

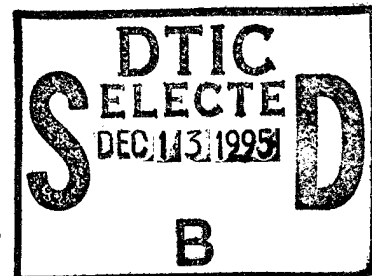
EXPERIMENTAL INVESTIGATION
OF NON-ADIABATIC SUPERSONIC
SLOT INJECTION INTO A
SUPERSONIC CROSS-FLOW

THESIS

Presented to the Faculty of the School of Engineering
of the Air Force Institute of Technology
Air University
In Partial Fulfillment of the
Requirements for the Degree of
Master of Science in Aeronautical Engineering

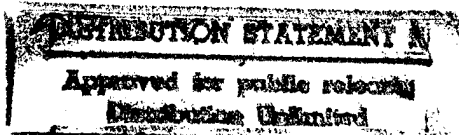
Kelly Colin Tucker
Second Lieutenant, USAF

December 19, 1995



19951211 066

DTIC AVAILABILITY INSPECTED 1



Jacobson, Carol

From: Kelly C Tucker
To: cjacobs0
Subject: RE: gaeeny23.ps.tar
Date: Thursday, December 07, 1995 1:00PM

The thesis titled "EXPERIMENTAL INVESTIGATION OF NON-ADIABATIC SUPERSONIC SLOT INJECTION INTO A SUPERSONIC CROSS-FLOW" is approved for public release; distribution unlimited. If would like I will send you a replacement Thesis title page with the appropriate statement. Thank you.

Lt Tucker

The views expressed in this thesis are those of the author and do not reflect the official policy or position of the Department of Defense or the United States Government.

Accession For	
NTIS GRA&I	<input checked="" type="checkbox"/>
DTIC TAB	<input type="checkbox"/>
Unannounced	<input type="checkbox"/>
Justification <i>Letter enclosed</i>	
By _____	
Distribution/	
Availability Codes	
Avail and/or Dist Special	
A-1	

EXPERIMENTAL INVESTIGATION
OF NON-ADIABATIC SUPERSONIC SLOT
INJECTION INTO A SUPERSONIC
CROSS-FLOW

THESIS
Kelly Colin Tucker
Second Lieutenant, USAF

AFIT/GAE/ENY/95D-23

Acknowledgments

I would first like to thank my advisor Dr. Rodney Bowersox for his enthusiasm and support for this research. His insight and guidance throughout the project were essential and greatly enhanced the quality of this work. I also appreciate Lt.Col. Jerry Bowman for his advise on the design of the air cooler, and thank Maj. Tom Buter for his feedback on the overall scope of the study.

I especially would like to thank Tim Handcock at the AFIT model shop. His craftsmanship, understanding, and patience were significant in the early stages of the component design. I would also like to thank our lab technician Andy Pitts. His expertise allowed us to keep working when the equipment would not.

I would like to express my appreciation to the AFIT Snack Bar for the donation of several hundred pounds of ice which was essential to the development and use of the air cooler in this experiment. These ladies have supported many students in many ways during my time here at AFIT.

Most importantly I would like to thank my lovely wife Allison for her patience, understanding and undying support through my time here at AFIT. I would not have made it without her. I also appreciate my parents encouragement and their stressing the importance of my education which helped prepare me for the challenges of AFIT and the Air Force.

Kelly Colin Tucker

Table of Contents

Acknowledgments.....	ii
List of Figures.....	vii
List of Tables	ix
List of Symbols	xi
Abstract	xiii
Chapter 1. Introduction.....	1
1.1 Objective	1
1.2 Motivation.....	1
1.3 Flowfield	2
1.4 Experimental Methods	3
1.5 Turbulence Models	4
1.6 Synopsis of the Research.....	4
Chapter 2. Turbulence Development and Modeling.....	6
2.1 Navier-Stokes Equations.....	6
2.2 Reynolds Averaged Navier-Stokes (RANS) Equations	7
2.3 Favre Averaged Navier-Stokes (FANS) Equations	9
Chapter 3. Facilities and Instrumentation	11
3.1 Experimental Facility	11
3.1.1 Supersonic Wind Tunnel	11
3.1.2 Supersonic Injector	12
3.1.3 Injection Heater	13
3.1.4 Injection Cooler	14

3.2 Mean Flow Instrumentation	14
3.2.1 Nicolet Data Acquisition System.....	14
3.2.2 Settling Chamber	15
3.2.3 Traverse and LVDT System with Coordinate System.....	15
3.2.4 Mean Flow Instruments.....	16
3.2.5 Data Acquisition Setup	17
3.3 Hot-Film Instrumentation.....	17
3.3.1 Anemometry	17
3.3.2 Cross-Film Probes.....	18
3.3.3 Cross-Film Angle Definition.....	18
3.3.4 Cross-Film Frequency Response.....	19
3.3.5 Data Acquisition Setup	19
3.4 Tunnel Operation and Data Acquisition.....	19
3.5 Optics and Flow Visualization.....	20
3.5.1 Photography and Alignment Techniques.....	20
3.5.2 Shadowgraph Photography	21
3.5.3 Schlieren Photography	21
3.6 Computational Facilities.....	22
Chapter 4. Data Reduction Techniques	23
4.1 Mean Flow Data	23
4.2 Hot-Film General Theory	24
4.2.1 Heat Transfer Theory	24
4.2.2 Cross-Film Turbulence	26

4.3 Cross-Film Analysis	28
4.4 Separation of Turbulence Variables.....	32
4.5 Raw Data Manipulation	33
Chapter 5. Results.....	36
5.1 Experimental Parameters.....	36
5.2 Optical Analysis and Results	37
5.3 Conventional Probe Mean Flow Data.....	40
5.4 Multiple Overheat Cross-Film Results	42
5.4.1 Mean Flow.....	42
5.4.2 Turbulent Flow	44
5.5 Flow Quality	47
Chapter 6. Conclusions and Recommendations.....	49
6.1 Conclusions	49
6.1.1 Optical Evaluation	49
6.1.2 Injectant Temperature Dependence	49
6.1.3 Injectant Temperature Independence.....	50
6.1.4 Turbulence Modeling Criteria.....	51
6.2 Recommendations.....	53
6.2.1 Current Injection Scheme.....	53
6.2.2 Computational Study	53
Appendix A. Error Analysis.....	93
Appendix B. Design of the Air Cooler	99
Appendix C. Reference Temperature and Pressure Data.....	102

Appendix D. MSHEAR Input Decks.....	105
Appendix E. Cold Injection Tabulated Data.....	109
Appendix F. Hot Injection Tabulated Data	117
Appendix G. Pitot and Cone-Static Data	131
Bibliography.....	136
Vita.....	139

List of Figures

<u>Figure</u>	<u>Page</u>
1.1 SCRAMjet Example	55
1.2 Sketch of Flowfield.....	56
3.1 Injection Model Schematic.....	57
3.2 two-dimensional Injector Nozzle.....	58
3.3 Traverse Stand	59
3.4 Tunnel Coordinate System.....	60
3.5 Mean Flow Probes.....	61
3.6 Hot-Film Probes	62
3.7 Hot-Film Probe Coordinate System	63
3.8 Hot-Film Channel - Angle Determination	64
3.9 Shadowgraph Optical Setup.....	65
3.10 Schlieren Optical Setup.....	66
5.1 Shadowgraph of Flowfield	67
5.2 Schlieren of Injector Region.....	68
5.3 Schlieren of Flowfield	69
5.4 Schlieren of Lambda Shock	70
5.5 Injector Mach Profile and Stream Function	71
5.6 two-dimensional Mach Profiles	72
5.7 Mach number and Reynolds number	73

5.8	Cross-film measured total temperature and average density	74
5.9	Mean flow velocity and mass flux flow angle	75
5.10	Mass Flux Data.....	76
5.11	Cross-film turbulence intensity data.....	77
5.12	Cross-film separated turbulence intensities	78
5.13	Cross-film transformed turbulent x-y shear data	79
5.14	Cross-film transformed turbulence x-z shear data	80
5.15	Cross-film mass flux - total temperature fluctuation correlations	81
5.16	Specific turbulent heat flux data	82
5.17	Cross-film velocity-velocity correlation data	83
5.18	Cross-film velocity-density correlations.....	84
5.19	Cross-wire TKE data.....	85
5.20	Cross-film separated Reynolds shear (xy).....	86
5.21	Cross-film separated Reynolds shear (xz) and Favre shear	87
5.22	Cross-film Favre variable data.....	88
5.23	Cross-film shear repeatability	89
5.24	Non-dimensionalized Reynolds number repeatability	90
5.25	Axial mass flux turbulence intensity repeatability	91
5.26	Total temperature repeatability	92
A.1	Recorded probe flex.....	98
G.1	Pitot and Cone-Static Data	132

List of Tables

<u>Table</u>	<u>Page</u>
5.1 Tunnel Conditions	36
5.2 Injector Conditions	37
5.3 Experimental Parameters	39
5.4 Local Freestream Conditions	40
A.1 Mean Flow Error	96
A.2 Hot-Film Error.....	97
E.1 UV#1 Cold Injection Component Data.....	110
E.2 UV#1 Cold Injection Mean Flow Data	111
E.3 UV#1 Cold Injection Separated Turbulence Data	112
E.4 UV#1 Cold Injection Reynolds Separated Data	113
E.5 UV#1 Cold Injection Compressible Shear Data	114
E.6 UV#1 Cold Injection Favre Data	115
E.7 UV#1 Cold Injection Turbulent Heat Flux Data.....	116
F.1 UV#1 Hot Injection Component Data.....	118
F.2 UV#1 Hot Injection Mean Flow Data	119
F.3 UV#1 Hot Injection Separated Turbulence Data.....	120
F.4 UV#1 Hot Injection Separated Reynolds Shear Data	121
F.5 UV#1 Hot Injection Compressible Shear Data	122
F.6 UV#1 Hot Injection Favre Data.....	123
F.7 UV#1 and UW Hot Injection Turbulent Heat Flux and TKE data.....	124

F.8 UW Hot Injection Component Data.....	125
F.9 UW Hot Injection Mean Flow Data	126
F.10 UW Hot Injection Separated Turbulence Data	127
F.11 UW Hot Injection Separated Reynolds Shear Data.....	128
F.12 UW Hot Injection Compressible Shear Data	129
F.13 UW Hot Injection Favre Data	130
G.1 Pitot and Cone-Static Tabulated Data	133

List of Symbols

a, b	Hot-film calibration constants
f, g	Hot-film sensitivities
i	Film current
k	Thermal conductivity
L	Length of film
M	Mach number
n	Calibration and power law exponent
Nu	Nusselt number
P	Pressure, pressure ratio
Pr	Prandtl number
q	Heat flux
q _w	Power through film
Re	Reynolds number
T	Temperature
U, V, W	x,y,z component velocities
x, y, z	Cartesian coordinates
α, β	Hot-film functions of Mach number
γ	Ratio of specific heats
δ	Boundary layer thickness
μ	Viscosity
ρ	Density

	ϕ	Hot-film incidence angle
	τ	Shear stress, film temperature loading
Subscripts	e	Effective
	cs	Cone-static
	d	Per film diameter
	m	Per meter
	n	Normal
	t2	Pitot
	t	Total, tangential
	T	Turbulent
	w	Wire or wall
	oo	Local
Superscripts	T	Turbulent
	()'	Reynolds fluctuation
	()"	Favre fluctuation
	$\overline{()}$	Mean or average

ABSTRACT

Turbulence and mean flow measurements were acquired downstream of a normal, supersonic ($M=1.6$), two-dimensional, slot injection into Mach 3.0 flow ($Re/m = 15 \times 10^6$). Two non-adiabatic cases ($T_{t_i}/T_{t_\infty} = 1.11$ and $T_{t_i}/T_{t_\infty} = 0.93$) were studied. Multiple overheat anemometry and conventional mean flow analysis, as well as shadowgraph and schlieren photography, were utilized to study the turbulent mixing layer. The mean flow data included the Pitot, cone-static, and Mach number profiles. The measured turbulence data included shear stresses, mass flux, total temperature turbulence intensities, and turbulent heat fluxes. The temperature and density variation in the flow provided a better understanding of the mixing process. The turbulence mass flux and shear results highlighted the importance of compressibility within the mixing region. The optical analysis showed the physical phenomena of the flow as well as the associated turbulent structure that existed in the mixing layer.

EXPERIMENTAL INVESTIGATION OF NON-ADIABATIC SUPERSONIC SLOT INJECTION INTO A SUPERSONIC CROSS-FLOW

Chapter 1

Introduction

1.1 Objective

The objective of this research was to experimentally investigate the mean and turbulent flow structure associated with a supersonic ($M=1.6$) slot injection of air, normally into a Mach 2.9 cross-flow. In particular, the effects of the injectant gas temperature on the flow was examined.

1.2 Motivation

Normal injection into a supersonic cross-flow is of fundamental and practical interest. This interaction may be identified in several areas, which include thrust vector control systems inside high temperature nozzles, reaction control jets of high speed flight vehicles, boundary layer and surface cooling of high temperature flows, and chemical laser mixing

enhancement. The primary interest for this study, however, centers around the area of fuel injection and the associated mixing enhancement in a supersonic combustor.

Mixing enhancement in a combustor type arrangement, particularly in a Supersonic Combustion Ramjet (SCRAMjet), consist of mixing a fuel and air as quickly and thoroughly as possible (see Fig. 1.1). The available time to mix the fuel with the incoming air, efficiently combust the mixture, and exit the products in a SCRAMjet will be on the order of milliseconds [1,2]. The thrust of the SCRAMjet will depend on several design considerations including the mixing enhancement and efficiency [3]. The fuel might also be used to actively cool the high temperature surface of the hypersonic vehicle being propelled by the SCRAMjet. All things considered, the fuel composition will no doubt be of a different density and temperature than the air with which it is designed to mix.

1.3 Flowfield

The flow regime created by a normal supersonic injection in a supersonic crossflow has associated with it, very violent and complex physics (see Fig. 1.2). The flow considered here is supersonic with a turbulent boundary layer upstream of the flush injector nozzle. Just slightly ahead of the injection stream, the boundary layer is disturbed and stopped causing a separation or bow shock to occur. Behind the bow shock, the injection plume continues expanding outside the nozzle and gives rise to a jet induced shock that the remainder of the flowfield must pass through. The injection plume then decelerates and encounters a normal shock to attain pressure equilibrium within the flow. The resultant

structure of the fluid flow resembles a disk, and is commonly recognized as a Mach disk for circular jets. For this two-dimensional interaction, the Mach disk spans the flow. Down stream of this Mach disk, the two fluid streams begin mixing. The main supersonic crossflow expands and accelerates as it flows over and interacts with the jet. The flow then encounters a recompression shock to turn the flow parallel to the wall. The mixing region is much larger than the upstream turbulent boundary layer, and continues to grow after encountering the recompression shock [4]. It is downstream of the recompression shock that this study concentrates.

1.4 Experimental Methods

Multiple overheat cross-film anemometry, mean flow instruments, as well as shadowgraph and schlieren photography were used to study the turbulent mixing layer downstream of the injector. The variety of experimental methods provides a thorough analysis of the turbulence and other flow specifics existing inside the mixing layer. The purpose of the injection was to combine as quickly and as thoroughly as possible the two fluids through the described injection scheme. Turbulence is a key factor in the mixing. The turbulent kinetic energy and shear forces existing in the mixing layer were measured, and provide insight into the important flow physics associated with the mixing. Total temperature and average density profiles in the mixing region characterize the effects that the injectant temperature has on the flow.

1.5 Turbulence Models

All flows of practical engineering interest are turbulent. However, accurate realistic computer solutions of the full Navier-Stokes equations using Computation Fluid Dynamics (CFD) are not and will not be available in the near future. Even with the rapid advancement in computing power and memory occurring almost daily, Spaziale noted that a numerical simulation of turbulent pipe flow with a Reynolds number of 500,000 would require a computer 10 million times faster than a Cray Y/MP [5]. Current solutions of complex, high-speed, high Reynolds number, compressible flows now rely on approximate averaging techniques applied to the Navier-Stokes equations. Due to the non-linear nature of the governing equations, this averaging results in additional fluctuation correlation unknowns, which require modeling. These models are currently the controlling factor in the accuracy of a realistic viscous turbulent flowfields. Also, understanding whether the turbulence models are valid and justified in a similar flowfield is of considerable interest. The experimental data presented in this research provides information to build a turbulence model or validate existing turbulence models for this complex mixing problem.

1.6 Synopsis of the Research

The first step in this research was an examination of the governing turbulent flow physics. Presented in Chapter 2 is a development of the governing equations. The second step was to scope the research project. An experimental investigation was performed using the

methods mentioned in Sec. (1.4). Then the flow field described in Sec.(1.3) with air as the injectant was chosen. This decision was based on two factors. One, this is a realistic flow that can be tested using the experimental facilities and instrumentation currently available at AFIT. Two, the available data in the literature concerning turbulence in these flows is scarce at best. The third step of this study was to perform the experiment and analyze the results. This is given in Chapter 5. Lastly, Chapter 6 summarizes the conclusions and recommendations.

Chapter 2

Turbulence Development and Modeling

The time-dependent, three-dimensional, compressible Navier-Stokes equations fully accommodate and explain the turbulent flowfield. For practical high Reynolds number problems, direct numerical simulation is not feasible on current or near future computers. Hence, scientist and engineers must rely on approximate averaged forms of the governing equations. This averaging procedure leads to statistical correlations that require models. This is known as the classical closure problem, and its solutions depends on empirical information to model the unknowns [6]. The two prevalent averaging techniques, Reynolds averaged (time) and Favre averaged (mass-weighted time), are presented in this chapter.

2.1 Navier-Stokes Equations

The averaging is based on the three-dimensional, time-dependent, Navier-Stokes equations for which the flowfield is defined. The governing conservation of mass, momentum, and energy equations, respectively are given by

$$\frac{\partial \rho}{\partial t} + \frac{\partial(\rho u_j)}{\partial x_j} = 0 \quad (2.1)$$

$$\frac{\partial(\rho u_j)}{\partial t} + \frac{\partial(\rho u_i u_j)}{\partial x_j} = -\frac{\partial p}{\partial x_i} + \frac{\partial(\tau_{ij})}{\partial x_j} \quad (2.2)$$

$$\frac{\partial(\rho h_o)}{\partial t} + \frac{\partial(\rho u_j h_o)}{\partial x_j} = \frac{\partial p}{\partial t} + \frac{\partial(u_i \tau_{ij} - q_j)}{\partial x_j} \quad (2.3)$$

where the total enthalpy, molecular shear stress and heat flux are defined as

$$h_o = h + \frac{1}{2} u_i u_i \quad (2.4)$$

$$\tau_{ij} = \mu \left(\frac{\partial u}{\partial x_j} + \frac{\partial u_j}{\partial x_i} \right) - \frac{2}{3} \mu \delta_{ij} \frac{\partial u_k}{\partial x_k} \quad (2.5)$$

$$q_j = -k \frac{\partial T}{\partial x_j} \quad (2.6)$$

2.2 Reynolds Averaged Navier-Stokes (RANS) Equations

This derivation can be found in detail in Refs. [7] and [8]. A brief overview and the results of these derivations are presented below.

The RANS are derived by replacing the random, three-dimensional, turbulent, unsteady flow variables in the general form with the mean plus the fluctuating component, such as

$$u(x, y, z, t) = \bar{u}(x, y, z) + u'(x, y, z, t) \quad (2.7)$$

The time averaged quantity is found by integrating the component with respect to time

$$\bar{u} \equiv \frac{1}{\Delta t} \int_{t_0}^{t_0 + \Delta t} u dt \quad (2.8)$$

where Δt is large, yet finite, compared to the period of random turbulent motion. The subsequent Reynolds Averaged Navier-Stokes Equations are given by (continuity, momentum, and energy)

$$\frac{\partial \bar{\rho}}{\partial t} + \frac{\partial}{\partial x_j} (\bar{\rho} \bar{u}_j + \bar{\rho}' \bar{u}'_j) = 0 \quad (2.9)$$

$$\frac{\partial}{\partial t} (\bar{\rho} \bar{u}_j + \bar{\rho}' \bar{u}'_j) + \frac{\partial}{\partial x_j} (\bar{\rho} \bar{u}_i \bar{u}_j) = - \frac{\partial \bar{p}}{\partial x_i} + \frac{\partial}{\partial x_j} (\tau_{ij} + \tau_{ij}^T) \quad (2.10)$$

$$\frac{\partial}{\partial t} (\bar{\rho} e_o + \bar{\rho}' h_o') + \frac{\partial}{\partial x_j} (\bar{\rho} h_o \bar{u}_j) = \frac{\partial}{\partial x_j} (\bar{u}_i \tau_{ij} + \bar{u}_i' \tau_{ij}' - q_j - q_j^T) \quad (2.11)$$

where the subscript o characterizes the stagnation (or total) condition and the subscript ij is all combinations of x, y, or z. The turbulent shear stress and heat flux are given by

$$\begin{aligned} \tau_{ij}^T &= -\bar{\rho} \bar{u}_i' \bar{u}_j' - \bar{u}_i \bar{\rho}' \bar{u}_j' - \bar{u}_j \bar{\rho}' \bar{u}_i' - \bar{\rho}' \bar{u}_i' \bar{u}_j' \\ q_i^T &= \bar{\rho} h_o' \bar{u}_i' + h_o \bar{\rho}' \bar{u}_i' + \bar{u}_i \bar{\rho}' h_o' + \bar{\rho}' h_o' \bar{u}_i' \end{aligned} \quad (2.12)$$

Bowersox [9] presents a turbulence transformation such that the turbulent shear and heat flux terms can be expressed as

$$\tau_{ij}^T = -\frac{(\bar{\rho} u_i)(\bar{\rho} u_j)}{\bar{\rho}} + \bar{\rho} u_i u_j \left(\frac{\bar{\rho}'}{\bar{\rho}} \right)^2 \quad (2.13)$$

$$q_i^T = \overline{(\bar{\rho} u_i)' h_o'} + \overline{h_o \bar{\rho}' u_i'} \quad (2.14)$$

The benefit of these formulations is that the leading terms in each equation can be directly measured with multiple overheat cross-film anemometry. The second terms can be estimated by separating the cross-film variables assuming the pressure fluctuation term (P') is zero.

2.3 Favre Averaged Navier-Stokes (FANS) Equations

The Favre averaged equations are based on mass-weighted time averages. The derivation can be found in detail in [7] and [10]. This average is represented as a mean plus a fluctuating component

$$u(x, y, z, t) = \tilde{u}(x, y, z) + u''(x, y, z, t) \quad (2.15)$$

where the Favre mean value is defined

$$\tilde{u} \equiv \frac{\bar{\rho}u}{\bar{\rho}} \quad (2.16)$$

These components differ from the Reynolds averages in the fact the average fluctuating components are not zero ($\bar{u}'' \neq 0$). The Favre-Averaged form of the Navier-Stokes equations are given by (continuity, momentum, and energy)

$$\frac{\partial \bar{\rho}}{\partial t} + \frac{\partial(\bar{\rho}\tilde{u}_j)}{\partial x_j} = 0 \quad (2.17)$$

$$\frac{\partial(\bar{\rho}\tilde{u}_i)}{\partial t} + \frac{\partial(\bar{\rho}\tilde{u}_i\tilde{u}_j)}{\partial x_i} = -\frac{\partial \tilde{p}}{\partial x_i} + \frac{\partial(\bar{\tau}_{ij} + \tau''_{ij})}{\partial x_j} \quad (2.18)$$

$$\frac{\partial(\bar{\rho}\tilde{e}_o)}{\partial t} + \frac{\partial(\bar{\rho}\tilde{h}_o\tilde{u}_j)}{\partial x_j} = \frac{\partial(\tilde{u}_i\bar{\tau}_{ij} + \overline{u''_i\tau_{ij}} - \bar{q}_j - q''_j)}{\partial x_j} \quad (2.19)$$

with the fluctuating shear and heat transfer terms defined as

$$\tau''_{ij} = -\overline{\rho u''_i u''_j} \quad (2.20)$$

$$q''_i = \overline{\rho h''_o u''_i} \quad (2.21)$$

and, neglecting viscosity fluctuations, the average shear term becomes

$$\bar{\tau}_{ij} = \mu \left[\left(\frac{\partial \tilde{u}_i}{\partial x_j} + \frac{\partial \tilde{u}_j}{\partial x_i} \right) - \frac{2}{3} \delta_{ij} \frac{\partial \tilde{u}_k}{\partial x_k} \right] + \mu \left[\left(\frac{\partial \bar{u}''_i}{\partial x_j} + \frac{\partial \bar{u}''_j}{\partial x_i} \right) - \frac{2}{3} \delta_{ij} \frac{\partial \bar{u}''_k}{\partial x_k} \right] \quad (2.22)$$

The Favre averaged turbulent shear stresses and heat fluxes can be estimated from multiple overheat cross-film anemometry with the assumption that $P' \approx 0$.

Chapter 3

Facilities and Instrumentation

3.1 Experimental Facility

This experimental investigation was performed at the Air Force Institute of Technology Mach 3.0 wind tunnel. This section describes the tunnel configuration, the supersonic injector, and the method of heating and cooling the injected air flow.

3.1.1 Supersonic Wind Tunnel

The tunnel is a pressure-vacuum facility. It is fitted with a Mach 3.0 half nozzle and contains two successive 33 cm long and 6.35 cm x 6.35 cm test sections (see Fig. 3.1).

This study was performed in the first test section. The plenum settling chamber contains a multi-screen flow straightener. The plenum total pressure and temperature were measured between the flow straightener and the convergent side of the nozzle. The pressure was monitored with a Endevco 0.69 MPa pressure transducer, and the temperature was measured with an Omega Engineering Type K thermocouple.

The high pressure system was powered by two Atlas Copco GAU 807 compressors and was dried via two methods. Initially, the air encountered two Pioneer Refrigerant Air Dryers when entering the high pressure reservoir. Then, before entering the tunnel plenum,

the air passed through a cyclone separator and multiple layers of high grade filters to insure no moisture nor foreign particles entered the test section. This system was capable of providing a mass flow of 0.75 kg/sec at a pressure of 0.20 MPa.

The vacuum system was separate from the high pressure system and provided a low pressure by two Stokes-Pennwalt evacuation vacuum pumps and one Stokes-Pennwalt seal exhaust pump. Each pump was powered by a Reliance XW Duty Master AC motor delivering 7.5 hp @ 1760 rpm and 460 volts. The low pressure system evacuated approximately 16 cubic meters of air to 267 Pa in 8 minutes, and was the limiting factor in the duration of the wind tunnel operation. The vacuum provided approximately 25 seconds of constant wind tunnel operation before unstarting occurred.

3.1.2 Supersonic Injector

The supersonic injector was designed to provide a two-dimensional mixing layer. The injector consisted of a settling chamber where the fluid pressure and temperature were measured prior to entering the converging diverging nozzle. The pressure was measured with a Endevco 0.35 MPa pressure transducer tapped into the plenum wall upstream of the nozzle, and the temperature was measured at the same location by placing an Omega Engineering Type K thermocouple in the plenum. The slot length was 4.45 cm long and was centered in the upper surface of the tunnel. The throat width was 0.159 cm with the exit width at 0.198 cm; this provided an area ratio of 1.25 which corresponded to a Mach 1.6 injection (see Fig. 3.2). The injector was machined from an aluminum plug that fit into

an existing opening in the tunnel upper surface. A three-dimensional contoured surface was included to provide a smooth transition from a circular feedline to the rectangular plenum. This shape insured a fully symmetric pressure distribution along the convergent surface of the injector. All items were machined at the AFIT machine shop.

The mass flow rates for the heated (1.76×10^{-2} kg/s) and cooled (1.81×10^{-2} kg/s) flows were within 2.5% of one another. This provided a baseline to compare the two conditions. The mass flow injected into the tunnel was controlled by an air feed line from the tunnel settling chamber where an adjustable valve was set to keep a constant injection pressure for a given tunnel plenum pressure (see Fig 3.1).

3.1.3 Injection Heater

The air was heated using a Reheat Co., Inc., 30.5 cm long tube coil type heater. The device heated the injected fluid to within +/- 2.0 degrees Celsius during each run. The air exited the heater directly into the injector plenum. It was necessary to keep air flowing through the heater while not taking data to prevent damage to the heater and keep constant the temperatures in the injector and tunnel upper surface. The auxiliary air feed line provided the necessary air which was then exited through a safety valve. An Omega Engineering Type J thermocouple was placed at the inside wall surface at the data taking location to measure the inside wall temperature. At the injector surface, the temperature was assumed to be the same as the injected fluid. A fixed point iterative procedure of manually adjusting the heater temperature relative to the mass flow was used to determine

what temperature the heater would consistently produce. It was determined that that the maximum attainable and repeatable temperature was 328 K, and was measured in the injector diffuser and recorded manually from an Omega Engineering Model 415B temperature display unit.

3.1.4 Injection Cooler

A heat exchanger was designed to cool the injected air to 273 degrees Celsius. A 0.189 cubic meter (50 gallon) garbage can was fitted with 15.2 meters of 1.27 cm outer diameter copper tubing coiled inside around a sturdy screen support. The garbage can was filled with an ice, salt, and water mixture which created an ice slush at -1.0°C at the surface of the container. This was chemically possible because the ice was produced at approximately 255 Kelvin, and the salt added to the mixture lowered the water's freezing point and therefore produced an ice slush at 272 Kelvin [11]. The length necessary to cool the air was calculated [12] (see Appendix B) and a factor of safety was added to produce an injection of air at 273 degrees Celsius. The upper wall surface temperature was measured by an Omega Engineering Type J thermocouple unit (see Fig. 3.1) and recorded manually from an Omega Engineering Model 415B temperature display unit.

3.2 Mean Flow Instrumentation

3.2.1 Nicolet Data Acquisition System

The Nicolet data acquisition system was Windows based and controlled four data acquisition boards with up to four channels on each board. The frequency rate that each

channel took data could be pre-selected, and the data acquisition trigger could be selected from either a board or a channel. All data was taken in voltage form and was reduced to appropriate values and units in the initial raw data reduction routines. This will be discussed in more detail in the following chapter. The system was run by a Zenith Z-Station 510, 486DX-33 with 8 megabytes of RAM and a 450 megabyte hard drive [13].

3.2.2 Settling Chamber

The supersonic wind tunnel was operated at its experiment design point by selecting the settling chamber pressure on a Fairchild pneumatic pressure regulator which controlled a Leslie brand dome regular valve. This is a mechanical system which consist of a feedback pressure line to equalize the settling chamber pressure. The total pressure was kept constant to 202 ± 3 kPa for both the hot and cold data sets. The pressure was recorded at 200 Hz for each run, and the temperature was recorded manually from an Omega Engineering temperature display unit.

3.2.3 Traverse and LVDT System with Coordinate System

The traverse was used to move the probes vertically in the flow. It was powered by an Arric Robotics MD-2 dual stepper motor driver and a Size 23 Stepper Motor. The motor turned a screw/slide assembly which moved the probe holder up and down. The position of the traverse was measured by a TransTek, Inc. Model 0217 linear voltage displacement transducer (LVDT). This device output voltage and was recorded by the Nicolet at 200Hz. This signal was used to trigger the Nicolet data acquisition system. Each time a

probe was inserted into the traverse and moved to its zero or initial location, the “zero” voltage was recorded and used in the data reduction. The traverse and LVDT assembly were bolted to an adjustable metal stand that had three degrees of freedom in alignment (see Fig. 3.3) The stand was built by the AFIT model shop.

The traverse was controlled by a Compaq Deskpro 386DX-25 running a program called TRAVERSE.BAS and communicated with the traverse via a RS-232 port on the PC. The program interface took user specified distances and speeds and moved the probe through the desired task.

The coordinate system used the center of the injector as the origin with the x-axis along the centerline of the tunnel positive in the direction of the flow, the y-axis positive up, and the z-axis positive to the right hand side of the tunnel (see Fig. 3.4).

3.2.4 Mean Flow Instruments

The mean flow measurements were made with a conventional Pitot probe and a 10° half-angle cone-static probe (see Fig. 3.5). The Pitot probe uses a 1.59 mm outer diameter stainless steel tubing inserted into a more rigid 3.18 mm stainless steel sleeve for support. The end of the Pitot probe was crimped to where the width was twice the length of the height to improve spatial resolution. The pressure was measured with a 103 kPa Endevco pressure transducer for each probe.

The cone-static probe has a 10° semi-vertex angle axisymmetric cone accurate to $\pm 0.03^\circ$.

Four 0.34 mm holes were placed at 90° increments at 4.3 mm from the tip. These pressure taps shared a common pressure chamber which averaged potential error from misalignment for up to $\pm 6^\circ$ to 7° [9,14]. The cone-static probe also used a 1.59 mm outer diameter stainless steel tubing inserted into a 3.18 mm stainless steel sleeve for support.

3.2.5 Data Acquisition Setup

The Nicolet data acquisition system recorded the pressures at 200Hz. Four channels of data were recorded during a mean flow data run. The tunnel plenum pressure voltage, the injector plenum pressure voltage, the location of the probe from the LVDT in volts, and the probe pressure in volts. The chamber and injector temperatures were monitored with an Omega Engineering Model 415B temperature display unit.

3.3 Hot-Film Instrumentation

3.3.1 Anemometry

The cross-film constant temperature anemometry was controlled by a TSI Inc. Intelligent Flow Analyzer (IFA) 100. The IFA 100 supported 2 hot-film channels, and each had a symmetrical bridge with a series resistance of 50Ω (R_s). An external 1:1 variable bridge arm was used to set the overheat resistance that defined the overheat ratio. The external resistance was set using a standard breadboard for each channel (film), and high quality, low inductance resistors were placed in series and parallel to build the necessary resistance. Six overheats ratios were used to define a data set. The overheat resistance

ratio (R_w/R_{ref}) ranged from 1.4 to 1.9. Low inductance TSI brand five meter cables were used for both the anemometer to film and anemometer to bridge connections [15]. Standard cables produced unacceptable noise in the signal.

3.3.2 Cross-Film Probes

TSI Inc. Model 1243-20 and Model 1243N-20 platinum hot-film probes were used in measuring the flow. The cross-film probes used two 1 mm long cylindrical cylinders with a 51 μm diameter. This accounted for a nominal 1 mm^2 total film cross-sectional area. The two probes measure flow in the x-y (1243-20) and x-z (1243N-20) planes (see Fig. 3.6). This allowed for all 3 velocity components to be measured and defined the complete flowfield. The UW (x-z plane) probe was only used in the heated cases and was used to help verify the accuracy of the UV (x-y plane) probes data. This was possible because both probes measure the U component information. Agreement between the probes was a factor in justifying the results since no other data was available.

3.3.3 Cross-Film Angle Definition

The angle of each of the two films on the cross-film probe must be determined relative to the flow direction to be used the data reduction discussed in Chapter 4. Figure (3.7) displays both the UV and UW component hot-film probes relative to the coordinate plane. The film angle is measured between the outward facing normal of the film and the x-axis as shown in Fig. (3.8). The channel - angle designation is the same for both probes and matches the component separation used in the data reduction.

3.3.4 Cross-Film Frequency Response

An important factor of taking multiple overheat cross-film data was the tuning and optimization of the cross-film frequency response. The cross-film was optimized by placing a square-wave AC signal across the film and viewing the film output signal on an oscilloscope. The anemometer gain and balance was optimized to a frequency response of nominally 150 kHz [15,16].

3.3.5 Data Acquisition Setup

The data acquisition setup was similar to that used in the mean flow except that five channels were taken during each run. These five channels include the tunnel plenum, injector plenum, LVDT, plus two channels for the cross-film. The cross-film data was taken at 20 kHz for a period of 13 seconds, with the other channels taken at 200Hz for the same length of time.

3.4 Tunnel Operation and Data Acquisition

The wind tunnel was started by manually switching the vacuum solenoid which opened the low pressure vacuum side, and then switching the high pressure solenoid which started the tunnel. The tunnel was shut down by closing the switches in reverse order.

Hot-film data was taken by using the above sequence and then manually starting the IFA 100 channels. This was accomplished by selecting the appropriate channel and pressing

run. The next step was to initiate the traverse movement sequence by running the traverse program. The Nicolet data acquisition system was triggered by the traverse LVDT. Data for each channel was saved to a file and reduced at a later time. The tunnel plenum, injector plenum, and wall temperatures were recorded manually at three times during the run. During calibration runs, the injector was turned off and the probe was left stationary in the center of the tunnel freestream. The tunnel mass flow was then adjusted by manually changing the plenum pressure setting . A complete range of Reynolds numbers, with the Mach number held constant, was used to calibrate the cross-film for the test flow conditions.

Between runs, the tunnel feedline was closed and an auxiliary high pressure line was used to match the mass flow rate necessary to keep the tunnel conditions constant for both the heated and cooled experiments. Both the settling chamber and auxiliary feed line could be opened and closed without changing the pressure ratio or feed line pressure. This insured repeatability in the testing conditions (see Fig. 3.1).

3.5 Optics and Flow Visualization

3.5.1 Photography and Alignment Techniques

The optical analysis consisted of shadowgraph and schlieren photography. Both photography techniques used a Polaroid open box type camera body with Type 57 Polaroid black and white film. The flash source was a Xenon Corporation Model N-787N arc lamp with a 10 ns duration with a 5ns rise time. It was powered by a Xenon

Corporation Model 437B nanopulser at 85% of its high voltage intensity. A single pulse was used for the photographic sequence. The optics for both setups were aligned using a Oriel Corporation Model 79255 HeNe gas laser operating at 0.95mW. After the sighting laser was removed and the arc light was repositioned, the optics were fine tuned by continuously pulsing the arc lamp which allowed the flash to be seen as nearly constant while aligning the knife edge on the schlieren.

3.5.2 Shadowgraph Photography

The shadowgraph photography setup consisted of the nanopulse arc lamp, one 165 cm focal length mirror, and the camera body. A collimated light beam that traversed the test section and entered the camera was created by placing the arc lamp at the focal point of the mirror (see Fig. (3.9) [17]). This type photography provides the second derivative (Laplacian) of the index of refraction existing inside the flow field normal to the optical path [18]. The shadowgraph photos were obtained through optical grade Plexiglas walls. Since the light beam was collimated, the photos were exactly to scale. These photographs were used to guide the selection of the test location inside the flowfield.

3.5.3 Schlieren Photography

The schlieren photography set up was more complex than the shadowgraph. The collimated light source was sent to a 165 cm focal length mirror and passed through the test section to a second 165 cm focal length mirror. A knife edge, which blocked approximately a third to a half of the light, was placed at the focal point of the second

mirror. Then, a flat mirror was used to reflect the light beam from the knife edge into the camera body (see Fig. (3.10) [17]). The schlieren provides the first derivative of the index of refraction through this process. When the knife edge and the arc lamp spark are both turned vertically, the photograph displays the density gradients in the vertical direction. More detail can be found in Bowersox and Hokenson [18]. The schlieren photographs were taken through both the Plexiglas and optical grade glass windows, and both types are presented in the results.

3.6 Computational Facilities

The majority of the computational work for the data reduction was done on a 486DX2-66 with 8 Megabytes of RAM, and a 850 Megabyte hard drive. Borland Spectra's TurboBasic was used to reduce the bulk data to a correlated output. The Fortran code MSHeAR [19] was used to do the reduce and separate the correlated data into the final results. Plots were generated using Grapher for Windows and contour plots were generated using Mathcad 5.0+. AFIT's Sun Sparc 20 work stations were used to store copies of data and facilitate uploading and downloading data files from the laboratory to the PC.

Chapter 4

Data Reduction Techniques

4.1 Mean Flow Data

Mean flow data was taken for two purposes. The first was to verify the 2D injection slot provided a good two dimensional flowfield which would facilitate only taking hot-film data at the centerline position. The second was to provide a Mach profile for the downstream mixing section. The Mach number was obtained from the solution of axisymmetric flow over a cone using Taylor-Mccoll conical flow theory and Rayleigh-Pitot formula. Bowersox [9] curve fit the solution as a function of the ratio of a cone-static probe (P_{cs}) and Pitot probe (P_{t2}) placed in the flow region of interest. Cone-static and Pitot pressure were taken over different runs; therefore, to account for any slight upstream total pressure differences the procedure below was used to build the proper relation.

$$P = \frac{P_{cs}}{P_{t1}} \frac{P_{t1}}{P_{t2}} \quad (4.1)$$

A least squares curve fit was used for the solution of axisymmetric supersonic flow over a cone and is presented below

$$M(P) = (-0.052976 + 4.6840P - 18.6786P^2 + 50.7006P^3 - 54.1577P^4)^{-1} \quad (4.2)$$

for $M \in [1.5, 4.4]$ and a standard deviation of $\sigma = 0.0006$.

4.2 Hot-Film General Theory

Hot-film anemometry provides experimental information in supersonic compressible flow by determining the rate at which the film or wire is cooled. The film is considered an infinite cylinder and acts as a resistor with a DC voltage placed across it. The film is one resistor (arm) in a wheatstone bridge arrangement, and the voltage across the film is increased or decreased to keep constant the desired temperature or overheat. Thus, the analysis is called constant temperature anemometry. The power required to keep the film at the desired temperature is equivalent to the heat loss of the wire to the flow. Hence, this voltage is measured and analyzed.

4.2.1 Heat Transfer Theory

The experimental investigative work was applied to a turbulent compressible flow. The dimensionless heat transfer or Nusselt number, applied to a cylinder (film) has the following functional form [16]

$$Nu = f(L/d, M, Pr, Re_e, \tau) \quad (4.3)$$

where L/d is the wire aspect ratio; M is the Mach number; Pr is the Prandtl number, Re_e is the effective Reynolds number based on the film diameter; and τ is the temperature loading factor. The loading factor is expressed as $\tau = (T_w - T_e)/T_t$, where T_w is the wire temperature, and T_e is the unheated equilibrium wire temperature. T_e is usually 97% of T_t when the film Reynolds number is greater than 20. Equation (4.3) is simplified when the Mach number normal to the wire is greater than 1.2, or $M \sin(\phi) \geq 1.0$, when Pr is

constant, and when the aspect ratio of the film is much greater than 1.0. For this case, the Nusselt number reduces to

$$Nu = f(Re_e, \tau) \quad (4.4)$$

This result has been experimentally verified. For a given wire temperature (τ), the following curve has been developed

$$Nu = (a Re_e^n + b) \quad (4.5)$$

where for the relatively high Reynolds number expected in this study ($Re_e > 100$), $n = 1/2$ has proven accurate.

The Nusselt number is also defined as a function of the power supplied to the film

$$\begin{aligned} Nu &= \frac{q_w}{\pi k_t L(T_w - T_e)} \\ q_w &= i_w^2 R_w \\ i_w &= \frac{V_w}{R_w + R_s + R_L} \end{aligned} \quad (4.6)$$

where q_w is power supplied; i_w is wire current; R_w is wire resistance; k_t is the thermal conductivity of the film; and V_w is wire voltage. The equilibrium temperature (T_e) is now assumed to be equal to the total temperature (T_t), and this is justified if used in both cross-film calibration and data reduction. Therefore, the Nusselt number can be presented as

$$Nu = \frac{V_w^2 R_w}{(R_w + R_s + R_L)^2} \frac{1}{\pi k_t L(T_w - T_t)} \quad (4.7)$$

To determine the appropriate heat transfer characteristics of the turbulent air, the physics of the supersonic flow upstream of the cross-film must be considered. A bow shock lies close to the film and the information about the flow lies upstream of the shock. However, the static temperature downstream of the shock is approximately equal to the total temperature ($T_2/T_t \approx 1$), and the bulk of the heat transfer occurs at the stagnation region of film. These two considerations allow both the thermal conductivity (using curve fits) and viscosity (Sutherland's formula) to be based on T_t in calculating Nu and Re [20].

4.2.2 Cross-Film Turbulence

To determine the mean and fluctuating hot-film equations, Eqns. (4.5) - (4.7) were combined and V_w , Re_e , and T_t were replaced with the mean plus the fluctuating components. The Binomial Theorem [21] is used, and with only the first order terms considered the *hot-film mean response* becomes

$$\frac{\overline{V_w^2}}{C_o} = \left(\frac{\overline{T_t}}{T_o} \right)^{n_k} \left[a\sqrt{Re_e} + b \right] (T_w - \overline{T_t}) \quad (4.8)$$

where C_o is defined as

$$C_o = \frac{(R_w + R_s + R_L)^2}{R_w} \pi L k_o \quad (4.9)$$

when $\frac{V'_w}{V_w}$ is solved for, the resulting *hot-film fluctuation equation* is

$$\frac{V'_w}{V_w} = f \left(\frac{Re o'_e}{Re o_e} \right) + g \left(\frac{T'_t}{T_t} \right) \quad (4.10)$$

where the *hot-film sensitivities* are

$$f = \frac{1}{4} \left(1 + \frac{b}{a\sqrt{\overline{Re}_e}} \right)^{-1} \quad \text{and} \quad g = \frac{-\overline{T}_t}{2(\overline{T}_w - \overline{T}_t)} + \frac{n_k}{2} - fn_\mu \quad (4.11)$$

and the thermal conductivity power law exponent, $n_k = 0.89$, and the viscosity power law exponent, $n_\mu = 0.77$, were found to match the data satisfactory. Re_e in Eqn. (4.10) is the effective Reynolds number evaluated at $\mu = \mu_o$. To determine f and g , the mean quantities $\sqrt{\overline{Re}_e}$ and \overline{T}_t must be evaluated. Since for this study multiple overheat ratios are used, a least squares analysis of the mean hot-film response yields the following equations

$$\begin{aligned} N\sqrt{\overline{Re}_e} + \overline{T}_t (\sum y_i - \sum x_i z_i) + 2\overline{T}_t \sqrt{\overline{Re}_e} \sum x_i + \overline{T}_t^2 \sum x_i y_i \\ + \overline{T}_t^2 \sqrt{\overline{Re}_e} \sum x_i^2 = \sum z_i \end{aligned} \quad (4.12)$$

$$\begin{aligned} \sqrt{\overline{Re}_e} (\sum y_i - \sum x_i z_i) + \overline{T}_t \sum y_i^2 + 2\sqrt{\overline{Re}_e} \overline{T}_t \sum x_i y_i + \sqrt{\overline{Re}_e} \sum x_i^2 \\ + \sqrt{\overline{Re}_e}^2 \overline{T}_t \sum x_i^2 = \sum y_i z_i \end{aligned} \quad (4.13)$$

where, $x_i = -1/T_{wi}$, $y_i = -b_i/(a_i T_{wi})$, $z_i = \overline{V}_{wi}^2 / (c_i a_i T_{wi}) - b_i / a_i$, where c is c_o with k_o replaced by k_t . N is defined as the number of overheat ratios, and the summations are over the i overheat ratios. The Secant Method [22] was used to iteratively solve the two non-linear equations above.

The *hot-film fluctuation equation*, Eqn. (4.10), was squared and averaged to obtain the turbulence results and is shown in this form

$$f_i^2 \left(\overline{\frac{Re o'_e}{Re o_e}} \right)^2 + 2f_i g_i \left(\overline{\frac{Re o'_e}{Re o_e} \frac{T'_t}{T_t}} \right) + g_i^2 \left(\overline{\frac{T'_t}{T_t}} \right)^2 = \left(\overline{\frac{V'_w}{V_w}} \right)_i^2 \quad (4.14)$$

A minimum of three overheat ratios are required to solve the three turbulence terms simultaneously. When more than three overheat ratios are used, a least squares analysis is applied. The *General Least Squares Method* (GLS-Method) is derived by Bowersox [9] and is applied to equation (4.14), yielding

$$\begin{bmatrix} \sum f_i^4 & 2\sum f_i^3 g_i & \sum f_i^2 g_i^2 \\ \sum f_i^3 g_i & 2\sum f_i^2 g_i^2 & \sum f_i g_i^3 \\ \sum f_i^2 g_i^2 & 2\sum f_i g_i^3 & \sum g_i^2 \end{bmatrix} \begin{bmatrix} \left(\overline{\frac{Re o'_e}{Re o_e}} \right)^2 \\ \left(\overline{\frac{Re o'_e}{Re o_e} \frac{T'_t}{T_t}} \right) \\ \left(\overline{\frac{T'_t}{T_t}} \right)^2 \end{bmatrix} = \begin{bmatrix} \sum f_i^2 \left(\overline{\frac{V'_w}{V_w}} \right)_i^2 \\ \sum f_i g_i \left(\overline{\frac{V'_w}{V_w}} \right)_i^2 \\ \sum g_i^2 \left(\overline{\frac{V'_w}{V_w}} \right)_i^2 \end{bmatrix} \quad (4.15)$$

where the summations are over the N overheat ratios. The least squares method shown above is *general* because the forms of f and g are not required. It is important to note, that the terms in both the sensitivity matrix and the right hand side vector have a combined power of four. Since the data is experimental and inherently contains scatter, the small errors are amplified by a factor of about 4. Hence, a careful calibration procedure was required to minimize the error amplification.

4.3 Cross-Film Analysis

The use of cross-film anemometry in supersonic flow must meet certain requirements to be a valid technique. The probes used in this research are canted at $\pm 45^\circ$ relative to oncoming

flow (see Fig. 3.7). It is necessary that $M\sin(\phi) \geq 1.0$ or that the Mach angle be larger than the wire angle. For this reason the Mach number was a determining factor in where the probe data would be considered valid in the flowfield of interest. The Mach number cutoff was calculated to be 1.41; however, a Mach number of 1.6 was chosen to account for viscous effects and probe flex during data taking.

In determining the transformation between the normal and tangential Reynolds number components to the x and y components is given by the matrix below

$$\begin{pmatrix} Re_n \\ Re_t \end{pmatrix} = \begin{bmatrix} \cos(\phi) & \sin(\phi) \\ -\sin(\phi) & \cos(\phi) \end{bmatrix} \begin{pmatrix} Re_x \\ Re_y \end{pmatrix} \quad (4.16)$$

The equations above are derived in tunnel coordinates, with the angle, ϕ , defined between the x-axis and the normal from the wire (see Sec. 3.3.3). The effective Reynolds number, Re_e , used in Eqn. (4.5) is defined as

$$\begin{aligned} Re_e^2 &= Re_n^2 \\ Re_e^2 &= A_1 Re_x^2 + 2A_2 Re_x Re_y + A_3 Re_y^2 \end{aligned} \quad (4.17)$$

where A_i are given by

$$\begin{aligned} A_1 &= \cos^2(\phi) \\ A_2 &= \cos(\phi) \sin(\phi) \\ A_3 &= \sin^2(\phi) \end{aligned} \quad (4.18)$$

The effective Reynolds number is replaced here with Re_{e_0} , which is the effective Reynolds number based on $\mu = \mu_0$ at the reference temperature T_0 for the power law viscosity

formulation [20]. $\overline{\text{Re}o_e}$, $\overline{\text{Re}o_x}$, and $\overline{\text{Re}o_y}$ are replaced by the mean plus the fluctuating component, and using the Binomial Theorem [21] and defining the following equations

$$\begin{aligned} R_o &= \frac{\overline{\text{Re}o_y}}{\overline{\text{Re}o_x}} \\ B_1 &= \frac{A_1}{B_3} \\ B_2 &= \frac{A_2}{B_3} \\ B_3 &= A_1 + 2A_2 R_o \end{aligned} \quad (4.19)$$

then assuming that $R_o^2 \ll 1.0$, it can be shown that

$$\begin{aligned} \overline{\text{Re}o'_{ej}} &= \overline{\text{Re}o_x} \sqrt{B_{3j}} \\ \left(\frac{\overline{\text{Re}o'_e}}{\overline{\text{Re}o_e}} \right)_j &= B_{1j} \left(\frac{\overline{\text{Re}o'_x}}{\overline{\text{Re}o_x}} \right) + B_{2j} \left(\frac{\overline{\text{Re}o'_y}}{\overline{\text{Re}o_y}} \right) \end{aligned} \quad (4.20)$$

where the j indexes one of the two wires on a cross-film probe. With the transformations performed above, the general film methods can now be applied to each of the wires on a cross-film probe.

Solving Eqn. (4.20) with the results from the two films, the mean results can be further resolved into x and y components of Re .

$$\begin{aligned} \overline{\text{Re}o_x}^2 &= \frac{\overline{\text{Re}o_{e1}}^2 / A_{21} - \overline{\text{Re}o_{e2}}^2 / A_{22}}{A_{11} / A_{21} - A_{12} / A_{22}} \\ \overline{\text{Re}o_y} &= \frac{1}{2\overline{\text{Re}o_x}} \frac{\overline{\text{Re}o_{e1}}^2 / A_{11} - \overline{\text{Re}o_{e2}}^2 / A_{12}}{A_{21} / A_{11} - A_{22} / A_{12}} \end{aligned} \quad (4.21)$$

The turbulence results can be decomposed into the x and y components by using the fluctuation equation in Eqn (4.20). Therefore,

$$\begin{aligned}\overline{\left(\frac{\text{Re } o'_x}{\text{Re } o_x}\right)^2} &= \frac{1}{D_2^2} \left[\frac{1}{B_{21}^2} \overline{\left(\frac{\text{Re } o'_e}{\text{Re } o_e}\right)^2} - \frac{2}{B_{21} B_{22}} \overline{\left(\frac{\text{Re } o'_e}{\text{Re } o_e}\right)_1 \left(\frac{\text{Re } o'_e}{\text{Re } o_e}\right)_2} + \frac{1}{B_{22}^2} \overline{\left(\frac{\text{Re } o'_e}{\text{Re } o_e}\right)_2^2} \right] \\ \overline{\left(\frac{\text{Re } o'_y}{\text{Re } o_x}\right)^2} &= \frac{1}{D_1^2} \left[\frac{1}{B_{11}^2} \overline{\left(\frac{\text{Re } o'_e}{\text{Re } o_e}\right)^2} - \frac{2}{B_{11} B_{12}} \overline{\left(\frac{\text{Re } o'_e}{\text{Re } o_e}\right)_1 \left(\frac{\text{Re } o'_e}{\text{Re } o_e}\right)_2} + \frac{1}{B_{12}^2} \overline{\left(\frac{\text{Re } o'_e}{\text{Re } o_e}\right)_2^2} \right] \\ \overline{\left(\frac{\text{Re } o'_x}{\text{Re } o_x} \frac{\text{Re } o'_y}{\text{Re } o_x}\right)} &= \frac{1}{2B_{11} B_{21}} \left[\overline{\left(\frac{\text{Re } o'_e}{\text{Re } o_e}\right)_1^2} - B_{11}^2 \overline{\left(\frac{\text{Re } o'_x}{\text{Re } o_x}\right)^2} - B_{21}^2 \overline{\left(\frac{\text{Re } o'_y}{\text{Re } o_x}\right)^2} \right]\end{aligned}\quad (4.22)$$

where D_i is defined in terms of B_{ij} of Eqn. (4.19)

$$\begin{aligned}D_1 &= \left(\frac{B_{21}}{B_{11}} - \frac{B_{22}}{B_{12}} \right) \\ D_2 &= \left(\frac{B_{11}}{B_{21}} - \frac{B_{12}}{B_{22}} \right)\end{aligned}\quad (4.23)$$

The General Least Squares Method [16] is used to solve the right hand side of Eqn. (4.22) except the middle correlation between wire 1 and wire 2. The covariance between the two wires on the cross-film probe is used to measure the correlation term. This covariance relationship is expressed as

$$\begin{aligned}\overline{\left(\frac{v'_w}{V_w}\right)_1 \left(\frac{v'_w}{V_w}\right)_2} &= f_1 f_2 \overline{\left(\frac{\text{Re } o'_e}{\text{Re } o_e}\right)_1 \left(\frac{\text{Re } o'_e}{\text{Re } o_e}\right)_2} + g_1 g_2 \overline{\left(\frac{T_t'}{T_t}\right)} \\ &\quad + f_1 g_2 \overline{\left(\frac{\text{Re } o'_e}{\text{Re } o_e} \frac{T_t'}{T_t}\right)_1} + f_2 g_1 \overline{\left(\frac{\text{Re } o'_e}{\text{Re } o_e} \frac{T_t'}{T_t}\right)_2}\end{aligned}\quad (4.24)$$

Equation (4.24) allows the x and y components of the Reynolds number to be computed.

The Reynolds number total temperature correlation is the remaining turbulence variable to be transformed into x and y components. It can be shown

$$\begin{aligned}\frac{\overline{\text{Re } o'_x T_t'}}{\overline{\text{Re } o_x T_t}} &= \frac{1}{D_2} \left[\frac{1}{B_{21}} \left(\overline{\frac{\text{Re } o'_x T_t'}{\overline{\text{Re } o_x T_t}}} \right)_1 - \frac{1}{B_{22}} \left(\overline{\frac{\text{Re } o'_e T_t'}{\overline{\text{Re } o_e T_t}}} \right)_2 \right] \\ \frac{\overline{\text{Re } o'_y T_t'}}{\overline{\text{Re } o_x T_t}} &= \frac{1}{D_1} \left[\frac{1}{B_{11}} \left(\overline{\frac{\text{Re } o'_e T_t'}{\overline{\text{Re } o_e T_t}}} \right)_1 - \frac{1}{B_{12}} \left(\overline{\frac{\text{Re } o'_e T_t'}{\overline{\text{Re } o_e T_t}}} \right)_2 \right]\end{aligned}\quad (4.25)$$

This analysis can be directly used to measure results in the x-z plane. The probe is rotated 90° about the x-axis, the v-component is replaced by w, the y is replaced by z, and the signs on the sine terms are changed in Eqn. (4.16).

4.4 Separation of Turbulence Variables

The procedure for the separation of the mass flux and total temperature terms into velocity and density fluctuation results is based on the assumption that for a thermally perfect gas ($P = \rho RT$), the density and temperature fluctuations are much larger than the pressure fluctuations. Considering only the first order terms and with the P' included for completeness, the following results can be obtained,

$$\begin{aligned}\frac{\bar{u}'}{\bar{u}} &= \frac{(\rho u)'}{\bar{\rho} \bar{u}} - \frac{\bar{\rho}'}{\bar{\rho}} \\ \frac{\bar{v}'}{\bar{u}} &= \frac{(\rho v)'}{\bar{\rho} \bar{u}} - R_o \frac{\bar{\rho}'}{\bar{\rho}} \\ \frac{\bar{\rho}'}{\bar{\rho}} &= \frac{1}{\alpha + \beta} \left[\beta \frac{(\rho u)'}{\bar{\rho} \bar{u}} - \frac{\bar{T}_t'}{\bar{T}_t} + \alpha \frac{\bar{p}'}{\bar{p}} \right]\end{aligned}\quad (4.26)$$

where α and β are defined as

$$\alpha = \frac{1}{1 + \frac{\gamma - 1}{2} M^2} \quad (4.27)$$

$$\beta = (\gamma - 1) \alpha M^2$$

Assuming $P' = 0$, the above equations provide the turbulent shear terms in the “Reynolds Averaged” Navier-Stokes equations.

The “Favre Averaged” Navier-Stokes equation’s terms were derived by defining the following relationships which are valid to third order

$$\begin{aligned} \frac{\bar{u}''}{U} &= \frac{-\bar{\rho}' u'}{\bar{\rho} u} \\ \frac{\bar{v}''}{U} &= \frac{-\bar{\rho}' v'}{\bar{\rho} u} \\ \bar{u}'' \bar{v}'' &= \bar{u}' \bar{v}' \\ U &= \frac{\bar{\rho} u}{\bar{\rho}} \end{aligned} \quad (4.28)$$

where $(\bar{})$ corresponds to the Favre or mass averaged fluctuating component

4.5 Raw Data Manipulation

All experimental data was acquired using the Nicolet Data Acquisition System (NDAS). The NDAS saved the individual channels of data in a compressed binary waveform file with a script heading describing the contents within. Nicolet also provided a waveform to ASCII conversion program which placed the stored data in two columns, the first being voltage and second time [13]. All five channels of hot-film data were taken

simultaneously with the probe in the mixing layer and moving down into the local freestream.

The hot-film data was taken at 20 kHz. Statistical averages (discussed below) were performed on blocks containing 4096 data points. This number was chosen from a binary standpoint because the data was converted from analog to digital through the NDAS while the data was being taken. At this rate of averaging, 49 points were spaced evenly in 2 cm span, though the first 7 were later removed because the Mach number was below the minimum 1.6 required for the response to be valid. This provided a spatial resolution of 1 data point every 0.04 cm inside the flow.

The data reduction program was written in TurboBasic. It read in 4096 points from both hot-film channel ASCII data files, then performed the following digital processing denoted

$$\bar{V} = \frac{1}{n_s} \sum_{i=1}^{n_s} V_i \quad (4.29)$$

$$\frac{\overline{(v')^2}}{\bar{V}^2} = \frac{1}{\bar{V}^2} \left[\frac{1}{n_s - 1} \sum_{i=1}^{n_s} (V_i - \bar{V})^2 \right] \quad (4.30)$$

$$\frac{\overline{(v'_1)(v'_2)}}{\bar{V}_1 \bar{V}_2} = \frac{1}{\bar{V}_1 \bar{V}_2} \left[\frac{1}{n_s - 1} \sum_{i=1}^{n_s} (V_i - \bar{V})_1 (V_i - \bar{V})_2 \right] \quad (4.31)$$

where n_s is the number of samples, and where 1 and 2 refer to the two wires on the cross-film [19]. Eqn. (4.29) is the average voltage, Eqn. (4.30) is the root mean squared voltage, and Eqn. (4.31) is the voltage cross-correlation. These equations were used to

process the raw blocks of data read by the reduction program. The reduction program repeated the averaging for all relevant data and stored the processed information into specific files to be used by MSHeAR. MSHeAR, which stands for **M**ultiple **O**verheat **S**upersonic **H**ot-Wire **A**nemometry **R**eduction **P**rogram [6], was written by Dr. Rodney Bowersox and was used to perform the analysis on the multiple overheat data described in sections (4.1) - (4.3) of this chapter.

Chapter 5

Results

This chapter presents and discusses the results obtained in the mixing region of a non-adiabatic, supersonic injection normally into a Mach 2.9 cross-flow. Full flowfield Mach number mapping was accomplished at two locations downstream of the injector to confirm the flowfield was nominally two-dimensional, and therefore justify taking all mean flow and hot-film data at the centerline position (see Sec. 5.3). The primary data location was chosen at 72 throat widths (x/w) downstream of the injector.

5.1 Experimental Parameters

The mean flow parameters of the experiment are summarized in Tables 5.1 and 5.2.

Table 5.1 Tunnel Conditions

Parameter	Cooled Case	Heated Case
Mach	2.9 ± 0.03	2.9 ± 0.03
$P_{t\infty}$	$203.9 \pm 2.8 \text{ kPa}$	$201.8 \pm 2.8 \text{ kPa}$
$T_{t\infty}$	$295.0 \pm 0.25 \text{ K}$	$293.0 \pm 0.25 \text{ K}$
$\rho_{t\infty}$	$2.41 \pm 0.03 \text{ kg/m}^3$	$2.40 \pm 0.03 \text{ kg/m}^3$
P_∞	$6.45 \pm 0.09 \text{ kPa}$	$6.39 \pm 0.09 \text{ kPa}$
T_∞	$110.0 \pm 0.08 \text{ K}$	$109.3 \pm 0.08 \text{ K}$
ρ_∞	$0.204 \pm 0.003 \text{ kg/m}^3$	$0.204 \pm 0.003 \text{ kg/m}^3$
V_∞	$610 \pm 5.0 \text{ m/s}$	$608 \pm 5.0 \text{ m/s}$
mass flow rate	$0.777 \pm 0.017 \text{ kg/s}$	$0.772 \pm 0.017 \text{ kg/s}$
Re/m	16.2×10^6	16.2×10^6

Table 5.2 Injector Conditions

<u>Parameter</u>	<u>Cooled Case</u>	<u>Heated Case</u>
Mach	1.6	1.6
$P_{t_{inj}}$	$61.0 \pm 0.7 \text{ kPa}$	$64.9 \pm 1.38 \text{ kPa}$
$T_{t_{inj}}$	$273 \pm 0.5 \text{ K}$	$329 \pm 2.0 \text{ K}$
ρt_{inj}	$0.78 \pm 0.01 \text{ kg/m}^3$	$0.69 \pm 0.019 \text{ kg/m}^3$
P_{inj}	$14.4 \pm 0.11 \text{ kPa}$	$15.3 \pm 0.29 \text{ kPa}$
T_{inj}	$181 \pm 0.25 \text{ K}$	$217 \pm 1.9 \text{ K}$
ρ_{inj}	$0.277 \pm 0.002 \text{ kg/s}$	$0.245 \pm 0.007 \text{ kg/s}$
Re /m	25.0×10^6	20.6×10^6
mass flow rate	$1.81 \pm 0.02 \times 10^{-2} \text{ kg/s}$	$1.76 \pm 0.05 \times 10^{-2} \text{ kg/s}$

5.2 Optical Analysis and Results

The primary use of photography in this research was to gain a better understanding of the overall flowfield and to define the flow conditions and measurement locations. The shadowgraph in Fig. (5.1) was used to guide the selection of injection pressure and to find the optimum location within the mixing region to make turbulence measurements. This decision was based on two criteria. First, the injector plenum pressure ($P_{t_{inj}}$) controlled the strength of the jet induced shock. A strong jet induced shock caused large reflected shock interactions within the mixing region. Second, the optimal data location needed to be as large as possible. This was important because data was only valid in 2/3 of the mixing region due to the Mach number limitations of the cross-film discussed in Sec. (4.3). The location chosen ($x/w = 72$) provided a 1.6 cm mixing region. This position is denoted in the flowfield sketch of Fig. (1.2).

The schlieren photography provided a crisp, highly detailed look at the flow physics. The area surrounding the injector region (Fig. 5.2), highlighted the viscous interaction as well as the complex and violent physics occurring at the intersection of two supersonic flowfields. The shock structure created when a supersonic stream of particles penetrated and stopped the tunnel turbulent boundary layer, shows a series of shocks forming a thick separation shock. Also, the injector plume continues to expand as it leaves the nozzle, and a shock forms on the upstream side of the plume. This jet induced shock intersects with the separation shock and forms a single shock which traverses the flowfield. Turbulent flow regions, detailed by random high and low density structures, are identified behind the separation shock and immediately downstream of the jet induced shock. The lighter region below the injection plume is the expansion experienced as the two flows turn, accelerate, and mix. The expanding flow then encounters a recompression shock which turns the flow parallel to the tunnel ceiling. Flow angles and shock positions are detailed in the sketch of Fig. (1.2).

Figure (5.3a) displays a schlieren of the entire flowfield made through the optical grade Plexiglas windows. A lambda shock is shown at the lower surface of the tunnel and is enlarged in Fig. (5.4). This viscous shock interaction occurs when the jet induced shock impinges the boundary layer on the lower surface and causes the boundary layer to separate. The separation bubbles creates a shock upstream of the impinging jet induced shock. The two shocks cross and form a lambda shaped formation. This shock is considered unsteady but no noticeable changes in position were seen from photo to photo.

However, some fluctuation was expected, and hence the area where the reflected lambda shock intersected the mixing region was avoided.

A schlieren of the injector and mixing regions was also taken through optical grade glass windows in the tunnel (Fig. 5.3b). The photo on the right displays a clear separation between the larger turbulent structure within the mixing region and the local freestream, both of which are downstream of the recompression shock. This separation was supported with the measured turbulence intensities discussed later in this chapter. However, to clarify for later discussion, the turbulent mixing region is defined as the first 1.6 cm from the upper surface, and the local freestream is defined between 1.6 and 2.5 cm from the upper surface of the tunnel. The chosen experimental parameters are presented below in Table (5.3).

Table 5.3 Experimental Parameters

Parameter	Cold	Hot
$P_{t_{inj}}/P_{t_{\infty}}$	0.30	0.32
$T_{t_{inj}}/T_{t_{\infty}}$	0.93	1.12
$U_{t_{inj}}/U_{\infty}$	0.72	0.79
P_{inj}/P_{∞}	1.36	1.20
T_{inj}/T_{∞}	1.64	1.99
$\rho u_{inj}/\rho u_{\infty}$	0.96	0.94

The local freestream conditions are summarized in Table (5.4) and are used to normalize data in the non-dimensionalized plots.

Table 5.4 Local Freestream Conditions

Mach	2.8
P _{t2}	70.8 kPa
P _{cs}	10.2 kPa
T _{t_{oo}}	290 K
ρ _{oo}	0.209 kg/m ³
V _{oo}	600 m/s
(ρu)bar	120 kg/m ² /s
ρbar ubar	125 kg/m ² /s
Re _d	341

The optical analysis is supported by the numerical simulation done previously by Rizzetta [4]. The Mach profile and stream function generated in that study is shown for comparison in Fig. (5.5). The Mach number contour plot shows the variation near the injector, and the stream function plot better displays the flow movement at the intersection of the two fluid streams. Rizzetta's work was performed with a Mach 3.7 crossflow and a $P_{t_{inj}}/P_{t_{oo}} = 0.31$, compared to a Mach 2.9 crossflow and $P_{t_{inj}}/P_{t_{oo}} = 0.30$ and 0.32 for this study. As is expected, the physical characteristics of the two flowfields are very similar.

5.3 Conventional Probe Mean Flow Data

A Mach number contour plot, shown in Fig. (5.6), was generated for the adiabatic injection case, over the entire y-z plane using cone-static and Pitot probes. This was performed at two locations downstream of the injector; the first location at 32 x/w and the second at 82 x/w. The resolution in the y direction provided one data point every 0.01

cm. The traverse data was taken at 7 stations (0, ± 0.95 cm, ± 1.59 cm, ± 2.22 cm) along the z axis to perform the mapping.

The Mach mapping shows good two-dimensionality in the mixing region, with some deviations close to the walls due to a wall boundary layer and other viscous interactions. In both the mixing region and the local freestream, the Mach lines are nominally constant along the z axis with some symmetric deviation. This slight variation may be due to the presence of weak axial vortices, described by Görtler. These vortices act as three-dimensional reattachment processes operating in the curved separated shear layer, and have been observed in prior slot gas injection configurations [23]. Nevertheless, the flow was still nominally two-dimensional in the y-z plane. It was assumed that the non-adiabatic cases would also be two-dimensional. The shock locations can be identified from the contour plots by the sudden reduction in the Mach number. This is attributed to the pressure discontinuity across a shock and the resultant effect on the mean flow probes. The position of the shocks, approximately 1.6 cm at 32 x/w and 1.8 cm at 82 x/w, shows good agreement with the schlieren photographs.

A Mach profile (Fig. 5.7a) was taken at the hot-film data location to provide mean flow data to separate the cross-film variables measured via the multiple overheat anemometry (see Sec. 4.4). The Mach profile was taken for both the cooled and heated test cases. The colder flow has a larger Mach number in the mixing region. This is a product of the speed of sound dependence on temperature, whereas the velocity shows little change between

the cases, the speed of sound decreases from a decrease in temperature and results in an increase of the Mach number. These changes will be discussed in the following section. Also, the profiles show good agreement outside the mixing region, where the non-adiabatic flow has not penetrated the local freestream. Please note that the heated Mach profile was taken at the exact location of the hot-film data, whereas the cooled Mach profile was taken 6.4 mm upstream of the hot-film location. Since the axial gradients in this region of the flow were expected to be small, this resulted in minimal discrepancy.

5.4 Multiple Overheat Cross-Film Results

5.4.1 Mean Flow

The cross-film analysis provided Reynolds number (Fig 5.7b) and total temperature results. The total temperature in conjunction with the Mach number data was used to compute the local mean flow properties. A plot of the total temperature profile (Fig. 5.8a) displays the change in total temperature within the flow. At 0.5 cm from the upper surface of the tunnel, the total temperature spans 7% or 20.3°C between the two cases. It is interesting to note that both the cooled and heated cases increase 2.0% in temperature at the boundary between the mixing region and local freestream (-1.3 to -1.6 cm). This result was expected since the large shear present at the freestream - mixing layer interface provided a means of slowing the flow and converting freestream kinetic energy to thermal energy as it entered the mixing layer.

The effect of the injected fluid temperature and density is most readily seen in Fig. (5.8b). The average density in the flow shifted 10% between the heated and cooled cases at the same location within the mixing region. The change stayed constant until the two cases intersected in the local freestream where the injected fluid had not penetrated. This plot shows that the injected fluid temperature strongly influences the resultant density within the mixing region. This is a valid assumption because the density shift is distinct and constant between the two cases for the same amount of mass having been injected into the flow. This is also an indication that the heated mixing region is larger (thicker) than the cooled because of the mass-volume relationship. The heated case is presented in Fig. (5.8b) with ρ_{bar} calculated by both the UV and UW component probes and is shown for agreement.

The mean flow velocity in Fig. (5.9a) shows that the average velocity in the U direction is the major component for both the heated and cooled cases. The injectant temperature has little influence on U except near the wall were the total temperature was the greatest. The mass flux flow angles in Fig (5.9b) also show very little change between the cooled and heated cases. The UW component probe measured a -2° flow angle in the local freestream. This was not anticipated, and could be considered either a misalignment error or that the measurement further supports the influence of three-dimensional vortices postulated earlier in Sec. (5.3).

In Fig. (5.10a) the hot-film measured mass flux ($\bar{\rho} u$) shows little distinction between the heated and cooled cases and agrees well with the calculated mass flux ($\bar{\rho} \bar{u}$) in Fig. (5.10b). The calculated mass flux is determined from the hot-film measured total temperature and the mean flow measured Mach number. The plot of ($\bar{\rho} \bar{u}$) does show a consistent shift of 7 - 10% throughout the mixing region due to the temperature difference between the two cases until converging at the local freestream. The individual mass flux variables in both plots were normalized with the local freestream quantities summarized in Table (5.3). The overall agreement between the two methods of determining the mass flux is very good.

5.4.2 Turbulent Flow

The mass flux and total temperature turbulence intensities for both the heated and cooled injections are given in Fig. (5.11). The heated and cooled results agree very well. The traverse and spanwise mass flux turbulence are approximately 50% of the axial values. The total temperature fluctuations levels are independent of the injectant fluid temperature. This indicates that the production of thermal energy from the freestream kinetic energy, described in the total temperature discussion, is considered the most significant contribution. Also, the peak in the density flux profile near the edge of the shear layer reinforces the thermal energy production at the edge of the two regions. The separated results presented in Fig. (5.12) demonstrate that the axial, traverse, and spanwise velocity fluctuations all have the same order of magnitude and trends. This

information, coupled with the mass flux turbulence intensity variation of 50% between the axial and other components (Fig. 5.11), emphasizes the compressibility of the region.

The compressible shear terms are presented in Figs. (5.13) - (5.14) and represent the measured values for Eqn. (2.13) which have been normalized by the corresponding $(\bar{\rho}u^2)$. As can be seen, the second term in Eqn. (2.13) is much smaller than the first. Hence for this flow, the cross-film shear provides a direct measurement of the turbulent shear stress. The shear stresses display strong influence from the injection temperature. At -0.8 cm into the flow, the cooled shear value is exactly half of the heated shear. Figure (5.14b) presents the individual cross-film shear terms plotted together to better quantify the magnitude and trends between the heated and cooled injection and between the UV and UW component shear.

The cold injection axial mass-flux total temperature fluctuation correlations (Fig. 5.15) is 20% smaller than the hot injection terms. For both cases the axial flux is the largest. The traverse, which is the important component for thin layer type flows, showed no dependence on the flow temperature. The specific turbulent heat flux is shown in Fig. (5.16). The axial and traverse heat flux was dependent on the injectant temperature with the heated case approximately 25% larger than the cooled.

The velocity-velocity correlations (Fig. 5.17) are similar in the x-y and x-z planes and correspond well between the heated and cooled cases. The velocity-density correlations in

Fig. (5.18) are of the same order of magnitude between the heated and cooled conditions, but have different trends as the data traverses the mixing region. The axial component is the largest, with the traverse and spanwise components at roughly 60% of the axial magnitude.

Figure (5.19) displays the compressible and incompressible turbulent kinetic energy (TKE) results for the heated case only. In the mixing region, the incompressible TKE is 60% of the compressible. This again emphasizes the importance of the compressibility in this supersonic flowfield.

The separated Reynolds shear terms (xy) in Fig. (5.20) and defined in Eqn. (2.12) are influenced by the injected fluid temperature and density. The incompressible term, denoted by a square, is reduced 33% from its peak value while within the mixing region of the cooled case and affected the shape of the resultant Reynolds shear. The heated case incompressible term, however, follows the same trend and has the same magnitude as the compressible shear term. In both cases, the compressible term, denoted by a circle, does not exhibit any dependence on the injectant temperature. The third term of Eqn. (2.12) was negligible for each of the plots. The separated Reynolds shear terms (xz) in Fig. (5.21a) display a large difference between the two influential separated terms. The compressible shear term is twice the size of the incompressible term, and compared to the xy component shear terms, the compressible term is roughly 20% larger in the xz plane.

Although the separated magnitudes vary between the xy and xz results, the total Reynolds shear in the xy and xz planes, has the same trend and magnitude.

The Favre mass averaged data shown in Figs. (5.21b) and (5.22) provide the shear and velocity fluctuations terms. The shear terms are plotted together to display the good agreement between the heated and cooled injection. The velocity fluctuations show that the axial velocity turbulence is twice that of the traverse and spanwise components and share the same temperature independence.

5.5 Flow Quality

The repeatability of the experimental data produced in this study was used gauge the quality of the obtained information. For the cooled injected case, two separate data sets were used. The heated injected case is supported by two UV component data sets and a single UW component data set. The UV and UW component probes both measure the axial component information and are used to validate one another. The cross-film shear, Reynolds number, axial mass-flux turbulence intensities, and total temperature profiles are provided and discussed. The data presented in Figs. (5.7) - (5.22) correspond to the UV#1 data in the repeatability plots and the single UW probe data. The UV#2 data is the validation set to check the flow quality for the UV component information and is plotted in Figs. (5.23) - (5.26) with the previously displayed data.

The cross-film shear repeatability is presented in Fig. (5.23). The agreement in each plot is excellent. This agreement is important because the shear is a second order variable and shows the stability of the measured quantities in both the heated and cooled cases.

The Reynolds number is plotted with two UV component probes for the cooled case and two UV and one UW component probes for the heated case in Fig. (5.24). The plots show excellent agreement and validate the hot-film calibration between the individual sets of data . The flow characteristics are repeated with excellent agreement.

The turbulence characteristics of the two injection flows are also repeatable as shown in Fig. (5.25). Again, excellent agreement between the individual sets of data is seen. The heated case axial mass-flux turbulence intensity is measured by both the UV and UW component probes and match throughout the flowfield.

The measured total temperature is presented in Fig. (5.26). The cooled case again shows an increase in the flow temperature in the boundary between the mixing region and local freestream with both data sets. The heated case shows excellent agreement with both UV component probes. The UW component also agrees but varies slightly from the UV component measurements in the unstable interface between the two regions of flow.

Chapter 6

Conclusions and Recommendations

The mean flow and turbulent physics associated with the Mach 1.6 non-adiabatic normal injection into a Mach 2.9 crossflow was experimentally investigated. Conclusions from the results are discussed and recommendations for future studies are presented.

6.1 Conclusions

6.1.1 Optical Evaluation

The optical analysis provided an excellent method to better understand the flowfield generated by the intersection of two supersonic fluids and the resultant mixing phenomena. The visual study provided for a better understanding of the complex viscous interactions which comprise the flowfield in this study. Rizzetta's numerical study [4] provided a reference to further support and describe the injection physics displayed in the photographs.

6.1.2 Injectant Temperature Dependence

The mean flow properties of the flowfield were most readily affected by the injectant temperature. This information is conveyed in both the conventional and hot-film probe data. The Mach number (Fig. 5.7a) was affected by the speed of sound dependence on

temperature. The total temperature spanned a full 23°C at its largest point between the two cases, and the density averaged a 10% shift throughout the mixing region (Fig. 5.8). The injectant fluid, however, did not penetrate nor affect the local freestream. This is supported by the agreement in the local freestream for all the data.

Certain turbulence variables were also affected by the injectant temperature. The turbulent shear stresses, which are measured directly, were strongly affected by the injected fluid temperature (Fig. 5.14b). The cold injection shear, at -0.8 cm within the turbulent mixing region, was found to be 50% smaller than the hot injection case. The cross-film axial mass flux - total temperature fluctuation correlations show a 20% rise in magnitude from the cooled to the heated case with no affect on the traverse component. Also, both the axial and traverse components of the specific turbulent heat flux increased 25% from the cooled to the heated cases.

6.1.3 Injectant Temperature Independence

The injectant temperature did not affect the total temperature production within the mixing region. The total temperature plot in Fig. (5.8) displays a 2% increase in temperature in the interface region (-1.2 to -1.6 cm) before experiencing the influence of the injectant temperature and diverging. This indicates that the turbulent dissipation of both the freestream and injection kinetic energy resulted in the generation of relatively high amounts of thermal energy. This effect practically mask any influence of the injection temperature. This energy translation is also supported by the density fluctuations in Fig.

(5.12), where both the heated and cooled density fluctuations peak at the intersection of the two regions. These density peaks essentially represent the static temperature fluctuation maximum within the flow.

The mass flux turbulence intensity was essentially unaffected by the temperature of the injected fluid (Fig. 5.11). In both the axial and traverse components, as well as the total temperature fluctuations, the magnitudes and trends did not change from case to case.

6.1.4 *Turbulence Modeling Criteria*

Settles and Dodson presented a set of criteria to justify using experimental data to build a turbulence model for a shock / boundary - layer interaction [24]. The criteria and how it was extended to this study is presented and explained below.

- 1.) *Baseline applicability*: This experimental study investigates a normal Mach 1.6 injection into a Mach 2.9 freestream.
- 2.) *Simplicity*: This is a previously studied [4], simple two-dimensional injection scheme, with practical applications in several areas which are discussed in Sec. (1.2).
- 3.) *Specific applicability*: Turbulence information for this valid mixing scheme is critical in fully understanding the physics of the flowfield and possible applications to more complex mixing problems.
- 4.) *Well - defined experimental boundary conditions*: The incoming flow conditions upstream of the injector are presented in Miller [25] and Dotter [26] for this same facility

and conditions. Also, the two-dimensionality of the flowfield was validated by the Mach number mapping along the y-z axis shown in Fig. (5.6). This was done at two locations downstream of the injector, before and after the primary data location.

5.) *Well - defined experimental error bounds:* The repeatability of the data is proven in Sec. (5.5), with an error analysis given Appendix A.

6.) *Consistency criterion:* No mutually inconsistent results were discovered.

7.) *Adequate documentation of data:* The data is presented in both the figures and tabulated form in the Appendix.

8.) *Adequate spatial resolution of data:* The turbulence data was provided with 0.4 mm spatial resolution, and the meanflow was provided at a 0.2 mm spatial resolution in studying the flowfield.

9.) *Turbulence data:* A full range of turbulence data was presented including Reynolds shear stresses, velocity and mass-flux fluctuations, and compressible turbulent kinetic energy data.

10.) *Realistic test conditions:* The test conditions included non-adiabatic injection, non-adiabatic wall temperatures, and was evaluated in a viable SCRAMjet supersonic flowfield.

11.) *Redundant measurements:* The UV and UW hot-film probes provided excellent agreement in measuring the axial data components within the flowfield. Also the mass flux measurements by both the hot-film and conventional probes coincide.

This study meets and exceeds all of the critical criteria necessary to justify its use in building a turbulence model.

6.2 Recommendations

6.2.1 *Current Injection Scheme*

Multiple overheat cross-film anemometry used in conjunction with conventional mean flow devices, as well as shadowgraph and schlieren photograph prove to be a formidable experimental investigative technique. This analysis has described the flowfield with great detail and repeatable accuracy. Other investigative techniques could be applied such as Laser Doppler Velocimetry (LDV) and triple-film anemometry which would validate and expand upon the results found in this study. However, a parametric study incorporating the use of a sonic nozzle versus the supersonic nozzle used in this study, would be more easily compared to similar research existing in the literature [4]. Also, changing the injected fluid to helium, which has a lower molecular weight, could better estimate the changes of density within the flowfield and more accurately simulate a hydrogen injection in a SCRAMjet fuel mixing simulation. Lastly, the injection scheme could be applied to a larger Mach number cross-flow to resemble a higher Mach number flight condition associated with a SCRAMjet propulsion system.

6.2.2 *Computational Study*

A computation model of this injection scheme should be performed. The information obtained in this current study should be used to validate a numerical turbulence model.

The information from the computation study could be used to devise better injection schemes, perhaps based on similar physical flowfields which then could be estimated with a subsequent model. A purpose of this current study was to support the less expensive computational work with accurate turbulence information in numerically convenient form for which a CFD analysis could be improved.

Sketch of a Hypersonic Vehicle with a SCRAMjet Engine

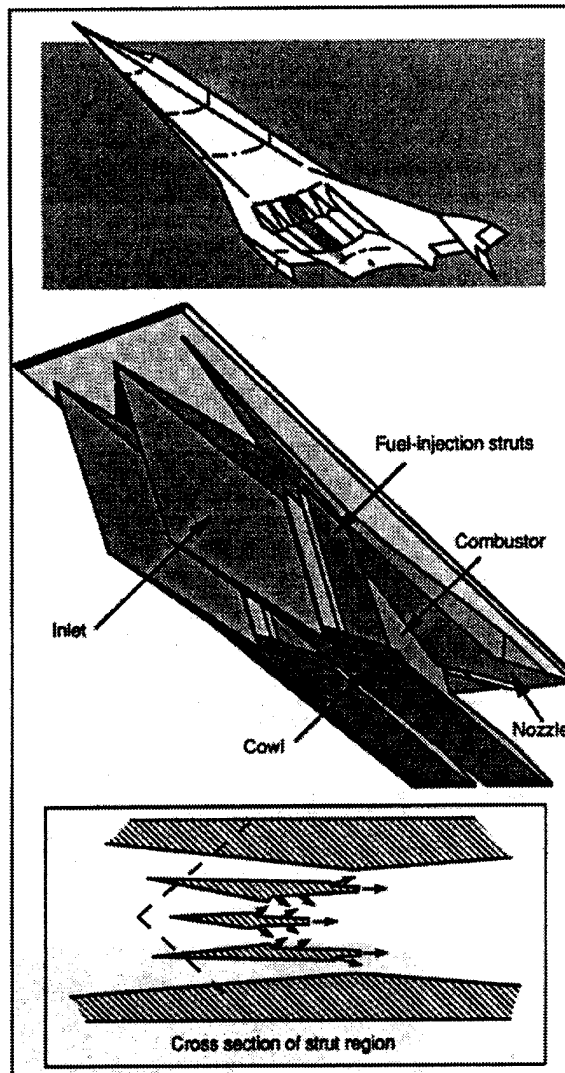


Fig. 1 Airframe-Integrated Supersonic Combustion Ramjet
(NASA).

Figure 1.1: SCRAMjet Example.

Flowfield Sketch (To Scale)

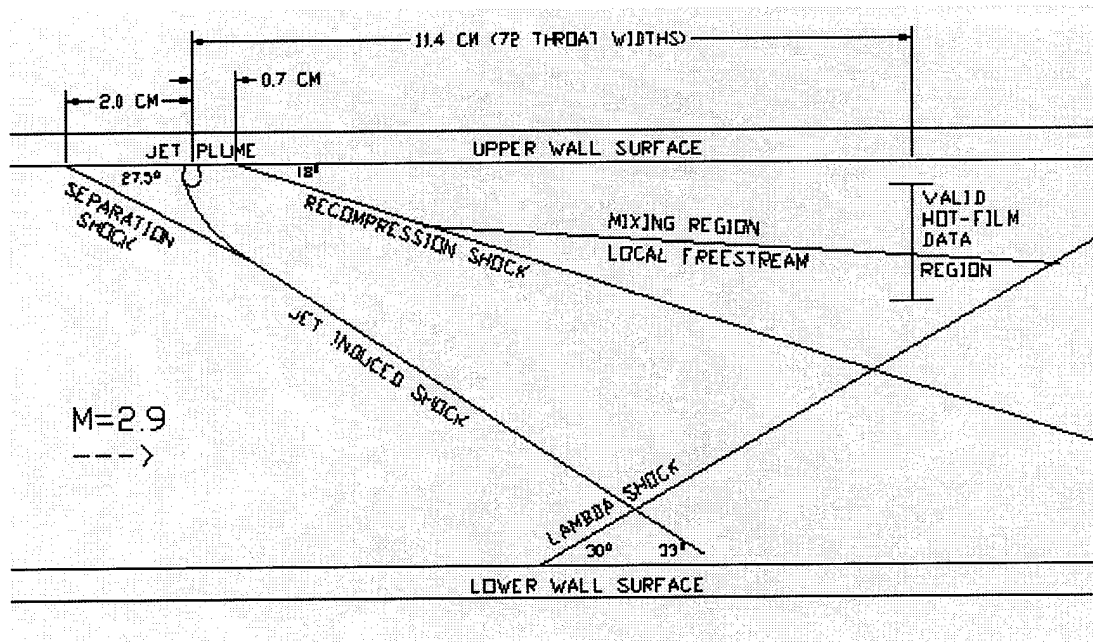


Figure 1.2: Flowfield Sketch with Hot-Film Data Location.

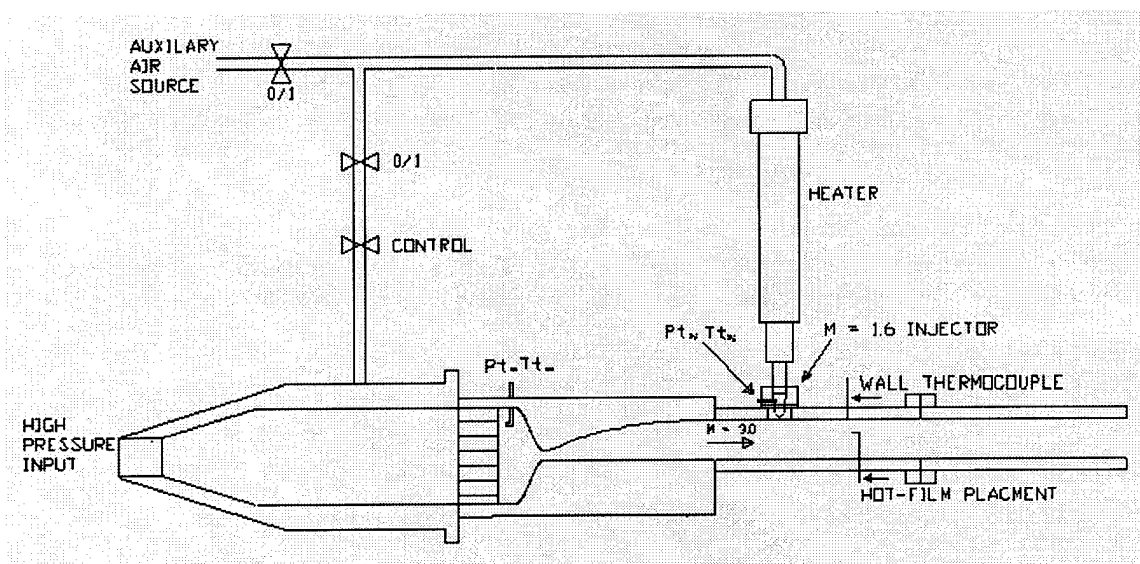


Figure 3.1: Injection Model Schematic.

$M=1.6$ $A_E/A^*=1.25$

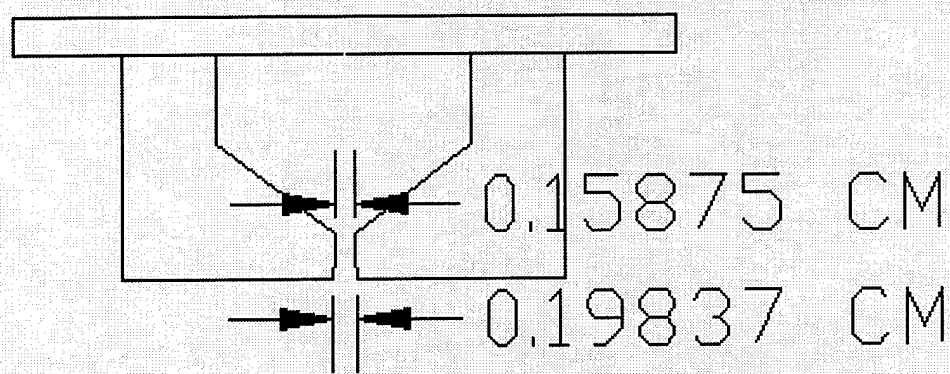


Figure 3.2: Two-Dimensional Injector Nozzle.

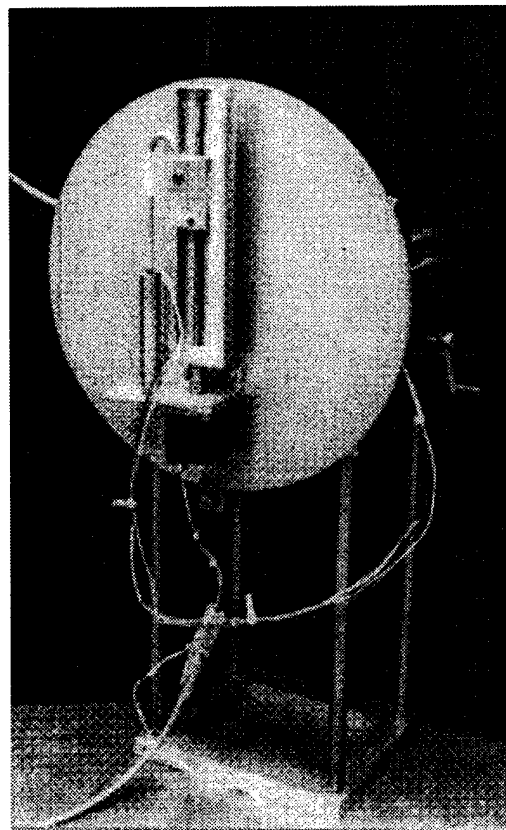


Figure 3.3: Traverse Stand.

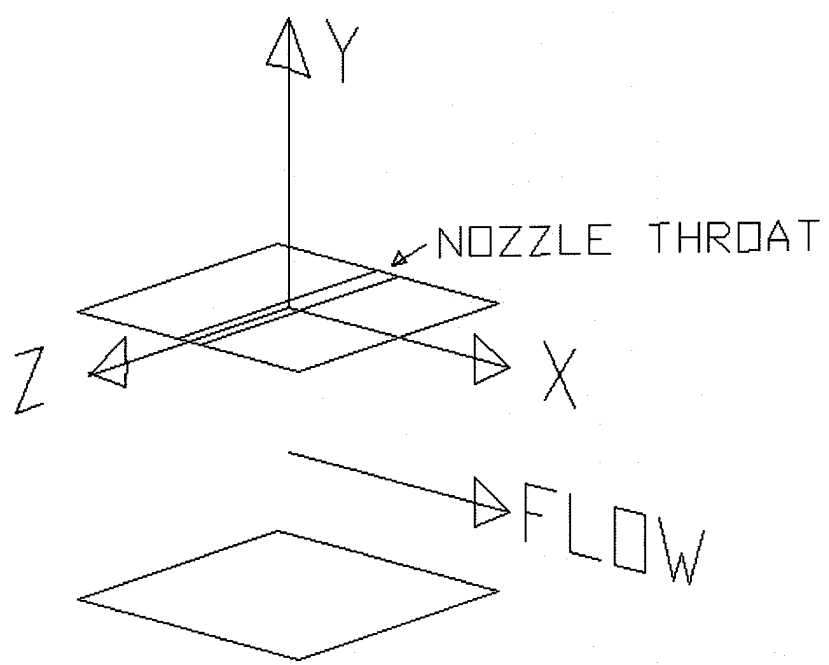


Figure 3.4: Tunnel Coordinate System.

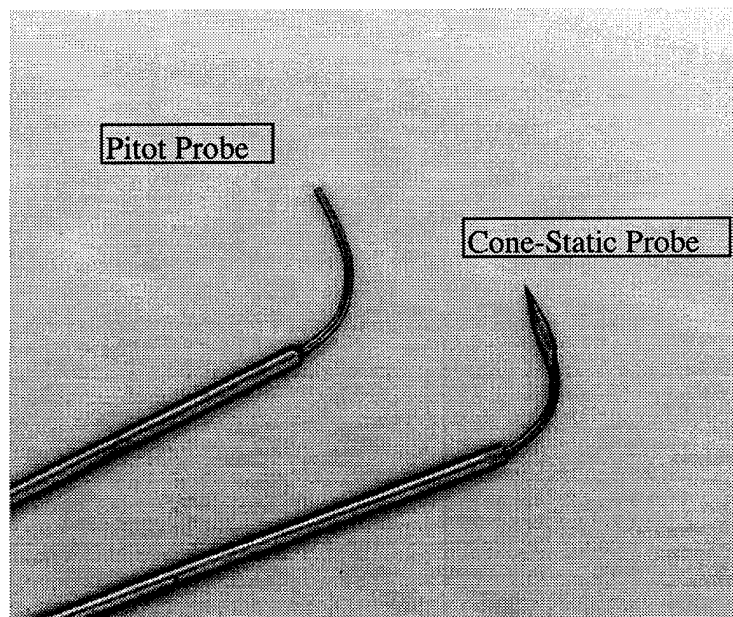
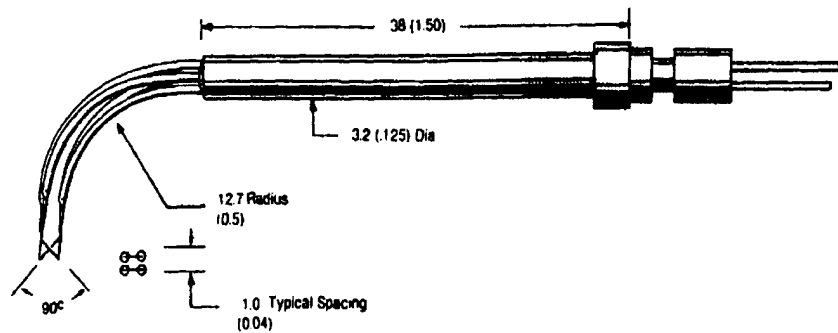
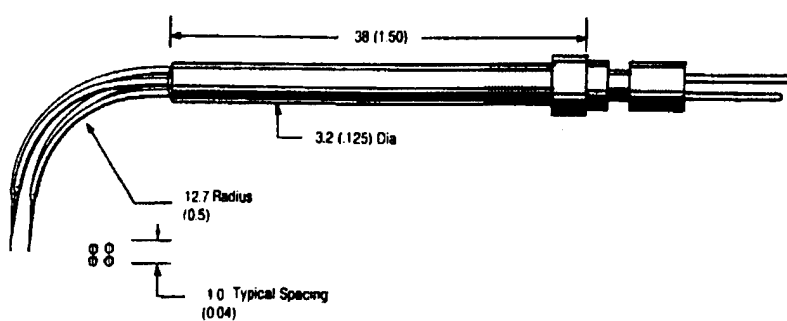


Figure 3.5: Mean Flow Probes.



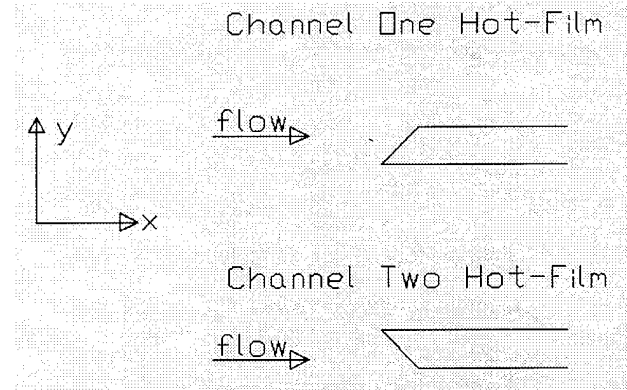
UV Probe (X-Y Plane)



UW Probe (X-Z Plane)

Figure 3.6: Hot-Film Probes.

UV Component Hot-Film Probe



UW Component Hot-Film Probe

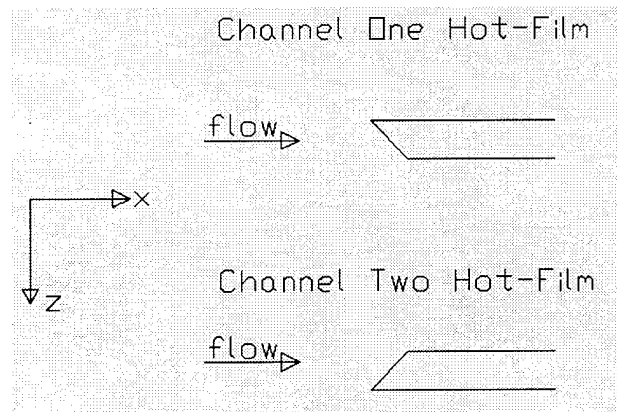
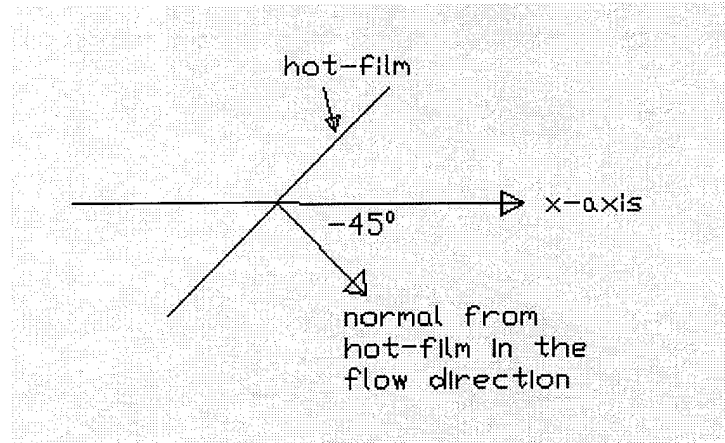


Figure 3.7: Hot-Film Probe Coordinate System.

Hot-Film Channel One Angle Determination



Hot-Film Channel Two Angle Determination

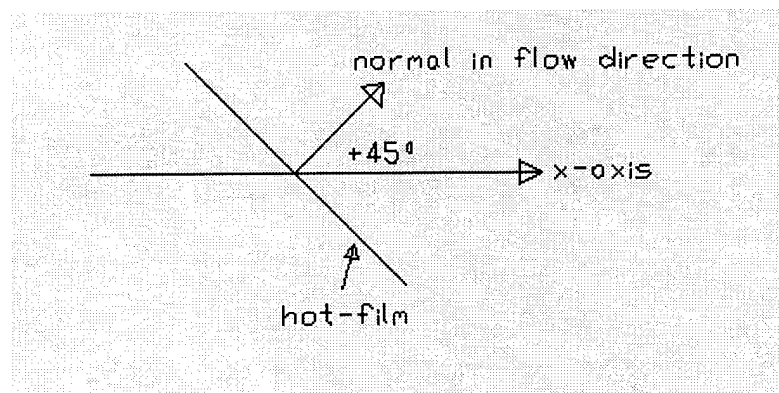


Figure 3.8: Hot-Film Channel - Angle Determination.

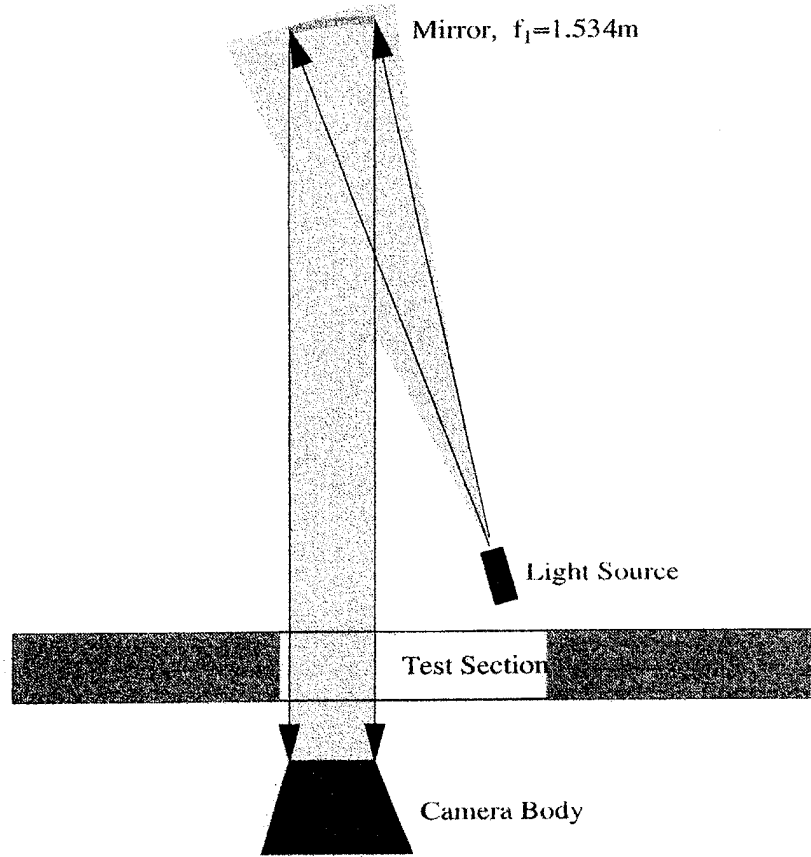


Figure 3.9: Shadowgraph Optical Setup [18].

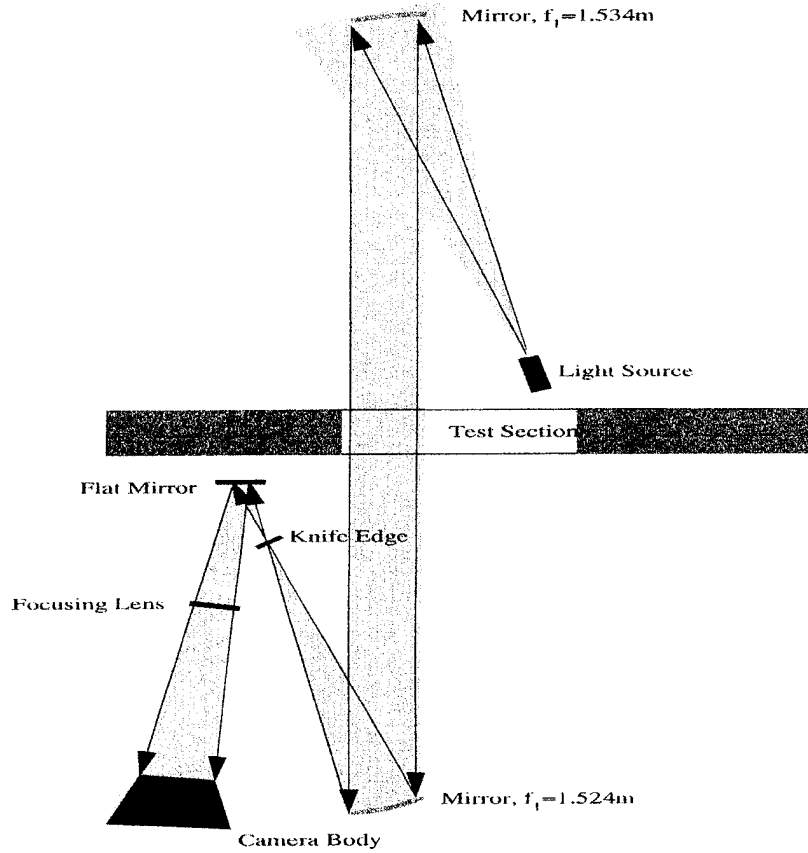


Figure 3.10: Schlieren Optical Setup [18].

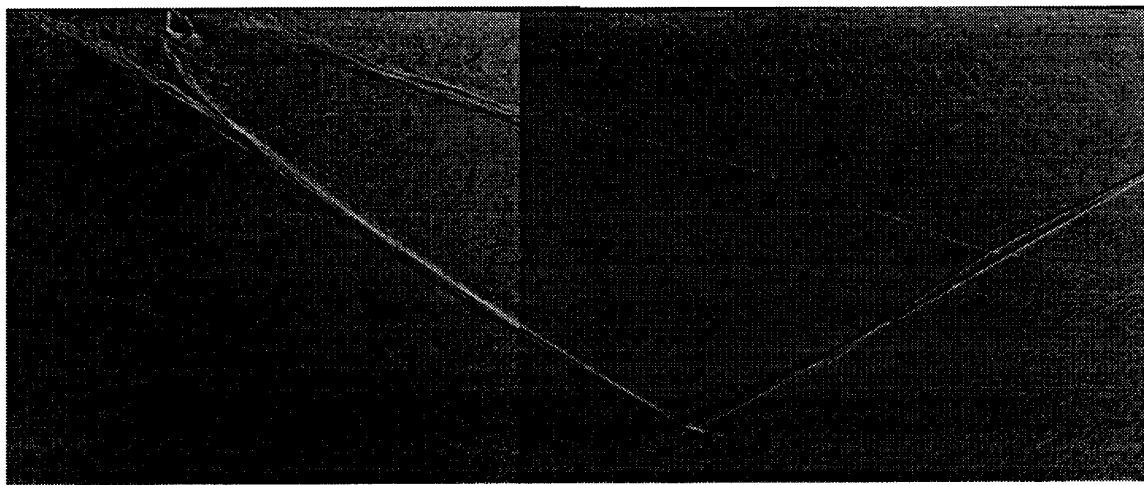
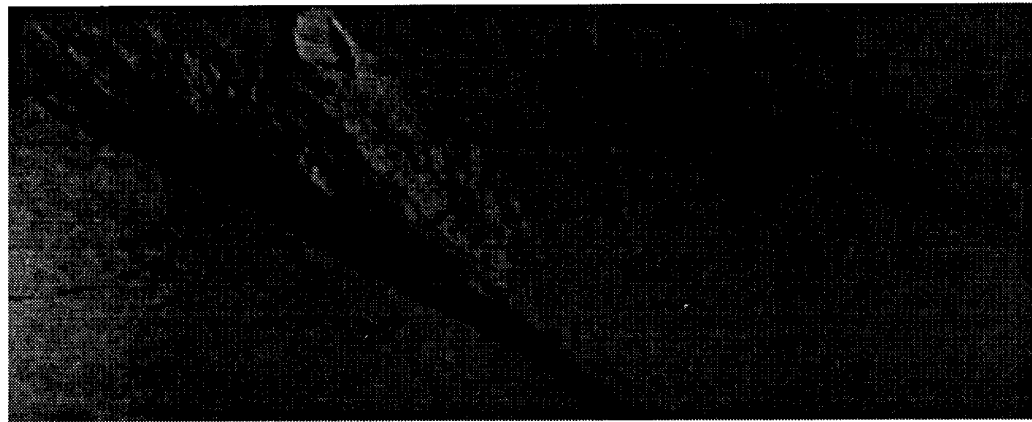
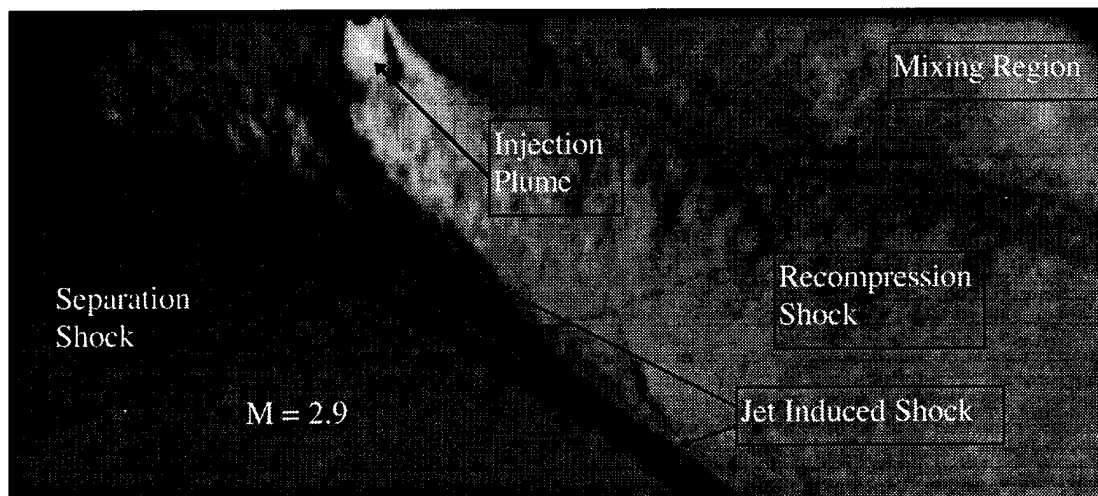


Figure 5.1: Shadowgraph of Flowfield.



(a) Adiabatic Injection

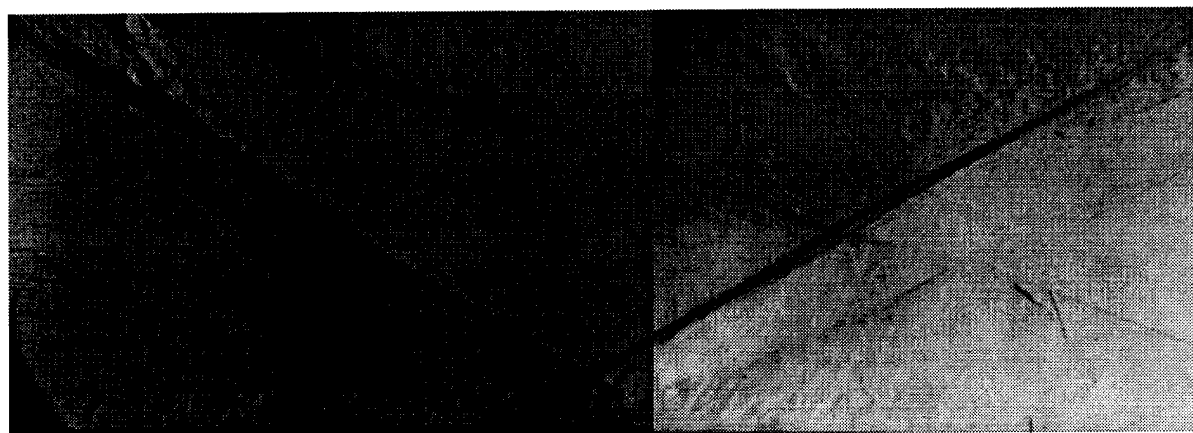


(b) Heated Injection

Figure 5.2: Schlieren of Injector Region.

Schlieren of Complete Flowfield Through Optical Grade Plexiglas Windows

(a)



Schlieren of Injector and Mixing Regions Through Optical Grade Glass Windows

(b)

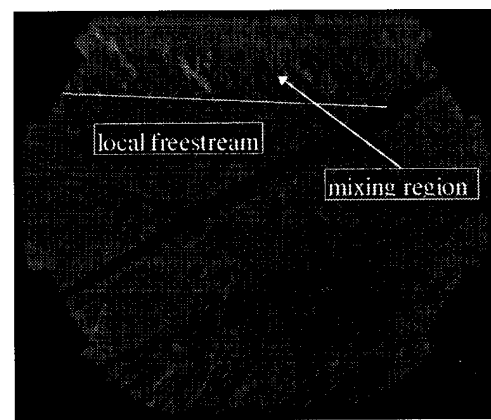
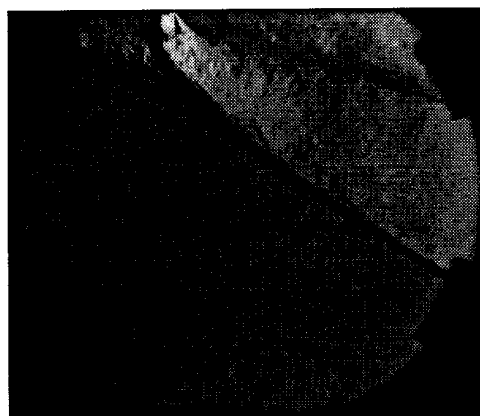


Figure 5.3: Schlieren of Flowfield.

Schlieren of Lambda Shock Formation

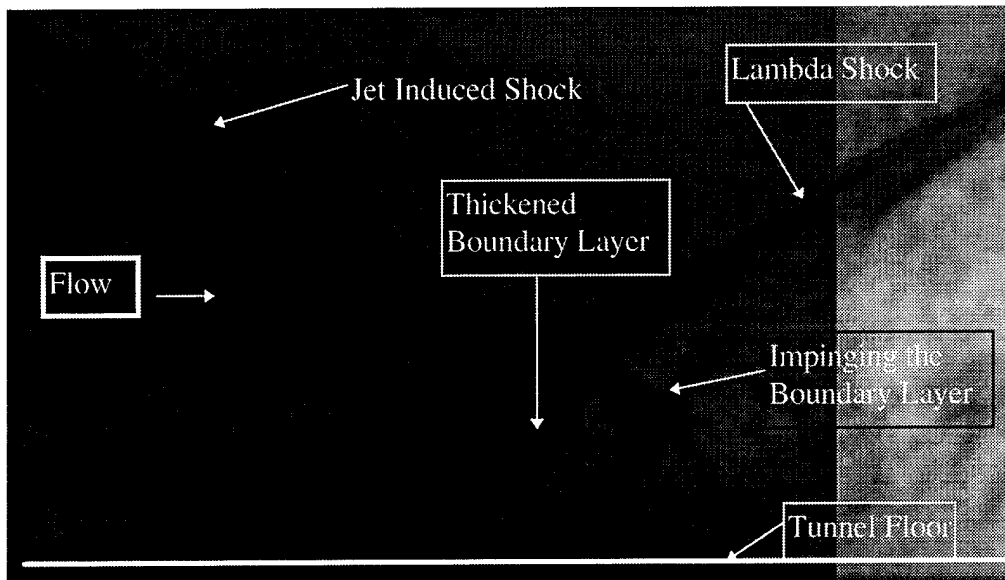
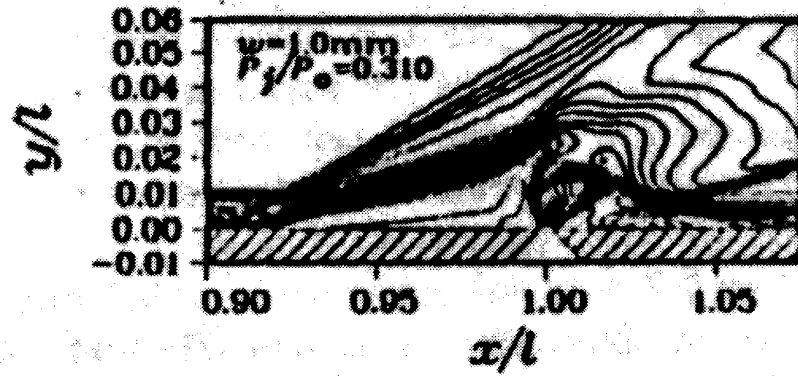
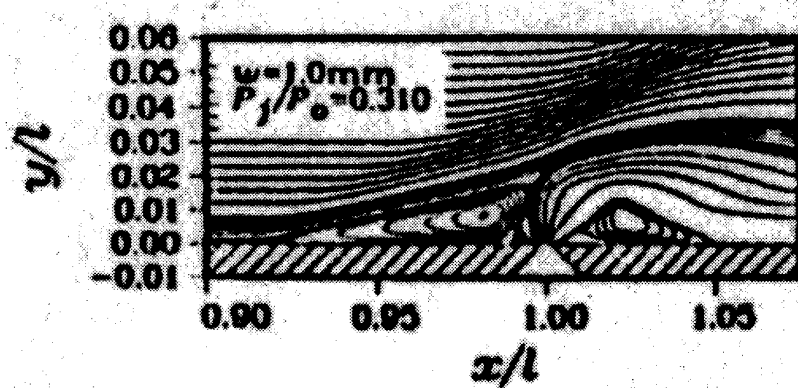


Figure 5.4: Schlieren of Lambda Shock.

Previous Injector Simulation with a Similar Flowfield



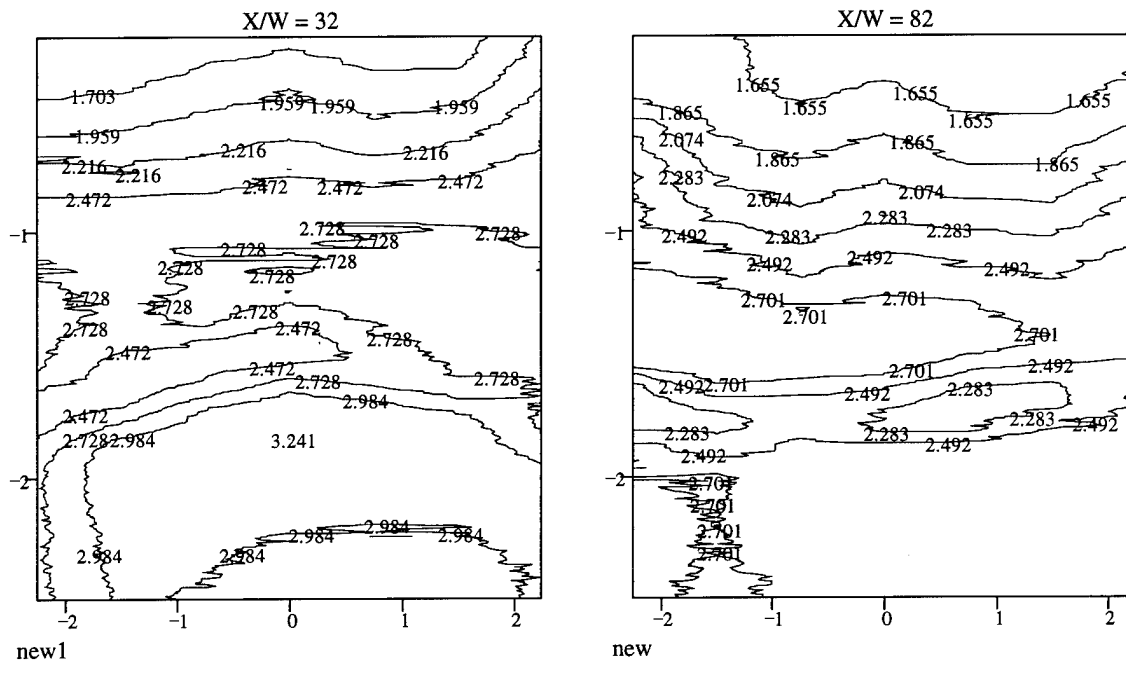
(a) Mach Profile



(b) Stream Function

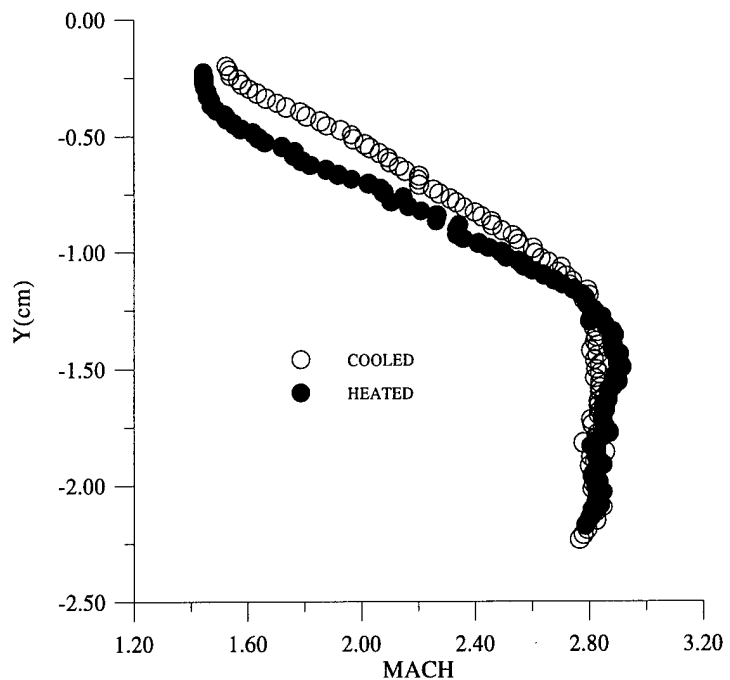
Figure 5.5: Rizzetta's Mach Profile and Stream Function for a 2D Injector Model [4].

Y-Z Axis Mach Number Contour Plots

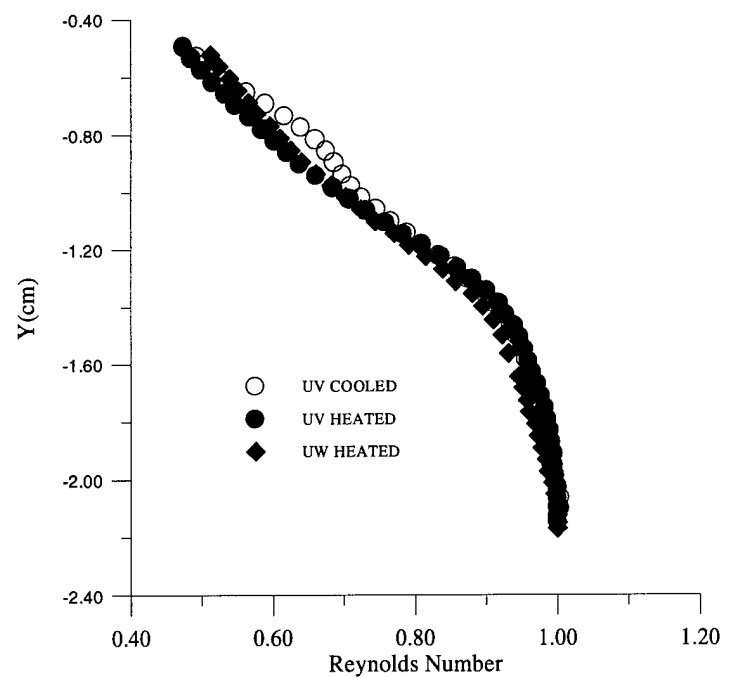


Y-Axis Vertical, Z-Axis Horizontal

Figure 5.6: Two-Dimensional Mach Profiles.

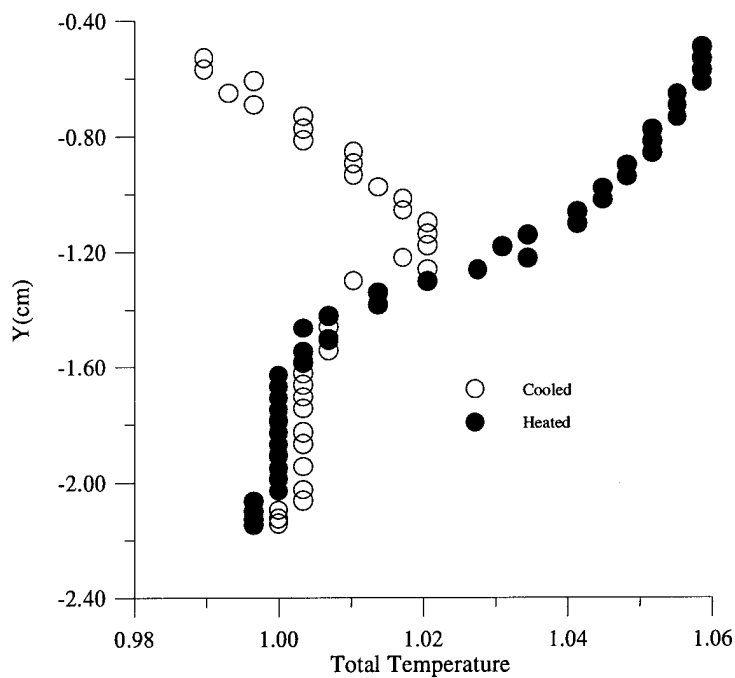


(a) Mach profile from conventional probes

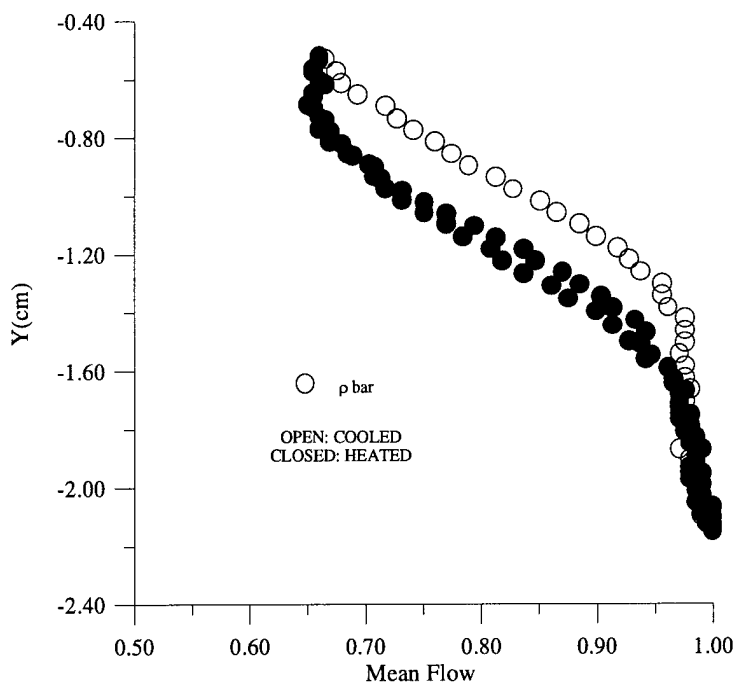


(b) Cross-film Reynolds number

Figure 5.7: Mach number and Reynolds number.

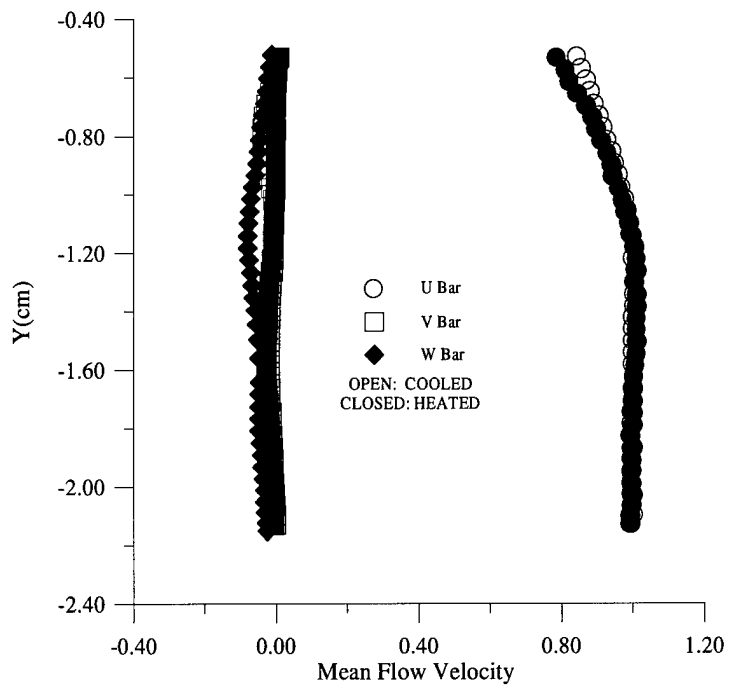


(a) Cross-film total temperature

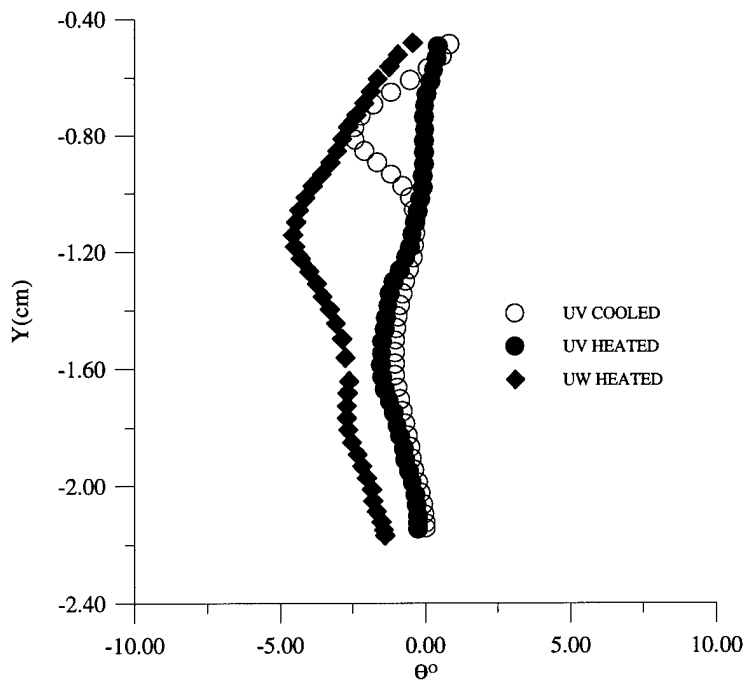


(b) Cross-film measured average density

Figure 5.8: Cross-film measured total temperature and average density.

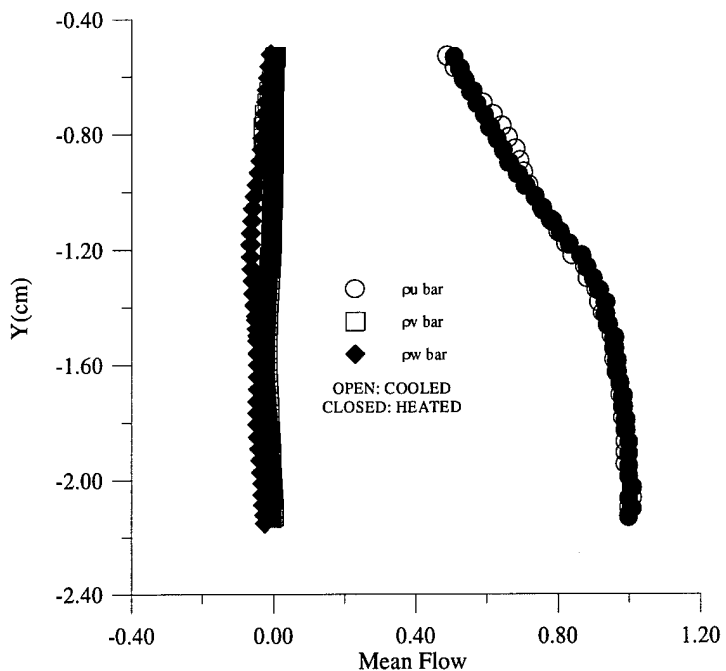


(a) Mean flow velocity

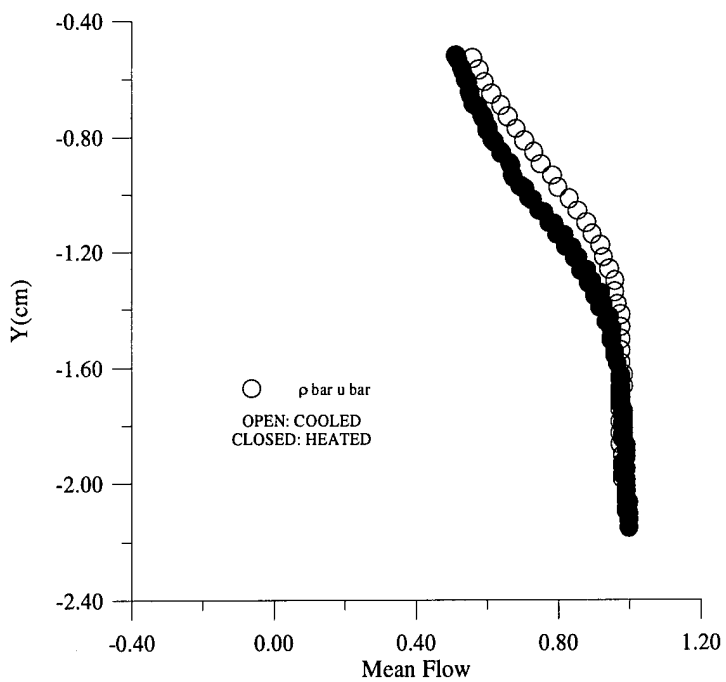


(b) Mass flux flow angle

Figure 5.9: Mean flow velocity and mass flux flow angle.

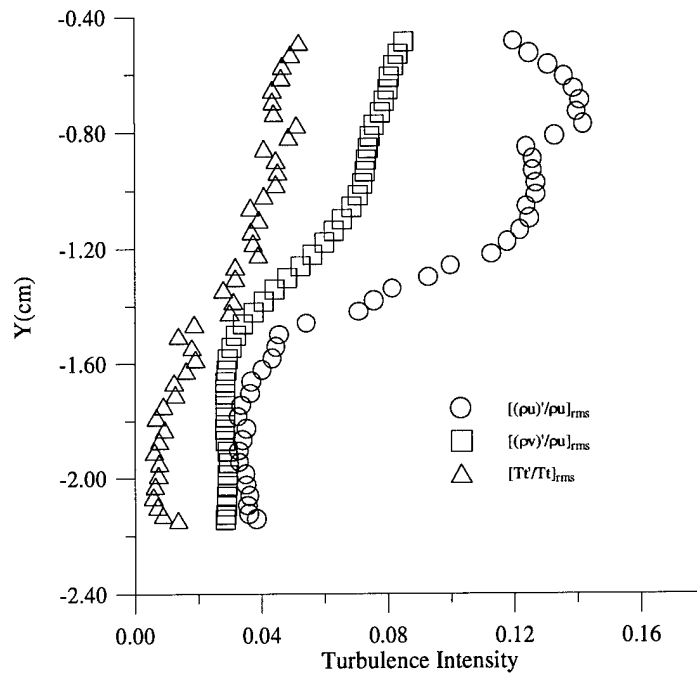


(a) Mass flux

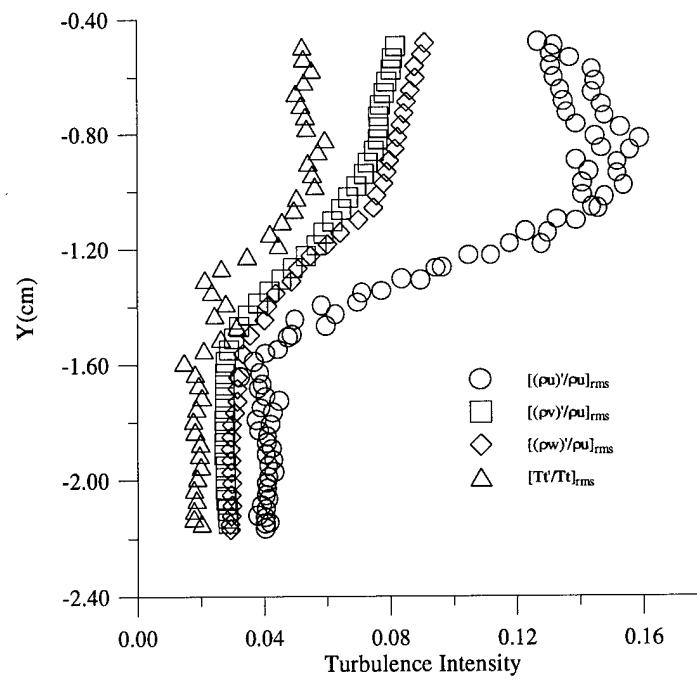


(b) Mass flux.

Figure 5.10: Mass flux data non-dimensionalized by local freestream value.

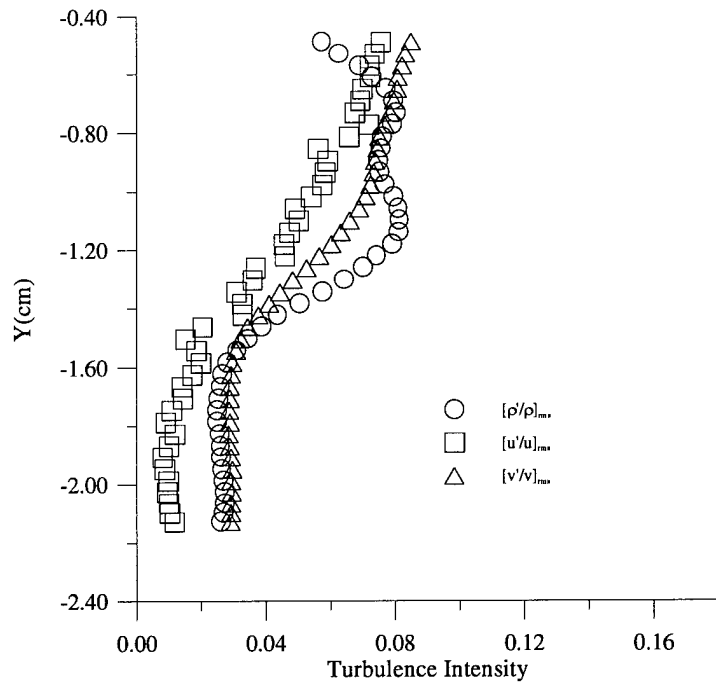


(a) Cold Injection Turbulence Intensity

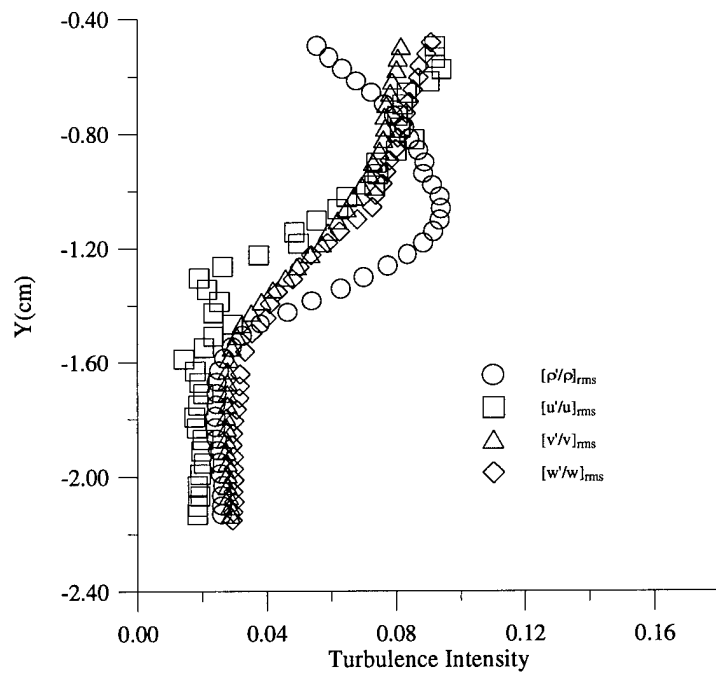


(b) Hot Injection Turbulence Intensity

Figure 5.11: Cross-film turbulence intensity data.

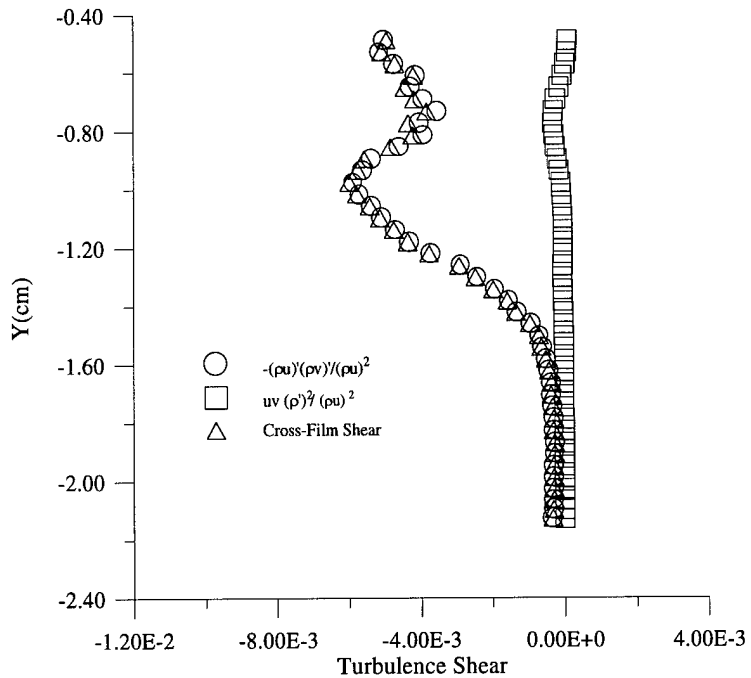


(a) Cold Injection Separated Turbulence Intensities

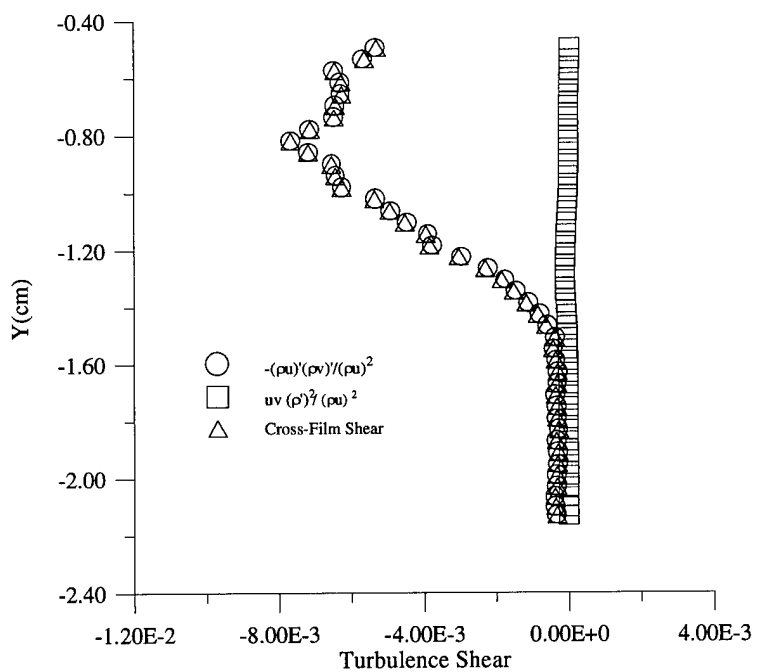


(b) Hot Injection Separated Turbulence Intensities.

Figure 5.12: Cross-film separated turbulence intensities.

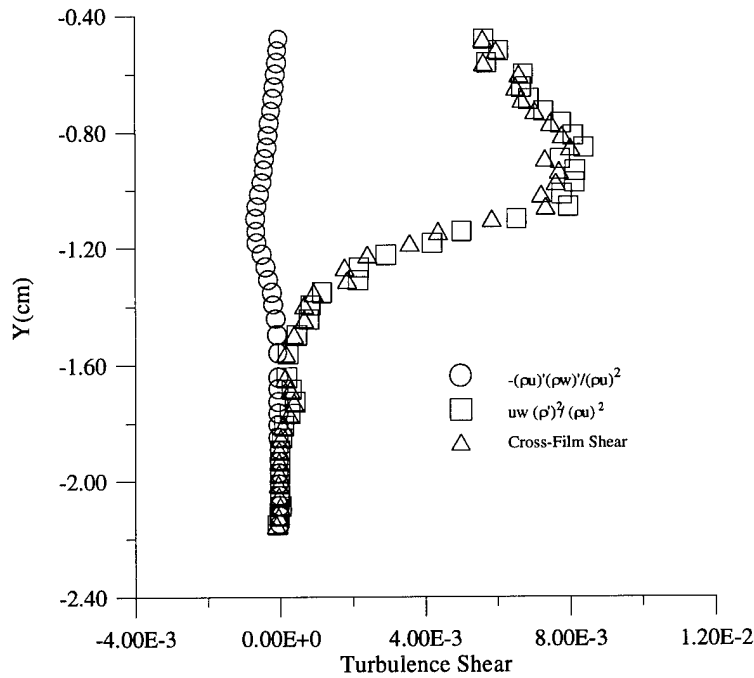


(a) Cold Injection Compressible Shear Terms

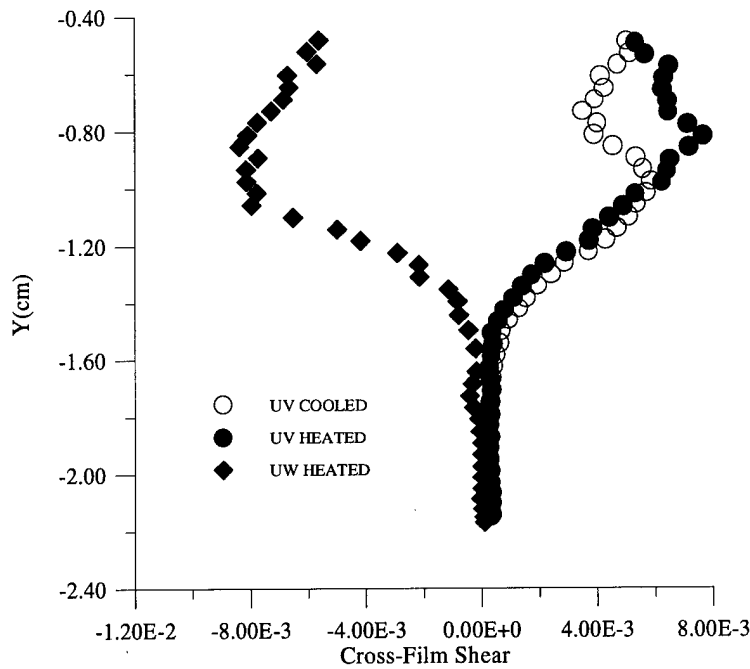


(b) Hot Injection Compressible Shear Terms

Figure 5.13: Cross-film transformed turbulent x-y shear data.

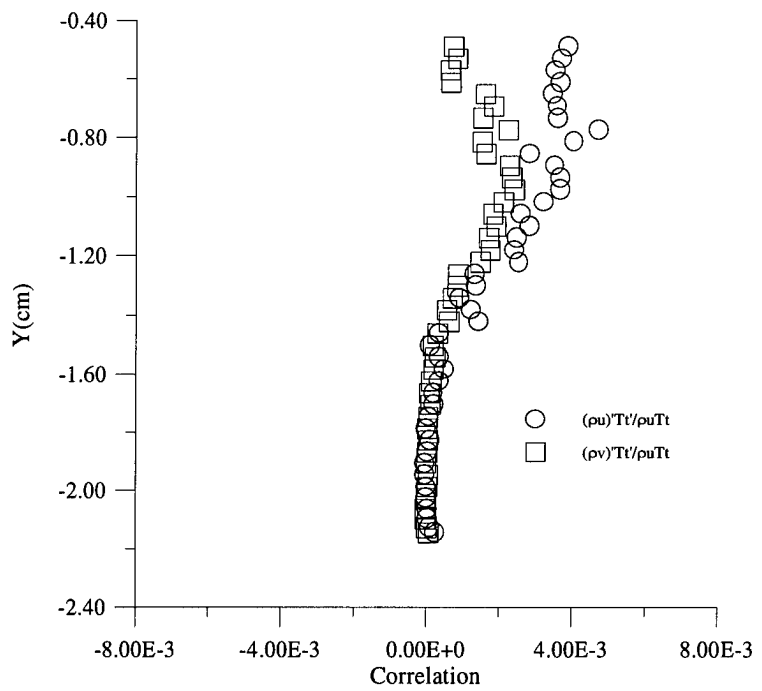


(a) Hot Injection x-z compressible shear term

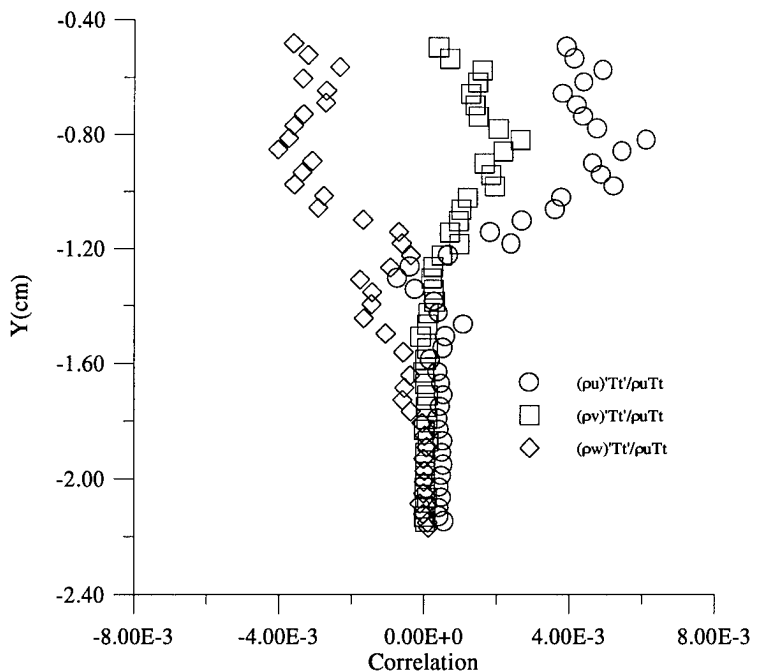


(b) Combined Reynolds Shear ($-\tau_{ij}^T$)

Figure 5.14: Cross-film transformed turbulence x-z shear data.

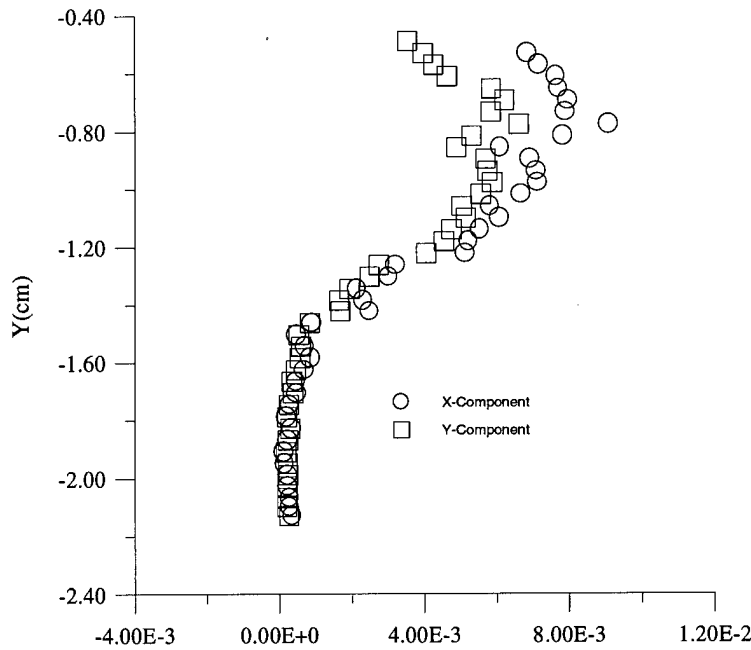


(a) Cold injection mass flux - total temperature fluctuation correlations

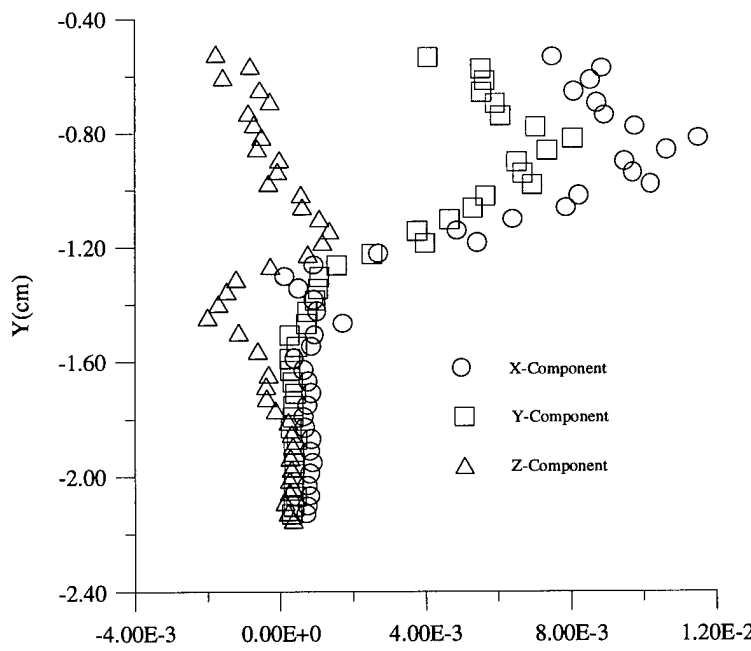


(b) Hot Injection mass flux - total temperature fluctuation correlations

Figure 5.15: Cross-film mass flux - total temperature fluctuation correlations.

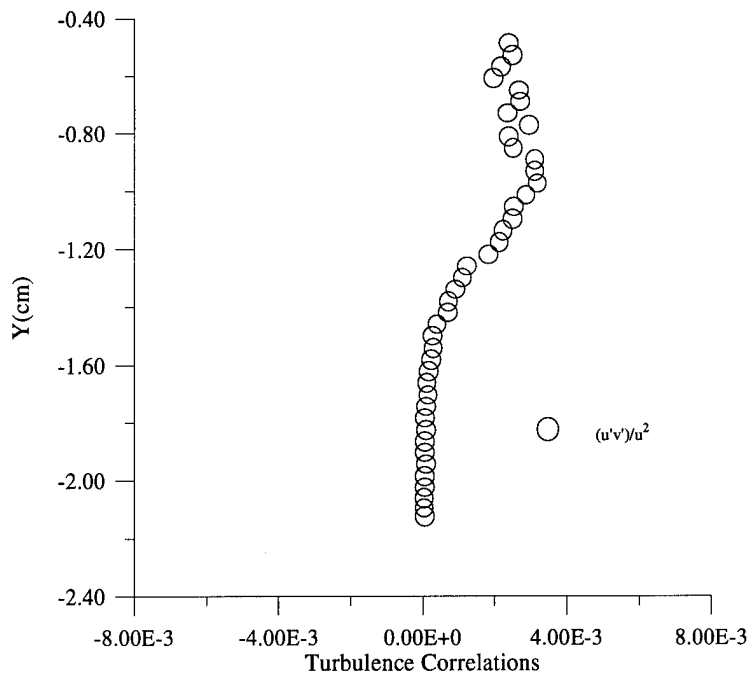


(a) Cold injected specific turbulent heat flux $\left(\frac{q_i^T}{C_p T_t \rho u} \right)$

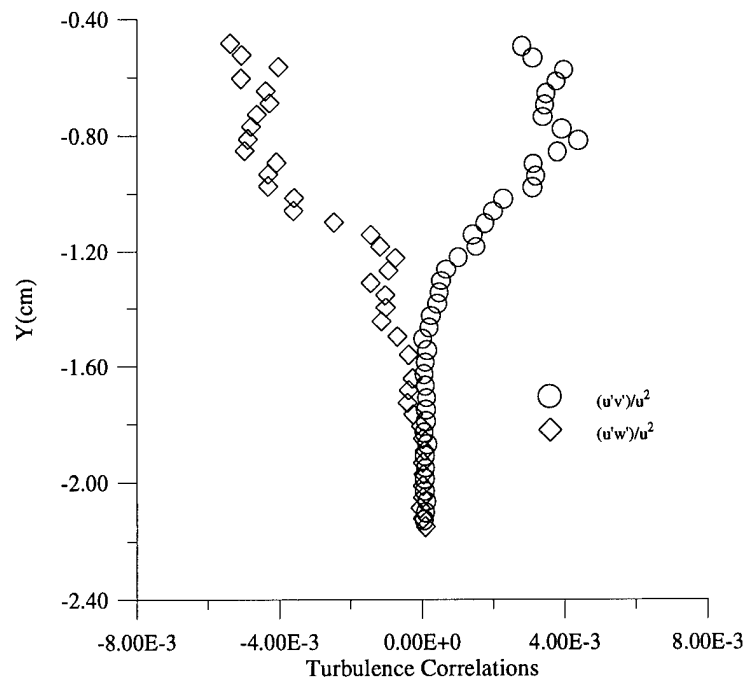


(b) Hot injected specific turbulent heat flux $\left(\frac{q_i^T}{C_p T_t \rho u} \right)$

Figure 5.16: Specific turbulent heat flux data.

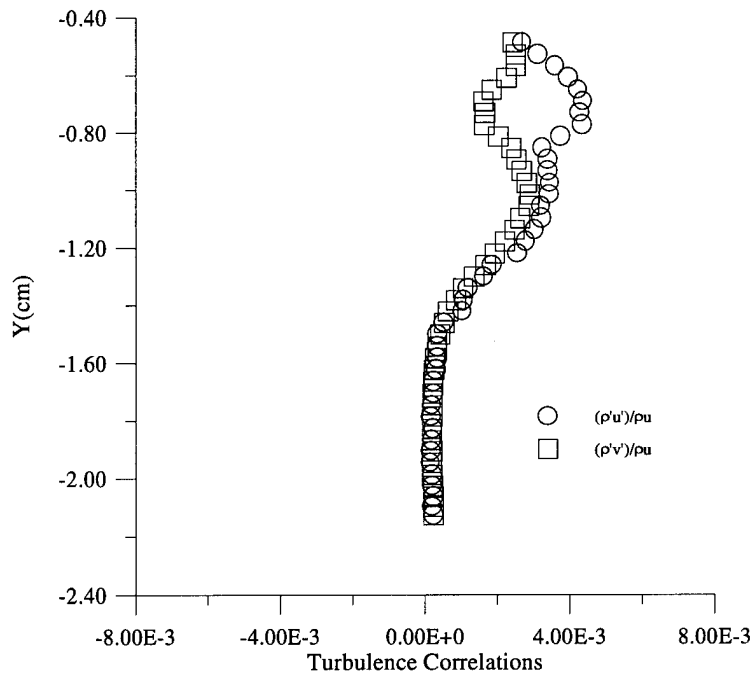


(a) Cold Injection velocity-velocity correlation

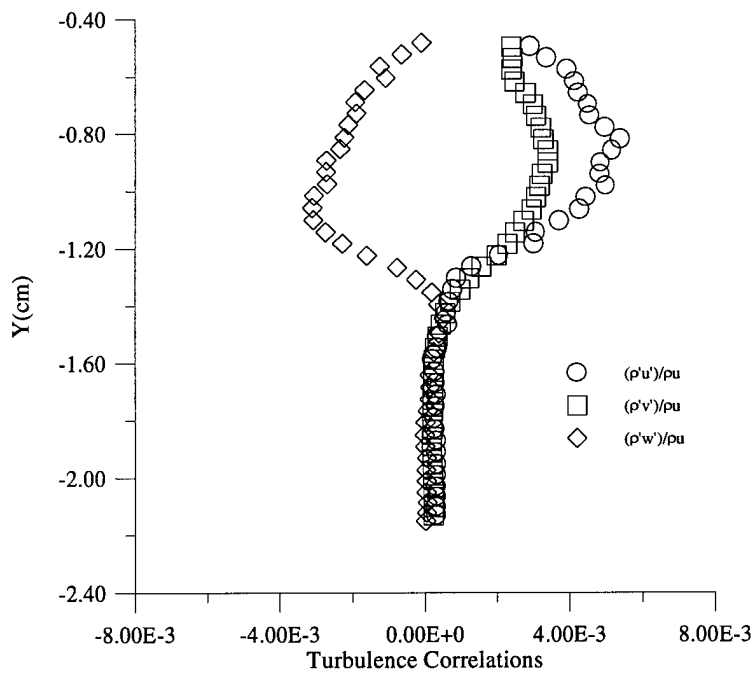


(b) Hot injection velocity-velocity correlation

Figure 5.17: Cross-film velocity-velocity correlation data.

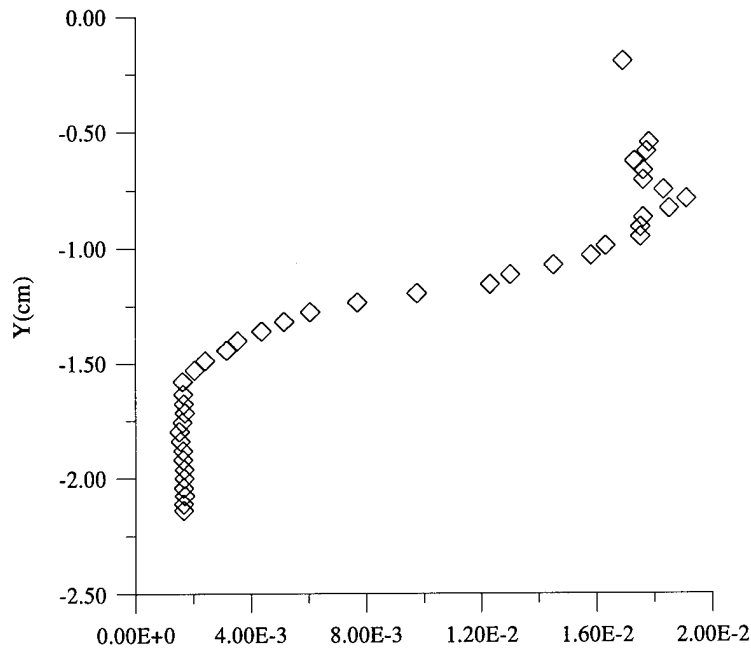


(a) Cold injection velocity-density correlations

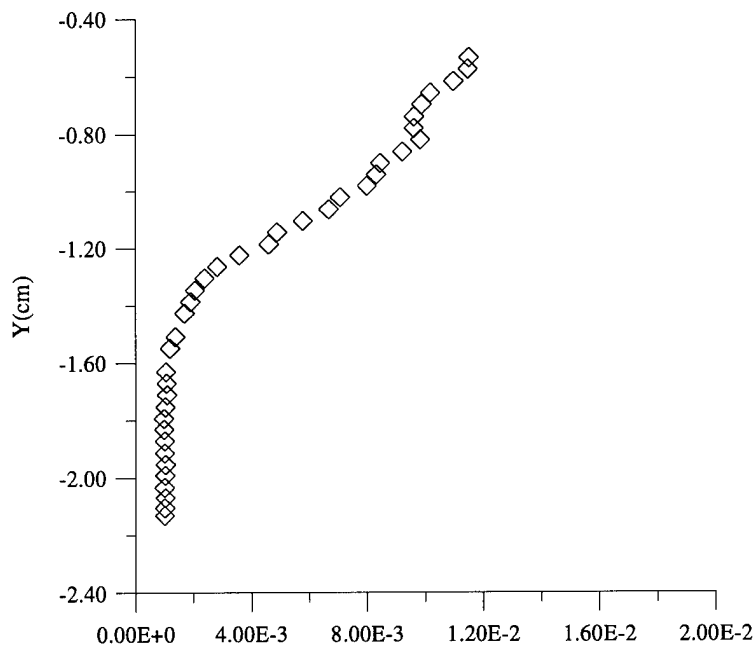


(b) Hot injection velocity-density correlation

Figure 5.18: Cross-film velocity-density correlations.

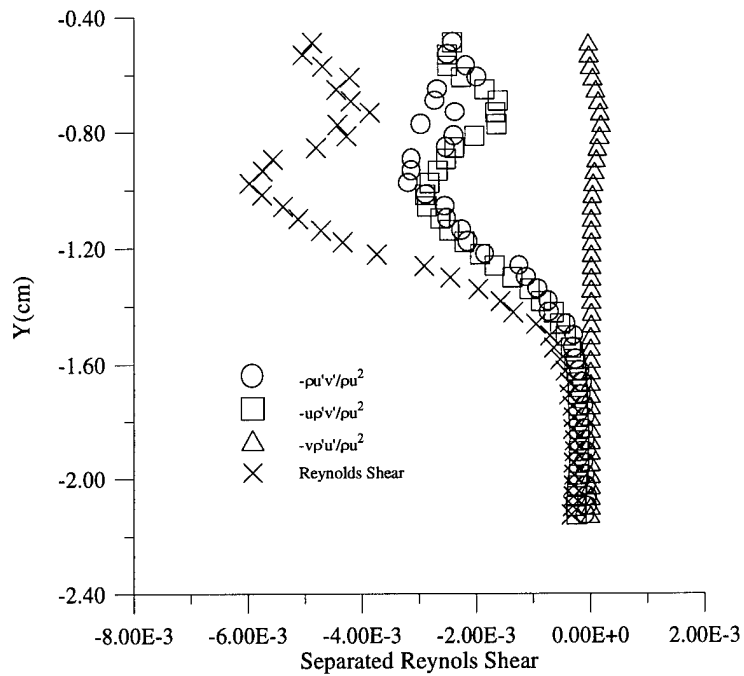


(a) Tke data (compressible)

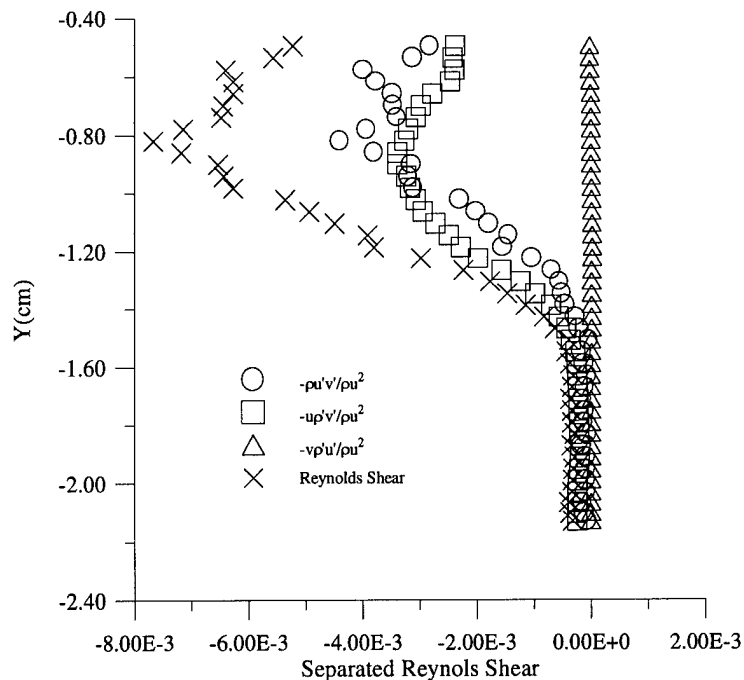


(b) Tke (incompressible)

Figure 5.19: Cross-wire TKE data (Heated Case Only).

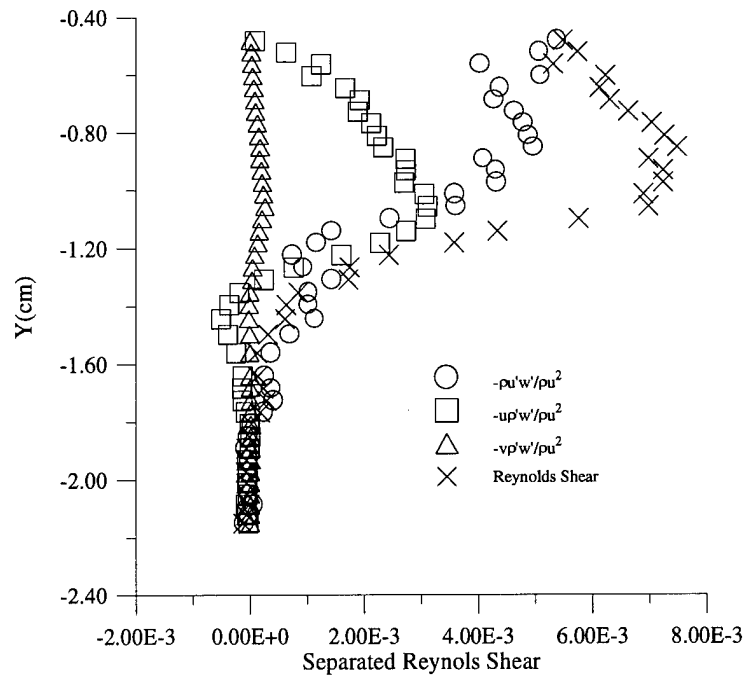


(a) Cold injection separated Reynolds shear

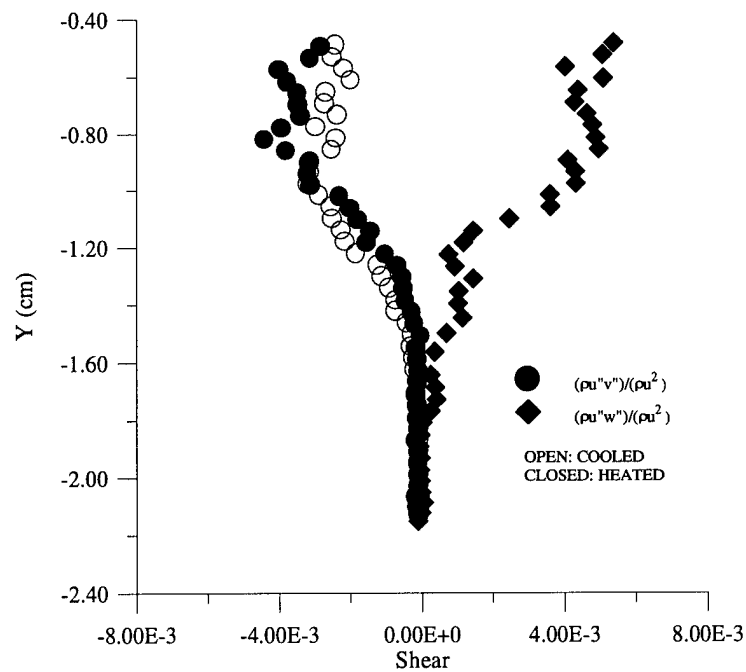


(b) Hot injection separated Reynolds shear

Figure 5.20: Cross-film separated Reynolds shear (xy).

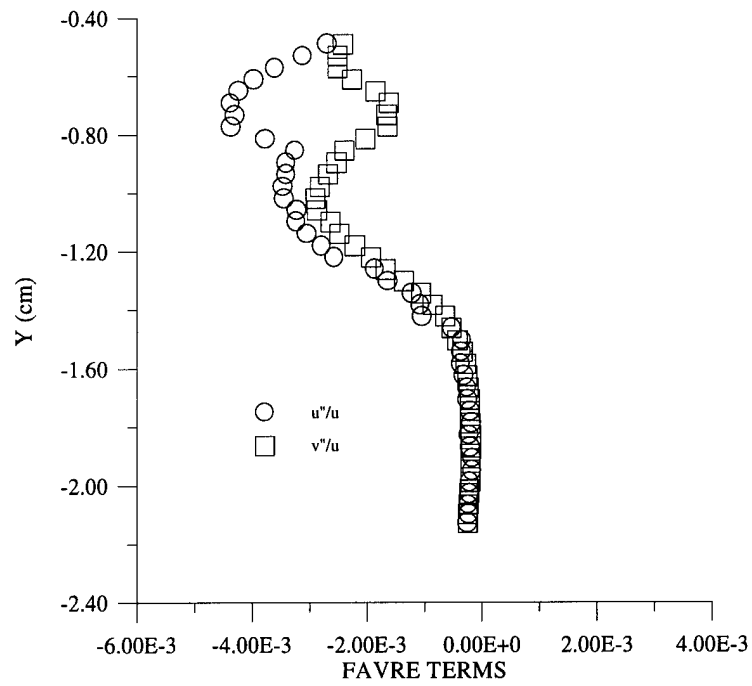


(a) Separated Reynolds shear (xz)

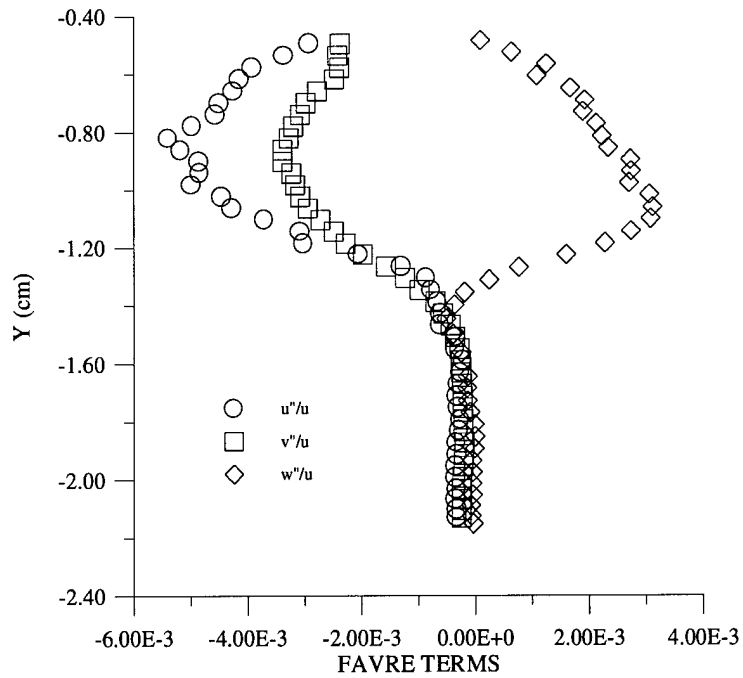


(b) Favre Shear

Figure 5.21: Cross-film separated Reynolds shear (xz) and Favre shear.

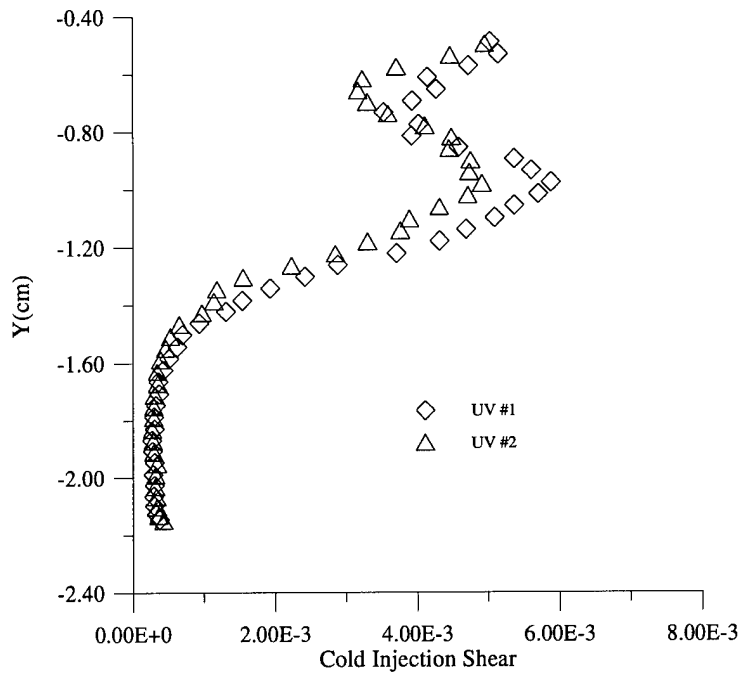


(a) Cold injection Favre terms

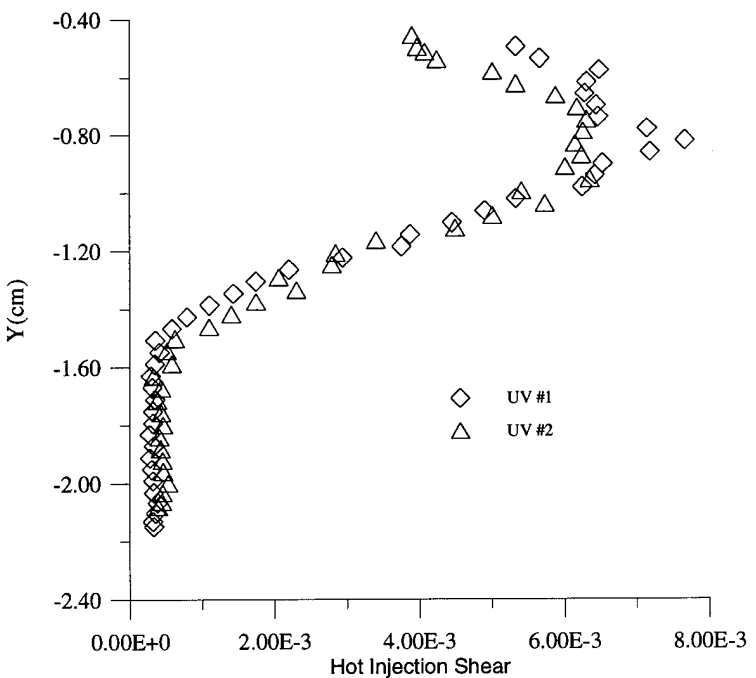


(b) Hot injection Favre terms

Figure 5.22: Cross-film Favre variable data.

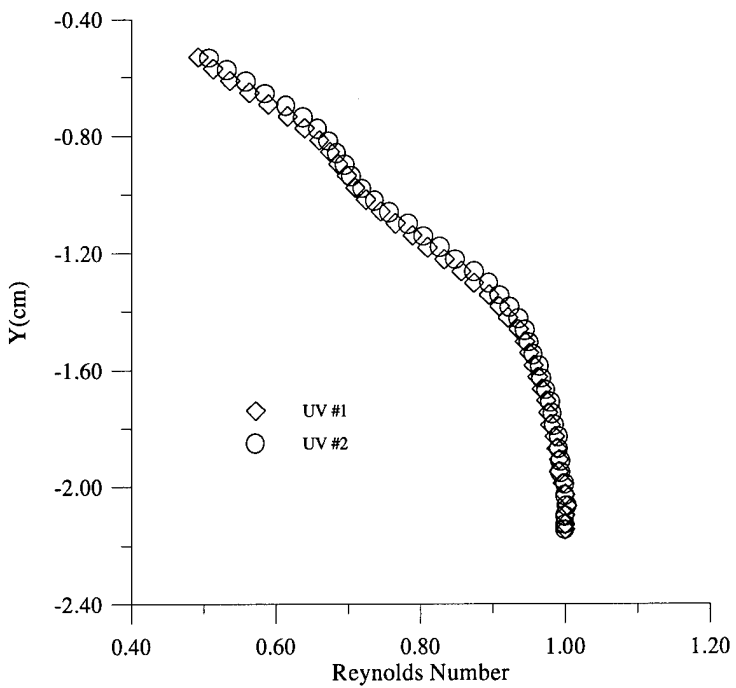


(a) Cold Injection Shear ($-\tau_{xy}^T$) from two data sets

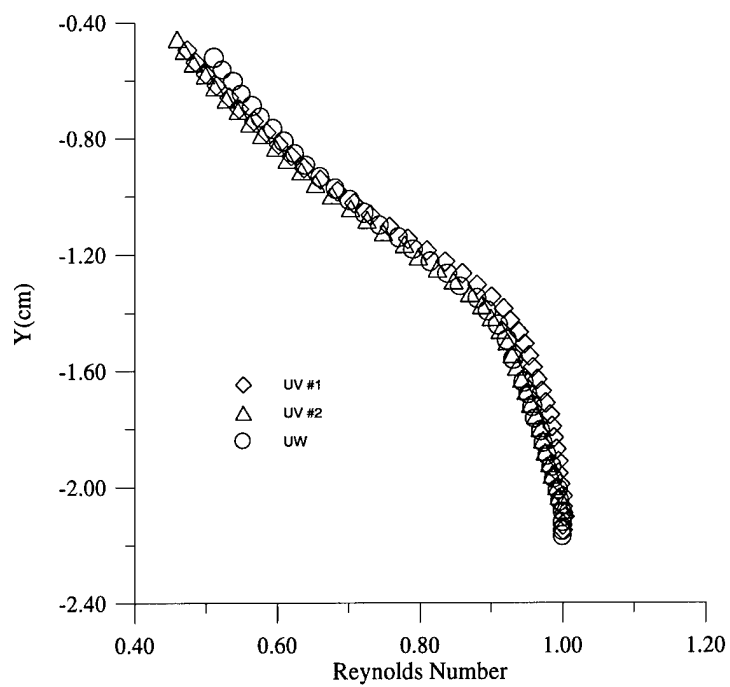


(b) Hot Injection Shear ($-\tau_{xy}^T$) from two data sets

Figure 5.23: Cross-film shear repeatability.

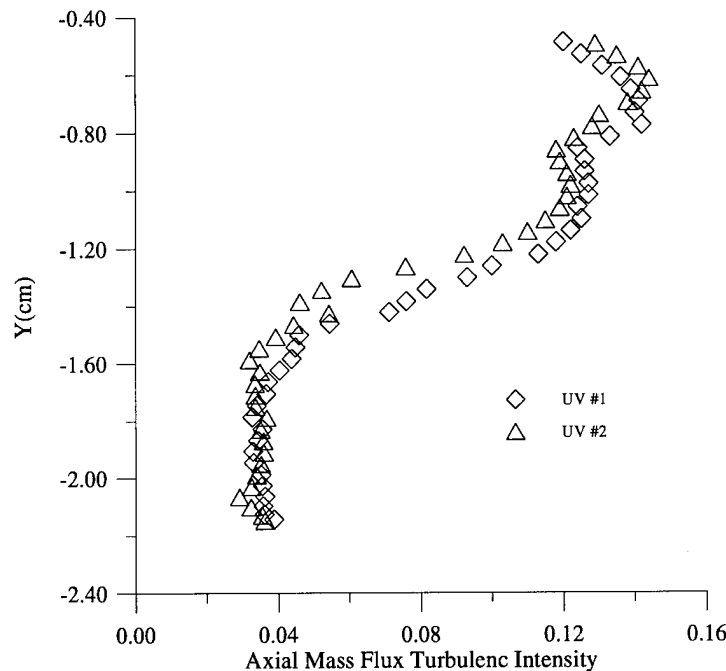


(a) Cold Injection Reynolds number from two data sets

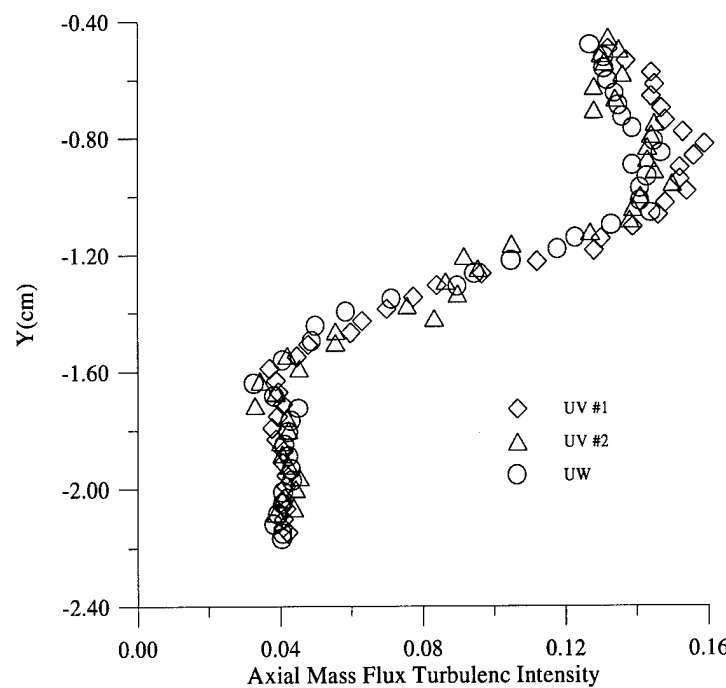


(b) Hot injection Reynolds number from three data sets

Figure 5.24: Non-dimensionalized Reynolds number repeatability.

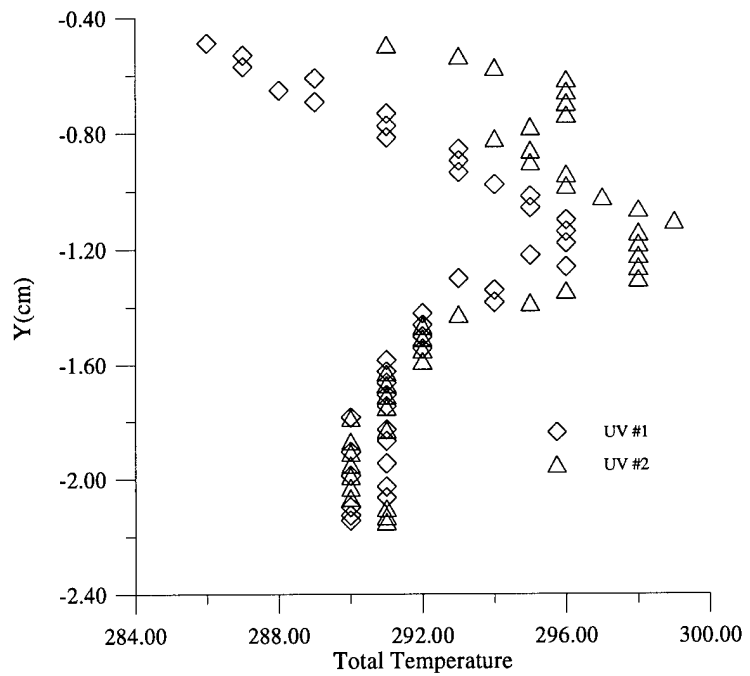


(a) Cold injection axial mass flux turbulence intensity from two data sets

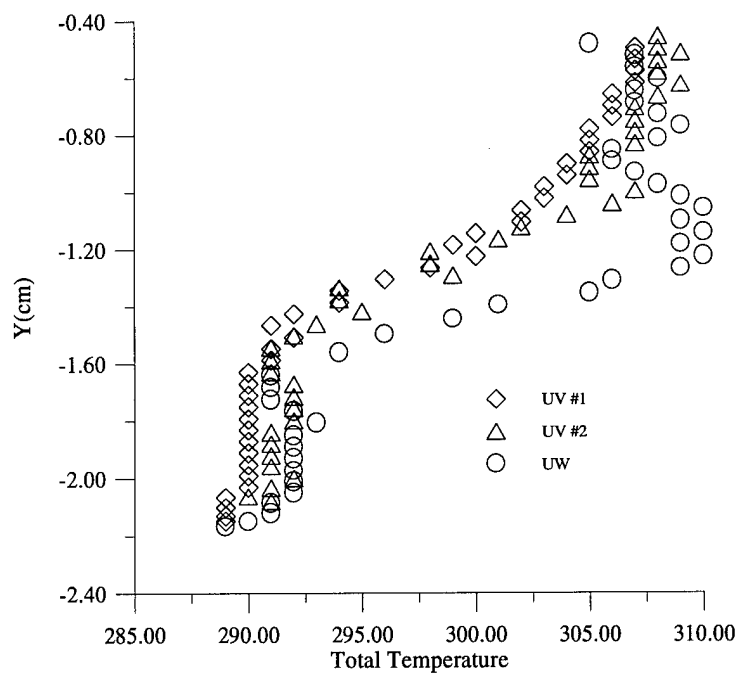


(b) Hot injection axial mass flux turbulence intensity from three data sets

Figure 5.25: Axial mass flux turbulence intensity repeatability.



(a) Cold injection total temperature from two data sets



(b) Hot injection total temperature from three data sets

Figure 5.26: Total temperature repeatability.

Appendix A

Error Analysis

Regardless of the effort to insure the accuracy of any experimental measurement, inherent scatter or error will occur. The purpose of this uncertainty analysis is to accurately account for all potential errors within the experimental processes for which this study was performed, and to predict the effect of a single error propagating through the calculation of other variables.

Several individual components often contribute to the total error of a particular measurement. It is assumed that the maximum of each individual error will not occur simultaneously with the maximum of other errors. With this assumption, the Euclidean Norm [22], denoted L_2 , was used to approximate the total error associated with an experimental measurement technique. The L_2 norm is given by

$$\epsilon_x = \left[\sum_{i=1}^n \epsilon_i^2 \right]^{1/2} \quad (A-1)$$

where i indexes the individual errors during the measurement of the x component.

A.1 Cross-Film Position Error

Multiple overheat cross-film anemometry was performed with six individual runs using the same probe at the same starting position. Averaging was performed twice to reduce the

potential amount of error from run to run. Initially the raw position voltage was averaged in blocks of 41 data points to coincide with the hot-film digital processing. Then, the position voltage and overheat information was saved in an individual data file. These six data files were combined to form the necessary input files to be used by MSHeAR [19] discussed in Sec. (4.5). The position voltage from all the data sets was combined and then averaged for each of the 49 data points that defined the flowfield. This averaged any drift that occurred during the 6 different runs. It was this final averaged voltage that was converted to a position via a linear conversion. Through this process, the computed position relative to the measured position differed by 0.457 mm. Also, the probes flexed during data taking and was seen to move vertically 1.3 mm and axially 2.5 mm as seen in Fig. (A.1). Therefore, the combined vertical position error was $\epsilon_y = 1.4$ mm and the axial position error was $\epsilon_x = 2.5$ mm.

A.2 Cross-Film Angle Error

Cross-film angle error for the UV component probe is also approximated. The maximum probe angle deflection, considering the flex along the vertical length of its 5.08 cm shaft, was measured to be -2.86°. Using the angle definitions as defined in Sec. (3.3.3), the recorded deflection was added to the defined angles used in the input deck of MSHeAR [19]. It is important to note that the calibration method would most likely remove any error associated with the probe flex, only if the probe experienced the same amount of flex during calibration. The flex described above was measured at its highest point, with the entire probe and shaft cantilevered in the flow. However, the flex at the centerline

calibration point was most likely smaller, because only half the probe shaft was cantilevered in the flow. Therefore, a flow angle error in the x-y plane of $\epsilon_\phi=1.5^\circ$ is predicted. A deviation in the angle definition of UW component probe is caused by the probe not being parallel to x-axis. However, this error would be fully corrected with the calibration at the same offset. This is justified if the probe does not twist in x-z plane as it traverses along the y-axis during data acquisition.

A.3 Random Error Analysis

This analysis follows the method used by Bowersox and McCann [27].

A.3.1 Mean Flow

The Mach number was computed using Eqn. (4.2) that was curve fit for P, which is the ratio of experimentally measured cone-static and Pitot pressure. The error in P includes the pressure transducer calibration curves which had a standard deviation of 0.2% for the plenum transducer and an estimated 0.9% [17] for the Pitot and cone-static transducer. The combined pressure transducer error, published by the manufacturer was estimated at $\epsilon_P = 2.0\%$. To calculate the Mach number error, the first derivative of Eqn. (4.2) is taken with respect to P to calculate the associated sensitivity. It can be shown that the Mach number error is approximately $\epsilon_M = (0.7 - 1.0)\epsilon_P$ or $\epsilon_{M1} = 2.0\%$. The error of the Mach number associated with the drift of the traverse data results in = 2.3%. Using the Euclidean norm, the total Mach number error was $\epsilon_M = 3.04\%$. Other mean flow parameter errors are calculated by approximating the effect the Mach number error

contributes to the calculation of that parameter. This is accomplished through a binomial expansion of the equation in question. The errors below are considered to be the maximum possible error, but do not constitute the actual error within the results. These errors are summarized below in Table (A.1), and are presented as a percentage of the measured values in Table (5.4).

Table A.1 Mean Flow Error

ϵ_{MACH}	3.0%
$\epsilon_{TEMPERATURE}$	3.1%
$\epsilon_{VELOCITY}$	1.6%
$\epsilon_{STATIC PRESSURE}$	3.0%
$\epsilon_{TOTAL PRESSURE}$	13%
$\epsilon_{DENSITY}$	3.7%
$\epsilon_{MASS FLUX}$	4.0%

Table (A.1) does not include the Mach number error associated with the 1.3 mm flex component added. This contributes an added 6.5% error to Mach number. However, the flex is considered to exist through both the hot-film and mean flow data and should only be considered when determining the absolute position of the data within the coordinate system and not between the calculation of the individual pieces of measured information. This assumption is justified by the flow quality discussed in Sec. (5.5).

A.3.2 Hot-Film

A hot-film random error analysis is performed considering the influence the mass-flux error ϵ_{pu} in the computation of hot-film information. A summary of this information is presented below in Table A.2.

Table A.2 Hot-Film Error

ϵ_{pu}	4.5%
$\epsilon_{(Reo^2)}$	4.5%
ϵ_{Rex}	6.8%
$\epsilon_{(u''/u)}$	16.0%
ϵ_{shear}	12.0%

These errors show the sensitivity of the solution of the individual variable based on an initial theoretical 4.5% mass flux error.

Probe Flex and Angle Change During Data Acquisition

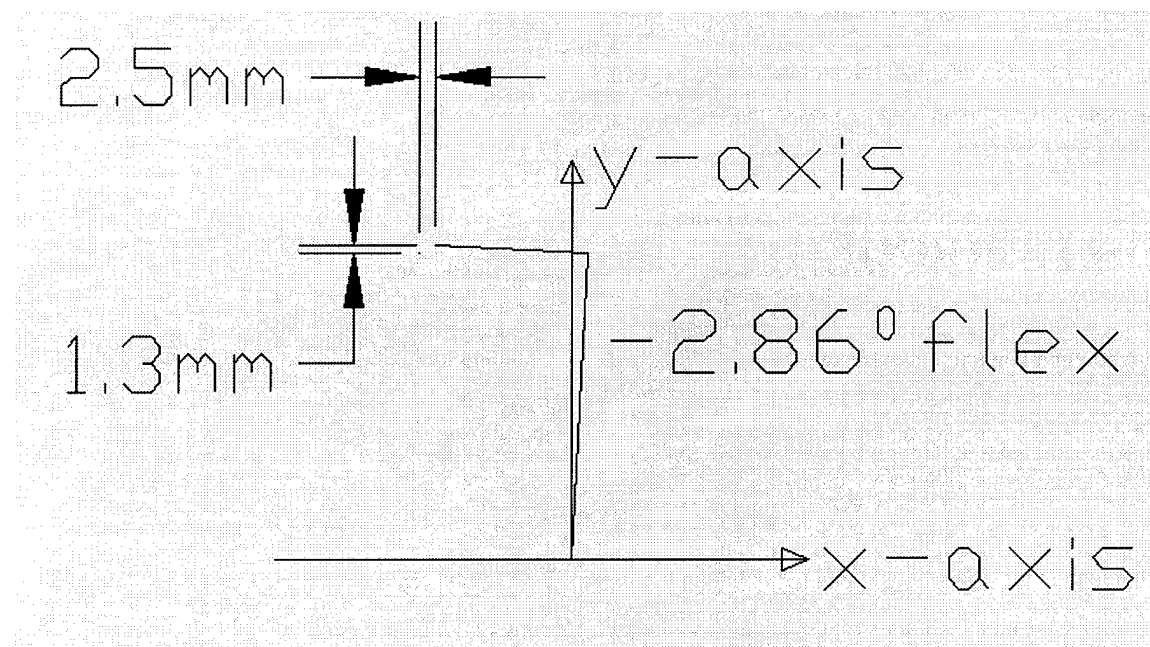


Figure A.1: Probe Flex Measurement.

Appendix B

Design of the Air Cooler

This design procedure was computed using a Mathcad 5.0+ worksheet and presents information at a higher significant figures than the expected accuracy. The procedure for designing the heat exchanger is discussed below. The purpose of the heat exchanger is to cool the air from 295 to 273 Celsius at the entrance of the injector. This will be accomplished by submerging a length of 1.27 cm inner diameter tubing in an ice-slush mixture at 270 Celsius. The air properties [9] are assumed at atmospheric pressure and with an average temperature, Tmean.

$$T_{mean} := 284 \cdot K$$

$$D := 0.0127 \cdot m$$

$$\mu := 17.66 \cdot 10^{-6} \cdot \text{newton} \frac{\text{sec}}{\text{m}^2}$$

$$T_{surface} := 270 \cdot K$$

$$k := 25.02 \cdot 10^{-3} \cdot \frac{\text{watt}}{\text{m} \cdot \text{K}}$$

$$T_{entrance} := 295 \cdot K$$

$$T_{exit} := 273 \cdot K$$

$$Pr := .7116$$

$$C_p := 1004 \cdot \frac{\text{joule}}{\text{kg} \cdot \text{K}}$$

Assumptions:

1. Steady-state conditions
2. Incompressible flow with constant properties
3. Negligible kinetic and potential energy and flow work changes
4. Fully developed flow throughout the tubing
5. Average convection coefficient for Turbulent flow
6. Surface temperature is constant along the length of the pipe
7. Negligible tube wall thermal resistance
8. Smooth wall inside the pipe

The mass of the air flowing through the heat exchanger is

$$\dot{m} := 1.81 \cdot 10^{-2} \frac{\text{kg}}{\text{sec}}$$

The Reynolds number was calculated through the tube and was found to be fully turbulent inside the heat exchanger.

$$ReD := \frac{4 \cdot \dot{m} D}{\pi \cdot D \cdot \mu} \quad ReD = 1.027529 \cdot 10^5$$

The friction factor inside a smooth pipe is an important factor in determining the heat transfer occurring between the pipe and the air. A correlation from Gnielinski [28] is used below

$$f := (1.82 \cdot \log(ReD) - 1.64)^{-2} \quad f = 0.017866$$

An experimental correlation for the Nusselt number for turbulent air through a circular pipe is attributed to Petukhov, Kirillov, and Popov [29] where f is the friction factor. This correlation has approximately 10% error associated with its use.

$$NuD := \frac{\left(\frac{f}{8}\right) \cdot ReD \cdot Pr}{1.07 + 12.7 \cdot \sqrt{\frac{f}{8} \left(\Pr^{\frac{2}{3}} - 1\right)}} \quad NuD = 172.213079$$

For a constant surface temperature problem, it is desirable to know the average convection coefficient, h_{bar} , and is defined as

$$h_{bar} := \frac{NuD \cdot k}{D} \quad h_{bar} = 339.273326 \cdot \text{kg} \cdot \text{sec}^{-3} \cdot \text{K}^{-1}$$

where the h_{bar} units are equivalent to $\text{W/m}^2 \text{ K}$.

It is well known that the temperature decays exponentially with distance along the tube axis, and using the general result in [12], the necessary length to cool the air to the desired temperature is

$$L := \frac{-\dot{m}C_p}{h_{\text{bar}}\pi D} \cdot \ln\left(\frac{T_{\text{surface}} - T_{\text{exit}}}{T_{\text{surface}} - T_{\text{entrance}}}\right) \quad L = 2.846419 \cdot m$$

A factor of safety is used to account for any errors in the assumptions and correlations, and to determine the final length to be used in the design of the heat exchanger.

$L=L^*fs$ where fs is the factor of safety.

$fs=5.35$

$L = 15.2$ meters

$L = 50.0$ feet

This is the length required to cool the injected air to 273 K.

Appendix C

Reference Temperatures and Pressures

Measured Experimental Injector, Plenum, and Wall Temperatures

UV#1 Cold Injection Case Temperatures				UV#2 Cold Injection Case Temperatures			
Overheat	injector	plenum	wall	Overheat	injector	plenum	wall
1.9	32.3	71.3	42.5	1.9	31.8	71.2	46
1.8	32.4	71.3	43	1.8	31.8	71.2	44
1.7	32.4	71.3	40.5	1.7	32	71.2	44
1.6	32.4	71.4	41.5	1.6	32	71.1	44
1.5	32.4	71.6	41	1.5	32.3	71.4	42
1.4	32.4	71.3	41	1.4	32.3	71.4	41
Average Farenheit	32.4	71.36667	41.58333		32.03333	71.25	43.5
Average Kelvin	273.37	295	278.47		273.169	294.95	279.54
UV#1 Hot Injection Case Temperatures				UV#2 Hot Injection Case Temperatures			
Overheat	injector	plenum	wall	Overheat	injector	plenum	wall
1.9	132	67.1	98	1.9	130.5	71.8	97
1.8	134	67.9	100	1.8	130.6	71.8	103.5
1.7	131	67.9	99	1.7	130	71.8	102
1.6	130	68	100	1.6	130.8	71.8	102.5
1.5	132	68	99	1.5	131.9	71.8	102.5
1.4	132	68	100	1.4	132	71.8	101
Average Farenheit	131.8333	67.81667	99.33333		130.9667	71.8	101.417
Average Kelvin	328.613	293.048	310.556		328.132	295.261	311.715
UW Hot Injection Case Temperatures							
Overheat	injector	plenum	wall				
1.9	133	71.8	104				
1.8	135.5	72.7	105				
1.7	134	73.4	104.5				
1.6	132	71.4	101				
1.5	130	71.5	102.5				
1.4	133	71.6	102.5				
Average Farenheit	132.9167	72.06667	103.25				
Average Kelvin	329.9167	295.409	312.733				

Table C.1: Measured Temperature.

Measured Injector and Plenum Pressures

UV#1 Cold Injection Case Pressures					UV#2 Cold Injection Case Pressures				
units	value	injector	plenum	ratio	units	value	injector	plenum	ratio
psi	largest	8.92	29.75	0.3036	psi	largest	8.91	29.727	0.303
psi	smallest	8.73	29.14	0.2975	psi	smallest	8.81	29.34	0.297
psi	average	8.78	29.35	0.2994	psi	average	8.85	29.568	0.3
atm	average	0.597	1.996		atm	average	0.602	2.011	
kPa	average	60.5	202.2		kPa	average	61.02	203.86	
UV#1 Hot Injection Case Pressures					UV#2 Hot Injection Case Pressures				
units	value	injector	plenum	ratio	units	value	injector	plenum	ratio
psi	largest	9.47	29.53	0.3236	psi	largest	9.45	29.47	0.323
psi	smallest	9.29	29.11	0.3191	psi	smallest	9.33	29.11	0.319
psi	average	9.41	29.27	0.3217	psi	average	9.41	29.29	0.321
atm	average	0.6401	1.991		atm	average	0.6401	1.9925	
kPa	average	64.88	201.8		kPa	average	64.9	201.9	
UW Hot Injection Case Pressures									
units	value	injector	plenum	ratio					
psi	largest	9.48	29.45	0.3225					
psi	smallest	9.31	28.91	0.3206					
psi	average	9.44	29.33	0.3217					
atm	average	0.642	1.995						
kPa	average	65.1	202.1						

Table C.2: Measured Pressures.

Appendix D

MSHEAR INPUT DECKS

UV#1 Input Deck for Cold Injection Case

14 September 1995

```
input deck
last
----- cross-wire -----
2
equation 1 wire information
run number = inc
iwtype nohr phi xk l d rs rl tcr ical
2 6 -47.9 .00 1.00 51.0 50. .0 .24 2
ohr # wire # rw rref tref
1 1    12.768 6.728 21.5
2 1    12.230 6.728 21.5
3 1    11.724 6.728 21.5
4 1    10.724 6.728 21.5
5 1    10.220 6.728 21.5
6 1    9.301 6.728 21.5
equation 2 wire information
run number = inc
iwtype nohr phi xk l d rs rl tcr ical
2 6 42.1 .00 1.00 51.0 50. .0 .24 2
ohr # wire # rw rref tref
1 2    12.811 6.780 21.5
2 2    12.297 6.780 21.5
3 2    11.811 6.780 21.5
4 2    10.810 6.780 21.5
5 2    10.302 6.780 21.5
6 2    9.280 6.780 21.5
```

UV#1 Input Deck for Heated Injection Case

14 September 1995

```
input deck
last
----- cross-wire -----
 2
equation 1 wire information
run number = in6
iwtype nohr phi  xk 1  d  rs  rl  tcr  ical
 2  5 -47.9 .00 1.00 51.0 50. .0 .24  2
ohr # wire #  rw  rref  tref
 1  1    12.768 6.728 21.5
 2  1    12.230 6.728 21.5
 3  1    11.724 6.728 21.5
 4  1    10.724 6.728 21.5
 5  1    9.301 6.728 21.5
equation 2 wire information
run number = in6
iwtype nohr phi  xk 1  d  rs  rl  tcr  ical
 2  5  42.1 .00 1.00 51.0 50. .0 .24  2
ohr # wire #  rw  rref  tref
 1  2    12.811 6.780 21.5
 2  2    12.297 6.780 21.5
 3  2    11.811 6.780 21.5
 4  2    10.810 6.780 21.5
 5  2    9.280 6.780 21.5
```

UW Input Deck for Heated Injection Case

6 September 1995

```
input deck
heat
----- cross-wire -----
2
equation 1 wire information
run number = in4
iwtype nohr phi xk 1 d rs rl tcr ical
2 5 -45.0 .00 1.00 51.0 50. .0 .24 2
ohr # wire # rw rref tref
1 1    11.692 5.968 21.5
2 1    10.709 5.968 21.5
3 1    10.188 5.968 21.5
4 1    9.800 5.968 21.5
5 1    9.278 5.968 21.5
equation 2 wire information
run number = in4
iwtype nohr phi xk 1 d rs rl tcr ical
2 5 45.0 .00 1.00 51.0 50. .0 .24 2
ohr # wire # rw rref tref
1 2    13.310 6.827 21.5
2 2    12.273 6.827 21.5
3 2    11.792 6.827 21.5
4 2    11.277 6.827 21.5
5 2    10.276 6.827 21.5
```

Appendix E

Cold Injection Tabulated Data

UV#1 Component Data
Cold Injection Case

Figure y(cm)	(5.11a) (rhou)rms	(5.11a) (rhov)rms	(5.14b) Cxy	(5.9b) thetamf	(5.15a) Rmxtt	(5.15a) Rmytt	(5.11a) Ttrms		5.8a	5.7b
	Pt1	Tt	Rex							
-2.1463	0.0387	0.0287	0.000377	0.0437	0.000245	0.0000643	0.0137	29.7	290	341
-2.12852	0.0362	0.0289	0.000332	0.0283	0.000104	0.0000119	0.00889	29.7	290	341
-2.09804	0.0358	0.0291	0.000305	-0.0061	0.0000438	-0.0000246	0.00722	29.6	290	341
-2.06502	0.0364	0.0291	0.000296	-0.0592	0.0000347	-0.0000223	0.00588	29.6	291	342
-2.02692	0.0355	0.0293	0.000299	-0.138	2.38E-06	1.72E-06	0.00639	29.6	291	341
-1.98882	0.0353	0.0292	0.000289	-0.249	0.0000156	0.0000275	0.00743	29.6	290	340
-1.94818	0.0332	0.0296	0.000302	-0.348	-0.0000352	0.0000517	0.00768	29.6	291	338
-1.90754	0.033	0.0292	0.000273	-0.43	-0.0000434	6.13E-06	0.00614	29.6	290	338
-1.86944	0.0343	0.0287	0.000272	-0.494	0.0000314	0.000031	0.00766	29.6	291	337
-1.8288	0.0355	0.0284	0.000302	-0.577	0.000104	0.0000579	0.00936	29.6	291	336
-1.78816	0.0328	0.0287	0.000291	-0.659	6.03E-06	0.0000255	0.00679	29.6	290	334
-1.74752	0.0339	0.0286	0.000321	-0.746	0.0000695	0.0000556	0.00899	29.6	291	333
-1.70688	0.0366	0.0287	0.000367	-0.841	0.000213	0.000117	0.0128	29.6	291	332
-1.66624	0.0371	0.0287	0.00036	-0.943	0.000196	0.0000777	0.0124	29.6	291	330
-1.6256	0.0404	0.029	0.00043	-1.01	0.000362	0.000138	0.0163	29.6	291	328
-1.58496	0.0437	0.0294	0.00051	-1.03	0.000493	0.000193	0.0192	29.6	291	326
-1.54432	0.0448	0.0307	0.000623	-1.02	0.000343	0.00024	0.0181	29.6	292	324
-1.50368	0.0459	0.032	0.000697	-1	0.000115	0.000184	0.0138	29.6	292	322
-1.46304	0.0544	0.0342	0.000931	-0.963	0.000359	0.000309	0.0188	29.6	292	319
-1.42224	0.0711	0.0376	0.00131	-0.913	0.00144	0.000627	0.03	29.6	292	314
-1.3843	0.0759	0.0409	0.00154	-0.849	0.00123	0.000565	0.0312	29.6	294	310
-1.34366	0.0817	0.0442	0.00193	-0.757	0.000916	0.000715	0.028	29.6	294	305
-1.30302	0.0931	0.0482	0.00242	-0.646	0.00137	0.000848	0.0318	29.6	293	298
-1.26238	0.1	0.0525	0.00288	-0.511	0.00134	0.000874	0.0318	29.6	296	292
-1.22174	0.113	0.0563	0.00371	-0.416	0.00254	0.00148	0.0391	29.5	295	284
-1.1811	0.118	0.06	0.00431	-0.337	0.00242	0.00175	0.0375	29.6	296	276
-1.14046	0.122	0.063	0.00469	-0.329	0.00249	0.00171	0.0369	29.6	296	269
-1.09982	0.125	0.0657	0.00509	-0.306	0.00284	0.00191	0.0392	29.5	296	261
-1.05918	0.124	0.0687	0.00536	-0.362	0.0026	0.00182	0.0366	29.5	295	254
-1.01854	0.127	0.0706	0.0057	-0.493	0.00323	0.00211	0.0409	29.6	295	247
-0.9779	0.127	0.072	0.00588	-0.753	0.00367	0.00241	0.0446	29.5	294	242
-0.93726	0.126	0.0729	0.0056	-1.16	0.00369	0.00234	0.0452	29.6	293	238
-0.89662	0.126	0.0732	0.00536	-1.63	0.00352	0.00228	0.0446	29.5	293	234
-0.85598	0.124	0.0738	0.00458	-2.08	0.00284	0.00163	0.0409	29.6	293	230
-0.81534	0.133	0.0744	0.00392	-2.39	0.00405	0.00153	0.0487	29.5	291	225
-0.77747	0.142	0.0759	0.00402	-2.43	0.00473	0.00224	0.0513	29.6	291	218
-0.73406	0.14	0.0779	0.00353	-2.21	0.0036	0.00154	0.0441	29.5	291	210
-0.69342	0.141	0.0791	0.00393	-1.76	0.00359	0.00184	0.0437	29.5	289	201
-0.65278	0.139	0.0802	0.00427	-1.16	0.00347	0.00161	0.0436	29.5	288	192
-0.61214	0.136	0.0806	0.00414	-0.492	0.00367	0.000662	0.0464	29.5	289	183
-0.5715	0.131	0.0821	0.00472	0.13	0.00355	0.000645	0.0468	29.5	287	175
-0.53086	0.125	0.0834	0.00514	0.601	0.00371	0.000839	0.0494	29.5	287	168
-0.49022	0.12	0.0852	0.00502	0.857	0.00389	0.00073	0.052	29.5	286	162

Table E.1: Cold Data.

UV#1 Component Mean Flow Data
Cold Injection Case

Figure y(cm)	(5.10a) rhoubar	(5.10a) rhovbar	(5.9a) ubar	(5.9a) vbar	(5.8b) rhobar	(5.10b) rhobub
-2.12852	120	0.0594	598	0.265	0.209	125
-2.09804	120	-0.0128	601	-0.0948	0.207	124
-2.06502	121	-0.125	600	-0.65	0.207	124
-2.02692	121	-0.29	599	-1.47	0.207	124
-1.98882	120	-0.521	598	-2.62	0.206	123
-1.94818	119	-0.726	599	-3.66	0.205	123
-1.90754	119	-0.894	598	-4.51	0.205	123
-1.86944	119	-1.03	601	-5.2	0.203	122
-1.8288	119	-1.2	597	-6.04	0.205	122
-1.78816	118	-1.35	599	-6.92	0.204	122
-1.74752	118	-1.53	599	-7.83	0.203	122
-1.70688	117	-1.72	600	-8.83	0.204	122
-1.66624	117	-1.92	601	-9.91	0.205	123
-1.6256	116	-2.04	602	-10.6	0.204	123
-1.58496	115	-2.07	601	-10.8	0.204	122
-1.54432	115	-2.04	600	-10.7	0.203	122
-1.50368	114	-1.99	601	-10.5	0.204	122
-1.46304	113	-1.9	600	-10.2	0.204	122
-1.42224	111	-1.77	600	-9.63	0.204	122
-1.3843	110	-1.64	603	-9.03	0.201	121
-1.34366	109	-1.44	603	-8.1	0.2	120
-1.30302	106	-1.19	602	-6.95	0.2	120
-1.26238	105	-0.933	604	-5.59	0.196	118
-1.22174	101	-0.737	601	-4.59	0.194	116
-1.1811	98.9	-0.582	603	-3.8	0.192	115
-1.14046	96.4	-0.553	597	-3.71	0.188	112
-1.09982	93.5	-0.499	594	-3.46	0.185	110
-1.05918	90.8	-0.573	591	-4.04	0.181	107
-1.01854	88.3	-0.759	586	-5.34	0.178	104
-0.9779	86.2	-1.13	580	-7.91	0.173	100
-0.93726	84.6	-1.71	576	-11.9	0.17	98
-0.89662	83.2	-2.37	569	-16.4	0.165	94
-0.85598	81.7	-2.97	565	-20.7	0.162	91.6
-0.81534	79.5	-3.32	556	-23.4	0.159	88.3
-0.77747	77.1	-3.27	550	-23.5	0.155	85.3
-0.73406	74.2	-2.86	543	-21.1	0.152	82.6
-0.69342	70.7	-2.17	535	-16.6	0.15	80.1
-0.65278	67.3	-1.36	528	-10.8	0.145	76.7
-0.61214	64.4	-0.553	522	-4.65	0.142	74.3
-0.5715	61.2	0.139	514	0.985	0.141	72.3
-0.53086	58.8	0.616	506	5.14	0.139	70.1
-0.49022	56.5	0.845	499	7.29	0.138	68.8

UV#1 Component Separated Turbulence Data
Cold Injection Case

Figure	(5.12a)	(5.12a)	(5.12a)	(5.18a)	(5.18a)	(5.17a)
Y(cm)	(rho)rms	Urms	Vrms	rhopup	rhopvp	UpVp
-2.12852	0.0263	0.0117	0.0289	0.000242	0.000245	8.68E-05
-2.09804	0.027	0.0102	0.0291	0.000225	0.000248	5.66E-05
-2.06502	0.0274	0.00991	0.0291	0.000238	0.00024	5.66E-05
-2.02692	0.0273	0.00939	0.0293	0.000214	0.000227	7.27E-05
-1.98882	0.027	0.00985	0.0292	0.000211	0.000205	8.66E-05
-1.94818	0.0264	0.00867	0.0296	0.000166	0.0002	0.000105
-1.90754	0.0262	0.00801	0.0292	0.00017	0.000206	6.97E-05
-1.86944	0.026	0.00988	0.0287	0.0002	0.000192	8.44E-05
-1.8288	0.0257	0.0118	0.0284	0.000231	0.000197	0.00011
-1.78816	0.0252	0.00896	0.0287	0.000179	0.00021	8.59E-05
-1.74752	0.0251	0.0108	0.0286	0.0002	0.000215	0.000113
-1.70688	0.0253	0.0142	0.0287	0.000249	0.000215	0.000163
-1.66624	0.026	0.0139	0.0287	0.000254	0.000235	0.000137
-1.6256	0.0267	0.0172	0.0291	0.00031	0.000256	0.000191
-1.58496	0.0281	0.0198	0.0295	0.000365	0.000285	0.000247
-1.54432	0.0311	0.0185	0.0308	0.00035	0.00034	0.000303
-1.50368	0.0345	0.015	0.0321	0.000346	0.00043	0.000284
-1.46304	0.0389	0.0203	0.0343	0.000519	0.000536	0.000421
-1.42224	0.0437	0.0327	0.0377	0.00104	0.000643	0.00072
-1.3843	0.0505	0.0326	0.041	0.00107	0.000859	0.000733
-1.34366	0.0576	0.0308	0.0443	0.00121	0.00106	0.000914
-1.30302	0.0642	0.0358	0.0483	0.00163	0.00136	0.00112
-1.26238	0.0701	0.0368	0.0526	0.00186	0.00168	0.00124
-1.22174	0.0743	0.0459	0.0564	0.00257	0.00193	0.00184
-1.1811	0.0792	0.0456	0.0601	0.00279	0.00221	0.00214
-1.14046	0.0811	0.0473	0.0631	0.00304	0.00248	0.00225
-1.09982	0.0814	0.0502	0.0658	0.00323	0.00263	0.00251
-1.05918	0.081	0.049	0.0688	0.00321	0.00287	0.00254
-1.01854	0.0796	0.054	0.0708	0.00344	0.0029	0.00288
-0.97779	0.0769	0.0574	0.0723	0.00346	0.00282	0.00319
-0.93726	0.0753	0.0583	0.0733	0.0034	0.00268	0.00313
-0.89662	0.0748	0.0591	0.0738	0.0034	0.00253	0.00313
-0.85598	0.0756	0.0562	0.0745	0.00325	0.00239	0.00253
-0.81534	0.0762	0.0658	0.0751	0.00377	0.00203	0.00239
-0.77747	0.0792	0.0719	0.0766	0.00436	0.00164	0.00297
-0.73406	0.0804	0.0676	0.0785	0.00429	0.00166	0.00236
-0.69342	0.0796	0.0692	0.0796	0.00437	0.00162	0.00272
-0.65278	0.0773	0.0699	0.0806	0.00423	0.00185	0.00268
-0.61214	0.0731	0.0723	0.0808	0.00396	0.00226	0.00199
-0.57715	0.0689	0.0722	0.0821	0.0036	0.00251	0.00218
-0.53086	0.0627	0.0738	0.0832	0.00312	0.00251	0.0025
-0.49022	0.0574	0.0757	0.0849	0.00269	0.00242	0.00241

UV#1 Component Reynolds Separated Shear Data
Cold Injection Case

Figure	(5.20a)	(5.20a)	(5.20a)	(5.20a)
y(cm)	RHO _b (UbV _b)	Ub(RHO _p V _p)	V _b (RHO _p U _p)	ReyShear
-2.12852	-0.0000868	-0.000245	-1.07E-07	-0.00033
-2.09804	-0.0000566	-0.000248	3.55E-08	-0.00031
-2.06502	-0.0000566	-0.00024	2.58E-07	-0.0003
-2.02692	-0.0000727	-0.000227	5.26E-07	-0.0003
-1.98882	-0.0000866	-0.000205	9.24E-07	-0.00029
-1.94818	-0.000105	-0.0002	1.02E-06	-0.0003
-1.90754	-0.0000697	-0.000206	1.28E-06	-0.00028
-1.86944	-0.0000844	-0.000192	1.74E-06	-0.00027
-1.8288	-0.00011	-0.000197	2.33E-06	-0.00031
-1.78816	-0.0000859	-0.00021	2.07E-06	-0.00029
-1.74752	-0.000113	-0.000215	2.62E-06	-0.00033
-1.70688	-0.000163	-0.000215	3.67E-06	-0.00037
-1.66624	-0.000137	-0.000235	4.19E-06	-0.00037
-1.6256	-0.000191	-0.000256	5.49E-06	-0.00044
-1.58496	-0.000247	-0.000285	6.58E-06	-0.00053
-1.54432	-0.000303	-0.00034	6.26E-06	-0.00064
-1.50368	-0.000284	-0.00043	6.08E-06	-0.00071
-1.46304	-0.000421	-0.000536	8.77E-06	-0.00095
-1.4224	-0.00072	-0.000643	0.0000167	-0.00135
-1.3843	-0.000733	-0.000859	0.0000161	-0.00158
-1.34366	-0.000914	-0.00106	0.0000162	-0.00196
-1.30302	-0.00112	-0.00136	0.0000188	-0.00245
-1.26238	-0.00124	-0.00168	0.0000172	-0.00291
-1.22174	-0.00184	-0.00193	0.0000196	-0.00374
-1.1811	-0.00214	-0.00221	0.0000176	-0.00434
-1.14046	-0.00225	-0.00248	0.0000189	-0.00472
-1.09982	-0.00251	-0.00263	0.0000188	-0.00512
-1.05918	-0.00254	-0.00287	0.0000219	-0.00539
-1.01854	-0.00288	-0.0029	0.0000314	-0.00575
-0.9779	-0.00319	-0.00282	0.0000471	-0.00597
-0.93726	-0.00313	-0.00268	0.0000704	-0.00574
-0.89662	-0.00313	-0.00253	0.000098	-0.00556
-0.85598	-0.00253	-0.00239	0.000119	-0.00481
-0.81534	-0.00239	-0.00203	0.000159	-0.00427
-0.7747	-0.00297	-0.00164	0.000186	-0.00443
-0.73406	-0.00236	-0.00166	0.000166	-0.00386
-0.69342	-0.00272	-0.00162	0.000135	-0.0042
-0.65278	-0.00268	-0.00185	0.0000868	-0.00445
-0.61214	-0.00199	-0.00226	0.0000353	-0.00422
-0.5715	-0.00218	-0.00251	-0.0000069	-0.0047
-0.53086	-0.0025	-0.00251	-0.0000317	-0.00504
-0.49022	-0.00241	-0.00242	-0.0000394	-0.00487

UV#1 Component Compressible Shear Data
Cold Injection Case

Figure	(5.13a)	(5.13a)	(5.13a)
y(cm)	Term 1	term 2	shear
-2.12852	-0.00033	3.31E-07	-0.00033
-2.09804	-0.00031	-1.23E-07	-0.00031
-2.06502	-0.0003	-8.62E-07	-0.0003
-2.02692	-0.0003	-1.93E-06	-0.0003
-1.98882	-0.00029	-3.36E-06	-0.00029
-1.94818	-0.0003	-4.48E-06	-0.00031
-1.90754	-0.00027	-5.49E-06	-0.00028
-1.86944	-0.00027	-6.17E-06	-0.00028
-1.8288	-0.0003	-7.06E-06	-0.00031
-1.78816	-0.00029	-7.92E-06	-0.0003
-1.74752	-0.00032	-8.84E-06	-0.00033
-1.70688	-0.00037	-1.00E-05	-0.00038
-1.66624	-0.00036	-1.20E-05	-0.00037
-1.6256	-0.00043	-1.40E-05	-0.00044
-1.58496	-0.00051	-1.60E-05	-0.00053
-1.54432	-0.00062	-2.00E-05	-0.00064
-1.50368	-0.0007	-2.40E-05	-0.00072
-1.46304	-0.00093	-0.00003	-0.00096
-1.4224	-0.00131	-3.70E-05	-0.00135
-1.3843	-0.00154	-4.60E-05	-0.00159
-1.34366	-0.00193	-5.50E-05	-0.00198
-1.30302	-0.00242	-6.20E-05	-0.00248
-1.26238	-0.00288	-5.80E-05	-0.00294
-1.22174	-0.00371	-5.50E-05	-0.00377
-1.1811	-0.00431	-5.40E-05	-0.00436
-1.14046	-0.00469	-5.50E-05	-0.00475
-1.09982	-0.00509	-5.30E-05	-0.00514
-1.05918	-0.00536	-6.20E-05	-0.00542
-1.01854	-0.0057	-8.10E-05	-0.00578
-0.9779	-0.00588	-0.00011	-0.00599
-0.93726	-0.0056	-0.00016	-0.00576
-0.89662	-0.00536	-0.00021	-0.00557
-0.85598	-0.00458	-0.00026	-0.00484
-0.81534	-0.00392	-0.0003	-0.00422
-0.7747	-0.00402	-0.00033	-0.00435
-0.73406	-0.00353	-0.00031	-0.00384
-0.69342	-0.00393	-0.00025	-0.00418
-0.65278	-0.00427	-0.00016	-0.00443
-0.61214	-0.00414	-6.30E-05	-0.0042
-0.5715	-0.00472	1.27E-05	-0.00471
-0.53086	-0.00514	5.68E-05	-0.00508
-0.49022	-0.00502	7.13E-05	-0.00495

UV#1 Component Favre Data
Cold Injection Case

Figure	5.22a	5.22a	5.21 b
y(cm)	ubar	vbar	FavShear
-2.12852	-0.00024	-0.00025	-8.7E-05
-2.09804	-0.00023	-0.00025	-5.7E-05
-2.06502	-0.00024	-0.00024	-5.7E-05
-2.02692	-0.00021	-0.00023	-7.3E-05
-1.98882	-0.00021	-0.00021	-8.7E-05
-1.94818	-0.00017	-0.0002	-0.00011
-1.90754	-0.00017	-0.00021	-7E-05
-1.86944	-0.0002	-0.00019	-8.4E-05
-1.8288	-0.00023	-0.0002	-0.00011
-1.78816	-0.00018	-0.00021	-8.6E-05
-1.74752	-0.0002	-0.00022	-0.00011
-1.70688	-0.00025	-0.00022	-0.00016
-1.66624	-0.00025	-0.00024	-0.00014
-1.6256	-0.00031	-0.00026	-0.00019
-1.58496	-0.00037	-0.00029	-0.00025
-1.54432	-0.00035	-0.00034	-0.0003
-1.50368	-0.00035	-0.00043	-0.00028
-1.46304	-0.00052	-0.00054	-0.00042
-1.4224	-0.00104	-0.00064	-0.00072
-1.3843	-0.00107	-0.00086	-0.00073
-1.34366	-0.00121	-0.00106	-0.00091
-1.30302	-0.00163	-0.00136	-0.00112
-1.26238	-0.00186	-0.00168	-0.00124
-1.22174	-0.00257	-0.00193	-0.00184
-1.1811	-0.00279	-0.00221	-0.00214
-1.14046	-0.00304	-0.00248	-0.00225
-1.09982	-0.00323	-0.00263	-0.00251
-1.05918	-0.00321	-0.00287	-0.00254
-1.01854	-0.00344	-0.0029	-0.00288
-0.9779	-0.00346	-0.00282	-0.00319
-0.93726	-0.0034	-0.00268	-0.00313
-0.89662	-0.0034	-0.00253	-0.00313
-0.85598	-0.00325	-0.00239	-0.00253
-0.81534	-0.00377	-0.00203	-0.00239
-0.7747	-0.00436	-0.00164	-0.00297
-0.73406	-0.00429	-0.00166	-0.00236
-0.69342	-0.00437	-0.00162	-0.00272
-0.65278	-0.00423	-0.00185	-0.00268
-0.61214	-0.00396	-0.00226	-0.00199
-0.5715	-0.0036	-0.00251	-0.00218
-0.53086	-0.00312	-0.00251	-0.0025
-0.49022	-0.00269	-0.00242	-0.00241

UV#1 Component Turbulent Heat Flux Data
Cold Injection Case

Figure	(5.16a)	(5.16a)
y(cm)	qxt	qyt
-2.12852	0.000346	0.000254
-2.09804	0.000269	0.0002
-2.06502	0.000273	0.000216
-2.02692	2.16E-04	2.16E-04
-1.98882	0.000227	0.000239
-1.94818	0.000131	0.000218
-1.90754	0.000127	1.76E-04
-1.86944	0.000231	0.000231
-1.8288	0.000335	0.000289
-1.78816	1.85E-04	0.000205
-1.74752	0.00027	0.000256
-1.70688	0.000462	0.000366
-1.66624	0.00045	0.000332
-1.6256	0.000672	0.000448
-1.58496	0.000858	0.000558
-1.54432	0.000693	0.00059
-1.50368	0.000461	0.00053
-1.46304	0.000878	0.000828
-1.4224	0.00248	0.001667
-1.3843	0.0023	0.001635
-1.34366	0.002126	0.001925
-1.30302	0.003	0.002478
-1.26238	0.0032	0.002734
-1.22174	0.00511	0.00405
-1.1811	0.00521	0.00454
-1.14046	0.00553	0.00475
-1.09982	0.00607	0.00514
-1.05918	0.00581	0.00503
-1.01854	0.00667	0.00555
-0.9779	0.00713	0.00587
-0.93726	0.00709	0.00574
-0.89662	0.00692	0.00568
-0.85598	0.00609	0.00488
-0.81534	0.00782	0.0053
-0.7747	9.09E-03	0.0066
-0.73406	0.00789	0.00583
-0.69342	0.00796	0.00621
-0.65278	0.0077	0.00584
-0.61214	0.00763	0.004622
-0.5715	0.00715	0.004245
-0.53086	0.00683	0.003959
-0.49022	0.00658	0.003529

Appendix F

Hot Injection Tabulated Data

UV and UW Component

UV#1 Component Data
Hot Injection Case

Figure	(5.11b)	(5.11b)	(5.14b)	(5.9b)	(5.15b)	(5.15b)	(5.11b)		(5.8a)	(5.7b)
y(cm)	(rho _u)rms	(rho _v)rms	C _{xy}	theta _{mf}	R _{mxtt}	R _{mytt}	T _{trms}	Pt1	T _t	R _{ex}
-2.14884	0.0421	0.0287	0.000331	-0.227	0.000557	4.26E-05	0.0203	29.1	289	342
-2.13106	0.0407	0.0287	0.000315	-0.24	0.000416	2.48E-06	0.0178	29.1	289	342
-2.10312	0.0409	0.0285	0.000356	-0.239	0.000429	4.57E-05	0.0179	29.1	289	343
-2.06756	0.0417	0.0281	0.000381	-0.278	0.000487	9.53E-05	0.0187	29.1	289	342
-2.032	0.0412	0.0278	0.000328	-0.333	0.000442	2.78E-05	0.0179	29.1	290	342
-1.99136	0.0416	0.0278	0.000318	-0.43	0.000499	3.72E-05	0.0189	29.1	290	341
-1.95326	0.0417	0.0278	0.000301	-0.544	0.000553	4.32E-05	0.0201	29.1	290	340
-1.91262	0.0408	0.0275	0.000278	-0.656	0.000512	4.26E-05	0.0196	29.1	290	340
-1.87198	0.041	0.0274	0.00033	-0.73	0.000543	0.000122	0.0199	29.2	290	339
-1.83134	0.0387	0.0276	0.000271	-0.843	0.000419	1.26E-05	0.0182	29.2	290	338
-1.79324	0.0378	0.0274	0.000319	-0.958	0.00039	0.00008	0.0177	29.2	290	337
-1.7526	0.0393	0.0276	0.000321	-1.08	0.000464	6.36E-05	0.0187	29.2	290	336
-1.71196	0.0407	0.0276	0.000348	-1.22	0.000552	0.000103	0.0204	29.2	290	334
-1.67132	0.0396	0.0276	0.000311	-1.38	0.000482	0.000044	0.0194	29.2	290	332
-1.63068	0.0388	0.0277	0.00029	-1.46	0.000391	-1.37E-06	0.0183	29.2	290	330
-1.59004	0.037	0.0281	0.000346	-1.49	0.000173	4.56E-05	0.0148	29.2	291	328
-1.5494	0.0446	0.0291	0.000409	-1.48	0.000518	0.000099	0.0211	29.2	291	326
-1.50876	0.0479	0.0306	0.000351	-1.45	0.000608	-9.30E-05	0.0264	29.2	292	324
-1.46812	0.0598	0.0323	0.000581	-1.37	0.0011	9.07E-05	0.0315	29.2	291	321
-1.42748	0.0629	0.0351	0.00079	-1.32	0.00041	0.000127	0.0245	29.2	292	317
-1.38684	0.0699	0.0383	0.0011	-1.26	0.000278	0.000295	0.0281	29.2	294	314
-1.3462	0.0774	0.0418	0.00143	-1.19	-0.00025	0.00027	0.0236	29.2	294	308
-1.30556	0.0839	0.0456	0.00174	-1.06	-0.00074	0.000205	0.0214	29.2	296	301
-1.26492	0.0966	0.0492	0.0022	-0.843	-0.00037	0.000254	0.0267	29.2	298	294
-1.22428	0.112	0.0534	0.00294	-0.648	0.000674	0.000485	0.0348	29.2	300	286
-1.18618	0.128	0.0569	0.00375	-0.492	0.00241	0.000972	0.0447	29.2	299	277
-1.14554	0.13	0.059	0.00387	-0.425	0.00182	0.000705	0.042	29.2	300	268
-1.1049	0.139	0.0619	0.00445	-0.326	0.0027	0.00095	0.0459	29.2	302	259
-1.06426	0.146	0.0646	0.0049	-0.233	0.00361	0.00102	0.0496	29.2	302	250
-1.02362	0.148	0.0668	0.00533	-0.156	0.00378	0.0012	0.0505	29.2	303	242
-0.98298	0.154	0.0694	0.00625	-0.0722	0.00522	0.00195	0.0563	29.2	303	234
-0.94234	0.152	0.0718	0.00642	-0.0446	0.00488	0.00184	0.0554	29.2	304	226
-0.9017	0.152	0.073	0.00653	-0.021	0.00465	0.00166	0.0541	29.2	304	218
-0.86106	0.156	0.075	0.00718	-0.0084	0.00546	0.00218	0.0572	29.2	305	212
-0.82042	0.159	0.0762	0.00766	-0.012	0.00612	0.00265	0.0594	29.2	305	206
-0.77978	0.153	0.0767	0.00714	0.00561	0.00478	0.00205	0.0536	29.2	305	200
-0.73914	0.148	0.0764	0.00647	-0.0125	0.00438	0.0015	0.0532	29.2	306	194
-0.6985	0.147	0.0771	0.00644	0.00604	0.00421	0.00141	0.0518	29.2	306	187
-0.65786	0.144	0.0782	0.00628	0.0825	0.00383	0.00129	0.0502	29.2	306	182
-0.61722	0.145	0.079	0.00631	0.207	0.0044	0.00148	0.0529	29.2	307	176
-0.57658	0.144	0.0805	0.00648	0.316	0.00493	0.0016	0.0552	29.2	307	171
-0.53594	0.137	0.0808	0.00566	0.416	0.00415	0.000703	0.0526	29.2	307	166
-0.4953	0.132	0.0819	0.00533	0.465	0.00393	0.000396	0.0523	29.2	307	162

Table F.1: Hot Data.

UV#1 Component Mean Flow Data
Hot Injection Case

Figure y(cm)	(5.10a) rhoubar	(5.10a) rhovbar	(5.9a) ubar	(5.9a) vbar	(5.8b) rhobar	(5.10b) rhobub
-2.13106	120	-0.504	597	-2.53	0.209	125
-2.10312	121	-0.503	597	-2.52	0.209	125
-2.06756	120	-0.584	599	-2.93	0.209	125
-2.032	121	-0.701	601	-3.52	0.207	124
-1.99136	120	-0.902	599	-4.53	0.207	124
-1.95326	120	-1.14	598	-5.7	0.207	124
-1.91262	120	-1.37	600	-6.9	0.206	124
-1.87198	120	-1.52	599	-7.65	0.207	124
-1.83134	119	-1.75	598	-8.82	0.206	123
-1.79324	119	-1.99	601	-10.1	0.205	123
-1.7526	118	-2.23	601	-11.4	0.205	123
-1.71196	118	-2.51	601	-12.8	0.203	122
-1.67132	117	-2.82	601	-14.5	0.204	122
-1.63068	116	-2.97	602	-15.4	0.202	122
-1.59004	116	-3.02	604	-15.7	0.201	121
-1.5494	115	-2.98	606	-15.7	0.198	120
-1.50876	115	-2.91	607	-15.4	0.196	119
-1.46812	113	-2.71	606	-14.5	0.197	119
-1.42748	112	-2.59	606	-14	0.195	118
-1.38684	112	-2.46	607	-13.4	0.191	116
-1.3462	110	-2.28	607	-12.7	0.189	115
-1.30556	108	-1.99	604	-11.3	0.185	112
-1.26492	106	-1.56	607	-9.1	0.182	110
-1.22428	104	-1.17	606	-7.07	0.177	107
-1.18618	100	-0.859	604	-5.42	0.175	105
-1.14554	97	-0.72	599	-4.7	0.17	102
-1.1049	94.2	-0.536	595	-3.65	0.166	98.6
-1.06426	91	-0.37	588	-2.67	0.161	95
-1.02362	88.3	-0.24	583	-1.87	0.157	91.2
-0.98298	85.3	-0.108	576	-1	0.153	88.3
-0.94234	82.6	-0.0643	567	-0.714	0.149	84.6
-0.9017	79.7	-0.0292	565	-0.491	0.148	83.6
-0.86106	77.7	-0.0114	557	-0.353	0.144	80.2
-0.82042	75.5	-0.0158	548	-0.37	0.142	77.9
-0.77978	73.3	0.00718	539	-0.189	0.14	75.4
-0.73914	71.3	-0.0156	533	-0.343	0.139	74
-0.6985	68.7	0.00724	522	-0.159	0.137	71.8
-0.65786	66.9	0.0963	507	0.537	0.137	69.5
-0.61722	64.8	0.234	493	1.61	0.139	68.6
-0.57658	63	0.347	487	2.53	0.137	66.7
-0.53594	61.2	0.444	472	3.27	0.138	64.9
-0.4953	59.7	0.484	462	3.6	0.137	63.1

Table F.2: Hot Data.

UV#1 Component Separated Turbulence Data
Hot Injection Case

Figure	(5.12b)	(5.12b)	(5.12b)	(5.18b)	(5.18b)	(5.17b)
y(cm)	(rho)rms	Urms	Vrms	rhopup	rhopvp	UpVp
-2.13106	0.0262	0.0185	0.0287	0.000314	0.000241	7.85E-05
-2.10312	0.0262	0.0186	0.0285	0.00032	0.000246	0.000115
-2.06756	0.0262	0.0193	0.0281	0.000339	0.000236	0.000151
-2.032	0.0264	0.0186	0.0278	0.000328	0.000238	9.63E-05
-1.99136	0.0259	0.0195	0.0278	0.000339	0.000226	0.000101
-1.95326	0.0253	0.0205	0.0278	0.00034	0.00021	0.000103
-1.91262	0.0252	0.0197	0.0275	0.00032	0.000195	9.62E-05
-1.87198	0.0248	0.0202	0.0274	0.000329	0.000186	0.000159
-1.83134	0.0244	0.0184	0.0276	0.000281	0.000208	7.78E-05
-1.79324	0.0242	0.0177	0.0274	0.000265	0.000206	0.00013
-1.7526	0.0245	0.0188	0.0277	0.000296	0.00022	0.000121
-1.71196	0.0246	0.0203	0.0277	0.00032	0.00022	0.000154
-1.67132	0.0246	0.0192	0.0277	0.000296	0.000229	0.000109
-1.63068	0.0254	0.0179	0.0278	0.00027	0.000241	7.49E-05
-1.59004	0.027	0.0144	0.0282	0.000218	0.000252	0.000114
-1.5494	0.0293	0.0205	0.0292	0.000356	0.000278	0.000165
-1.50876	0.0325	0.0235	0.0307	0.000344	0.000357	3.67E-05
-1.46812	0.0382	0.0295	0.0324	0.000623	0.000435	0.00021
-1.42748	0.0467	0.0235	0.0352	0.00061	0.000565	0.000273
-1.38684	0.0541	0.0253	0.0384	0.000662	0.000703	0.00045
-1.3462	0.0632	0.0215	0.042	0.000771	0.000972	0.000506
-1.30556	0.0703	0.019	0.0458	0.000869	0.00123	0.000551
-1.26492	0.0777	0.0263	0.0494	0.0013	0.00156	0.000691
-1.22428	0.0838	0.0375	0.0536	0.00205	0.00198	0.00103
-1.18618	0.0886	0.0499	0.057	0.00302	0.00228	0.00154
-1.14554	0.0917	0.0486	0.0591	0.00307	0.00249	0.00144
-1.1049	0.0939	0.0555	0.062	0.00371	0.00272	0.00179
-1.06426	0.0943	0.0621	0.0647	0.00428	0.00294	0.00201
-1.02362	0.0938	0.0648	0.0669	0.00445	0.00307	0.0023
-0.98298	0.0913	0.0734	0.0694	0.00499	0.00316	0.00311
-0.94234	0.0888	0.0744	0.0718	0.00484	0.00323	0.0032
-0.9017	0.0892	0.0739	0.073	0.00485	0.00339	0.00314
-0.86106	0.0871	0.0801	0.075	0.00517	0.00339	0.0038
-0.82042	0.0845	0.0857	0.0762	0.0054	0.00327	0.0044
-0.77978	0.0827	0.0813	0.0767	0.00498	0.0032	0.00393
-0.73914	0.0794	0.0805	0.0764	0.00456	0.00307	0.0034
-0.6985	0.0766	0.0821	0.0771	0.0045	0.00298	0.00346
-0.65786	0.0727	0.0834	0.0782	0.00425	0.00278	0.00348
-0.61722	0.0678	0.0903	0.0789	0.00414	0.00247	0.00377
-0.57658	0.0634	0.0942	0.0803	0.00392	0.00239	0.00399
-0.53594	0.0594	0.0922	0.0806	0.00336	0.00242	0.00312
-0.4953	0.0557	0.0921	0.0816	0.00292	0.00238	0.00282

UV#1 Component Separated Reynolds Shear Data
Hot Injection Case

Figure	(5.20b)	(5.20b)	(5.20b)	(5.20b)
Y(cm)	RHO _b (UbV _b)	Ub(RHO _p V _p)	V _b (RHO _p U _p)	ReyShear
-2.13106	-7.90E-05	-0.00024	1.33E-06	-0.00032
-2.10312	-0.00012	-0.00025	1.35E-06	-0.00036
-2.06756	-0.00015	-0.00024	1.66E-06	-0.00039
-2.032	-9.60E-05	-0.00024	1.92E-06	-0.00033
-1.99136	-0.0001	-0.00023	2.56E-06	-0.00032
-1.95326	-0.0001	-0.00021	3.24E-06	-0.00031
-1.91262	-9.60E-05	-0.0002	3.68E-06	-0.00029
-1.87198	-0.00016	-0.00019	4.21E-06	-0.00034
-1.83134	-7.80E-05	-0.00021	4.15E-06	-0.00028
-1.79324	-0.00013	-0.00021	4.44E-06	-0.00033
-1.7526	-0.00012	-0.00022	5.59E-06	-0.00034
-1.71196	-0.00015	-0.00022	6.82E-06	-0.00037
-1.67132	-0.00011	-0.00023	7.15E-06	-0.00033
-1.63068	-7.50E-05	-0.00024	6.91E-06	-0.00031
-1.59004	-0.00011	-0.00025	5.68E-06	-0.00036
-1.5494	-0.00017	-0.00028	9.21E-06	-0.00043
-1.50876	-3.70E-05	-0.00036	8.73E-06	-0.00039
-1.46812	-0.00021	-0.00044	0.000015	-0.00063
-1.42748	-0.00027	-0.00057	1.41E-05	-0.00082
-1.38684	-0.00045	-0.0007	1.46E-05	-0.00114
-1.3462	-0.00051	-0.00097	1.62E-05	-0.00146
-1.30556	-0.00055	-0.00123	1.63E-05	-0.00177
-1.26492	-0.00069	-0.00156	1.95E-05	-0.00223
-1.22428	-0.00103	-0.00198	2.39E-05	-0.00298
-1.18618	-0.00154	-0.00228	2.71E-05	-0.0038
-1.14554	-0.00144	-0.00249	2.41E-05	-0.00391
-1.1049	-0.00179	-0.00272	2.28E-05	-0.00449
-1.06426	-0.00201	-0.00294	1.94E-05	-0.00493
-1.02362	-0.0023	-0.00307	1.43E-05	-0.00535
-0.98298	-0.00311	-0.00316	8.70E-06	-0.00626
-0.94234	-0.0032	-0.00323	6.10E-06	-0.00643
-0.9017	-0.00314	-0.00339	4.21E-06	-0.00653
-0.86106	-0.0038	-0.00339	3.28E-06	-0.00718
-0.82042	-0.0044	-0.00327	3.64E-06	-0.00766
-0.77978	-0.00393	-0.0032	1.74E-06	-0.00714
-0.73914	-0.0034	-0.00307	2.94E-06	-0.00647
-0.6985	-0.00346	-0.00298	1.37E-06	-0.00644
-0.65786	-0.00348	-0.00278	-4.50E-06	-0.00626
-0.61722	-0.00377	-0.00247	-1.40E-05	-0.00626
-0.57658	-0.00399	-0.00239	-2.00E-05	-0.0064
-0.53594	-0.00312	-0.00242	-2.30E-05	-0.00556
-0.4953	-0.00282	-0.00238	-2.30E-05	-0.00522

Table F.4: Hot Data.

UV#1 Component Compressible Shear Data
Hot Injection Case

Figure	(5.13b)	(5.13b)	(5.13b)
y(cm)	term 1	term 2	shear
-2.13106	-0.00032	-3.14E-06	-0.00032
-2.10312	-0.00036	-3.13E-06	-0.00036
-2.06756	-0.00038	-3.64E-06	-0.00039
-2.032	-0.00033	-4.34E-06	-0.00033
-1.99136	-0.00032	-5.4E-06	-0.00032
-1.95326	-0.0003	-6.51E-06	-0.00031
-1.91262	-0.00028	-7.76E-06	-0.00029
-1.87198	-0.00033	-8.44E-06	-0.00034
-1.83134	-0.00027	-9.41E-06	-0.00028
-1.79324	-0.00032	-1.1E-05	-0.00033
-1.7526	-0.00032	-1.2E-05	-0.00033
-1.71196	-0.00035	-1.4E-05	-0.00036
-1.67132	-0.00031	-1.6E-05	-0.00033
-1.63068	-0.00029	-1.8E-05	-0.00031
-1.59004	-0.00035	-2.1E-05	-0.00037
-1.5494	-0.00041	-2.4E-05	-0.00043
-1.50876	-0.00035	-2.9E-05	-0.00038
-1.46812	-0.00058	-3.9E-05	-0.00062
-1.42748	-0.00079	-5.6E-05	-0.00085
-1.38684	-0.0011	-7E-05	-0.00117
-1.3462	-0.00143	-9.2E-05	-0.00152
-1.30556	-0.00174	-1E-04	-0.00184
-1.26492	-0.0022	-9.8E-05	-0.0023
-1.22428	-0.00294	-8.8E-05	-0.00303
-1.18618	-0.00375	-7.8E-05	-0.00383
-1.14554	-0.00387	-7.3E-05	-0.00394
-1.1049	-0.00445	-5.9E-05	-0.00451
-1.06426	-0.0049	-4.4E-05	-0.00494
-1.02362	-0.00533	-3E-05	-0.00536
-0.98298	-0.00625	-1.6E-05	-0.00627
-0.94234	-0.00642	-1E-05	-0.00643
-0.9017	-0.00653	-7.61E-06	-0.00654
-0.86106	-0.00718	-5.12E-06	-0.00719
-0.82042	-0.00766	-5.13E-06	-0.00767
-0.77978	-0.00714	-2.53E-06	-0.00714
-0.73914	-0.00647	-4.37E-06	-0.00647
-0.6985	-0.00644	-1.95E-06	-0.00644
-0.65786	-0.00628	6.03E-06	-0.00627
-0.61722	-0.00631	1.68E-05	-0.00629
-0.57658	-0.00648	2.34E-05	-0.00646
-0.53594	-0.00566	2.75E-05	-0.00563
-0.4953	-0.00533	0.000027	-0.0053

Table F.5: Hot Data.

UV#1 Component Favre Data
Hot Injection Case

Figure	(5.22b)	(5.22b)	(5.21b)
y(cm)	ubar	vbar	FavShear
-2.13106	-0.00031	-0.00024	-7.90E-05
-2.10312	-0.00032	-0.00025	-0.00012
-2.06756	-0.00034	-0.00024	-0.00015
-2.032	-0.00033	-0.00024	-9.60E-05
-1.99136	-0.00034	-0.00023	-0.0001
-1.95326	-0.00034	-0.00021	-0.0001
-1.91262	-0.00032	-0.0002	-9.60E-05
-1.87198	-0.00033	-0.00019	-0.00016
-1.83134	-0.00028	-0.00021	-7.80E-05
-1.79324	-0.00027	-0.00021	-0.00013
-1.7526	-0.0003	-0.00022	-0.00012
-1.71196	-0.00032	-0.00022	-0.00015
-1.67132	-0.0003	-0.00023	-0.00011
-1.63068	-0.00027	-0.00024	-7.50E-05
-1.59004	-0.00022	-0.00025	-0.00011
-1.5494	-0.00036	-0.00028	-0.00017
-1.50876	-0.00034	-0.00036	-3.70E-05
-1.46812	-0.00062	-0.00044	-0.00021
-1.42748	-0.00061	-0.00057	-0.00027
-1.38684	-0.00066	-0.0007	-0.00045
-1.3462	-0.00077	-0.00097	-0.00051
-1.30556	-0.00087	-0.00123	-0.00055
-1.26492	-0.0013	-0.00156	-0.00069
-1.22428	-0.00205	-0.00198	-0.00103
-1.18618	-0.00302	-0.00228	-0.00154
-1.14554	-0.00307	-0.00249	-0.00144
-1.1049	-0.00371	-0.00272	-0.00179
-1.06426	-0.00428	-0.00294	-0.00201
-1.02362	-0.00445	-0.00307	-0.0023
-0.98298	-0.00499	-0.00316	-0.00311
-0.94234	-0.00484	-0.00323	-0.0032
-0.9017	-0.00485	-0.00339	-0.00314
-0.86106	-0.00517	-0.00339	-0.0038
-0.82042	-0.0054	-0.00327	-0.0044
-0.77978	-0.00498	-0.0032	-0.00393
-0.73914	-0.00456	-0.00307	-0.0034
-0.6985	-0.0045	-0.00298	-0.00346
-0.65786	-0.00425	-0.00278	-0.00348
-0.61722	-0.00414	-0.00247	-0.00377
-0.57658	-0.00392	-0.00239	-0.00399
-0.53594	-0.00336	-0.00242	-0.00312
-0.4953	-0.00292	-0.00238	-0.00282

UV#1 and UW Component Turbulent Heat Flux and TKE Data
Hot Injection Case

Figure	(5.16b)	(5.16b)		Figure	(5.16b)		Figure	(5.19a)	Figure	(5.19b)
y(cm)	qxt	qyt		y(cm)	qzt		y(cm)	tke-comp	y(cm)	tke-incom
-2.13106	0.00073	3.16E-04		-2.15138	0.000351		-2.13868	0.00167	-2.13106	1.01E-03
-2.10312	0.000749	0.000366		-2.12344	0.000221		-2.11074	0.00168	-2.10312	1.02E-03
-2.06756	0.000826	0.000434		-2.08788	0.000133		-2.07518	0.00171	-2.06756	1.03E-03
-2.032	0.00077	0.000356		-2.05232	0.000247		-2.03962	0.00167	-2.032	9.97E-04
-1.99136	0.000838	0.000376		-2.01168	2.43E-04		-1.99898	0.0017	-1.99136	1.02E-03
-1.95326	0.000893	0.000383		-1.97358	0.000297		-1.96088	0.0017	-1.95326	1.04E-03
-1.91262	0.000832	0.000363		-1.93294	2.73E-04		-1.92024	0.00165	-1.91262	1.01E-03
-1.87198	0.000872	0.000451		-1.8923	0.000338		-1.8796	0.00165	-1.87198	1.01E-03
-1.83134	0.0007	0.000294		-1.85166	0.000302		-1.83896	0.00157	-1.83134	9.88E-04
-1.79324	0.000655	0.000345		-1.80848	0.000214		-1.79832	0.00153	-1.79324	9.76E-04
-1.7526	0.00076	0.00036		-1.76784	-0.00014		-1.75768	0.00163	-1.7526	1.03E-03
-1.71196	0.000872	0.000423		-1.7272	-0.00038		-1.71704	0.00171	-1.71196	1.09E-03
-1.67132	0.000778	0.00034		-1.68402	-0.0004		-1.6764	0.00167	-1.67132	1.07E-03
-1.63068	0.000661	2.69E-04		-1.64338	-0.00033		-1.63576	0.00165	-1.63068	1.05E-03
-1.59004	0.000391	0.000264		-1.5621	-0.00062		-1.57988	0.00164	-1.5494	1.19E-03
-1.5494	0.000874	0.000455		-1.4986	-0.00115		-1.53162	0.00205	-1.50876	1.38E-03
-1.50876	0.000952	0.000251		-1.44526	-0.00201		-1.48844	0.00242	-1.42748	1.70E-03
-1.46812	0.001723	0.000714		-1.397	-0.0017		-1.44526	0.00316	-1.38684	1.90E-03
-1.42748	0.00102	0.000737		-1.35382	-0.00147		-1.40208	0.00355	-1.3462	2.05E-03
-1.38684	9.40E-04	0.000957		-1.31064	-0.00122		-1.36144	0.00437	-1.30556	2.39E-03
-1.3462	0.000521	0.001041		-1.26746	-0.00027		-1.3208	0.00516	-1.26492	2.83E-03
-1.30556	0.000129	0.001074		-1.22428	7.57E-04		-1.27762	0.00606	-1.22428	3.59E-03
-1.26492	0.000927	0.001554		-1.18364	0.001166		-1.23698	0.00769	-1.18618	4.60E-03
-1.22428	0.002724	0.002535		-1.143	0.001352		-1.19634	0.00976	-1.14554	4.89E-03
-1.18618	0.00543	0.003992		-1.09982	0.00107		-1.15824	0.0123	-1.1049	5.78E-03
-1.14554	0.00489	0.003775		-1.05918	0.00061		-1.1176	0.013	-1.06426	6.66E-03
-1.1049	0.00641	0.00466		-1.016	5.70E-04		-1.07442	0.0145	-1.02362	7.06E-03
-1.06426	0.00789	0.0053		-0.97536	-0.00033		-1.03378	0.0158	-0.98298	7.98E-03
-1.02362	0.00823	0.00565		-0.93472	-8.00E-05		-0.99314	0.0163	-0.94234	0.00831
-0.98298	0.01021	0.00694		-0.89408	-0.00003		-0.9525	0.0175	-0.9017	8.44E-03
-0.94234	0.00972	0.00668		-0.85344	-6.30E-04		-0.91186	0.0175	-0.86106	9.21E-03
-0.9017	9.50E-03	0.00651		-0.8128	-0.00052		-0.87122	0.0176	-0.82042	9.83E-03
-0.86106	0.01063	0.00735		-0.76962	-7.20E-04		-0.83058	0.0185	-0.77978	9.61E-03
-0.82042	0.01152	0.00805		-0.72898	-8.80E-04		-0.78994	0.0191	-0.73914	9.62E-03
-0.77978	0.00976	0.00703		-0.68834	-2.90E-04		-0.7493	0.0183	-0.6985	9.88E-03
-0.73914	0.00894	0.00606		-0.6477	-5.70E-04		-0.70866	0.0176	-0.65786	1.02E-02
-0.6985	0.00871	0.00591		-0.60452	-0.00158		-0.66802	0.0176	-0.61722	1.10E-02
-0.65786	0.00808	0.00554		-0.56388	-0.00083		-0.62738	0.0173	-0.57658	1.15E-02
-0.61722	0.00854	0.00562		-0.52324	-0.00178		-0.58674	0.0177	-0.53594	1.15E-02
-0.57658	0.00885	0.00552					-0.5461	0.0178	-0.4953	1.17E-02
-0.53594	0.00751	0.004063					-0.198	0.0169		

Table F.7: Hot Data.

UW Component Data
Hot Injection Case

Figure	(5.11b)	(5.11b)	(5.14b)	(5.9b)		(5.15b)	(5.11b)		(5.26b)	(5.7b)
y(cm)	(rho _u)rms	(rho _v)rms	Cxy	thetamf	Rmxtt	Rmztt	Ttrms	Pt1	Tt	Rex
-2.16916	0.0406	0.0294	0.000108	-1.38	0.00046	0.000129	0.0217	29.1	289	336
-2.15138	0.0407	0.0293	9.01E-05	-1.43	0.000556	0.000102	0.0246	29.1	290	336
-2.12344	0.0383	0.0296	4.64E-05	-1.51	0.000353	-8E-06	0.0199	29.1	291	336
-2.08788	0.0395	0.0299	-1.7E-05	-1.67	0.000443	-0.00011	0.0221	29.1	291	336
-2.05232	0.0408	0.0296	1.95E-05	-1.8	0.000527	-3.1E-06	0.0241	29.1	292	335
-2.01168	0.041	0.0298	3.15E-05	-1.84	0.000561	5.44E-06	0.0255	29.1	292	334
-1.97358	0.0434	0.0297	2.02E-05	-2.01	0.000738	2.26E-05	0.0283	29.1	292	332
-1.93294	0.0432	0.0297	1.17E-05	-2.18	0.000715	-5.47E-06	0.0276	29.1	292	331
-1.8923	0.0426	0.0294	1.42E-05	-2.33	0.000686	7.03E-05	0.0272	29.2	292	329
-1.85166	0.0413	0.0296	-3.7E-05	-2.53	0.000556	2.55E-05	0.0236	29.2	292	327
-1.80848	0.0423	0.0298	-9.3E-05	-2.66	0.000738	-5.5E-05	0.0278	29.2	293	326
-1.76784	0.043	0.0308	-0.00026	-2.7	0.000926	-0.00036	0.0327	29.2	292	323
-1.7272	0.0451	0.0316	-0.0004	-2.7	0.00122	-0.00059	0.038	29.2	291	322
-1.68402	0.0384	0.0317	-0.0003	-2.67	0.000642	-0.00054	0.0299	29.2	291	320
-1.64338	0.0327	0.0319	-0.00017	-2.61	0.000164	-0.00038	0.0229	29.2	291	318
-1.5621	0.0407	0.0334	-0.00021	-2.74	0.000406	-0.00057	0.0356	29.2	294	313
-1.4986	0.049	0.0356	-0.00046	-2.86	0.000762	-0.00106	0.045	29.2	296	310
-1.44526	0.05	0.0402	-0.00078	-3.07	0.000353	-0.00166	0.049	29.2	299	306
-1.397	0.0585	0.0413	-0.00083	-3.28	0.000222	-0.00145	0.0497	29.2	301	301
-1.35382	0.0713	0.0438	-0.00114	-3.53	0.000912	-0.00143	0.0573	29.2	305	296
-1.31064	0.0898	0.0488	-0.00215	-3.73	0.00196	-0.00177	0.0635	29.2	306	288
-1.26746	0.0946	0.0509	-0.00217	-3.99	0.00134	-0.00093	0.0603	29.2	309	282
-1.22428	0.105	0.0548	-0.00291	-4.28	0.00141	-0.00036	0.0592	29.2	310	274
-1.18364	0.118	0.0602	-0.00419	-4.48	0.00235	-0.00061	0.0631	29.2	309	266
-1.143	0.123	0.0642	-0.005	-4.54	0.00254	-0.0007	0.0639	29.2	310	259
-1.09982	0.133	0.07	-0.00652	-4.44	0.0037	-0.00169	0.0667	29.2	309	250
-1.05918	0.144	0.0749	-0.00795	-4.34	0.00586	-0.00293	0.0749	29.2	310	243
-1.016	0.141	0.0759	-0.00777	-4.12	0.00517	-0.00277	0.072	29.2	309	236
-0.97536	0.141	0.078	-0.00812	-3.87	0.00542	-0.00358	0.0744	29.2	308	229
-0.93472	0.143	0.079	-0.00814	-3.55	0.00595	-0.00336	0.0773	29.2	307	222
-0.89408	0.139	0.0798	-0.00773	-3.26	0.00507	-0.00309	0.0736	29.2	306	215
-0.85344	0.147	0.0817	-0.00837	-3.03	0.00707	-0.00403	0.0822	29.2	306	210
-0.8128	0.145	0.0824	-0.00809	-2.85	0.00668	-0.00373	0.0805	29.2	308	205
-0.76962	0.139	0.0835	-0.00775	-2.65	0.00573	-0.00359	0.0767	29.2	309	200
-0.72898	0.136	0.0845	-0.00727	-2.36	0.00538	-0.00333	0.0776	29.2	308	194
-0.68834	0.135	0.0853	-0.00686	-2.09	0.00498	-0.00271	0.0742	29.2	307	190
-0.6477	0.134	0.0864	-0.00666	-1.87	0.00507	-0.00269	0.0754	29.2	307	185
-0.60452	0.132	0.088	-0.00671	-1.63	0.00519	-0.00335	0.0758	29.2	308	181
-0.56388	0.131	0.0879	-0.0057	-1.23	0.00542	-0.00233	0.0775	29.2	307	176
-0.52324	0.131	0.09	-0.00603	-0.936	0.00531	-0.00321	0.0745	29.2	307	172
-0.4826	0.127	0.0911	-0.00562	-0.419	0.00521	-0.0036	0.0774	29.2	305	168

Table F.8: Hot Data.

UW Component Mean Flow Data
Hot Injection Case

Figure		(5.10a)		(5.9a)	(5.8b)	
y(cm)	rhoubar	rhowbar	ubar	wbar	rhobar	rhobub
-2.15138	118	-2.96	597	-14.9	0.209	125
-2.12344	119	-3.13	599	-15.8	0.208	125
-2.08788	119	-3.46	601	-17.5	0.207	124
-2.05232	119	-3.73	601	-18.9	0.206	124
-2.01168	118	-3.8	601	-19.3	0.206	124
-1.97358	118	-4.13	601	-21.1	0.205	123
-1.93294	117	-4.46	601	-22.9	0.205	123
-1.8923	117	-4.74	601	-24.4	0.206	124
-1.85166	116	-5.12	601	-26.5	0.205	123
-1.80848	116	-5.38	602	-28	0.204	123
-1.76784	115	-5.4	604	-28.5	0.203	123
-1.7272	114	-5.36	602	-28.4	0.203	122
-1.68402	113	-5.27	602	-28.1	0.203	122
-1.64338	112	-5.12	603	-27.5	0.202	122
-1.5621	112	-5.33	609	-29.1	0.197	120
-1.4986	111	-5.54	612	-30.6	0.194	119
-1.44526	110	-5.92	614	-33	0.191	117
-1.397	109	-6.25	615	-35.2	0.188	115
-1.35382	109	-6.69	619	-38.1	0.183	113
-1.31064	106	-6.89	615	-40	0.18	111
-1.26746	104	-7.27	618	-43	0.175	108
-1.22428	102	-7.6	616	-45.9	0.171	106
-1.18364	98.5	-7.7	613	-47.7	0.169	103
-1.143	96.1	-7.62	609	-47.9	0.164	99.9
-1.09982	92.6	-7.17	601	-46.3	0.161	96.9
-1.05918	90.2	-6.83	595	-44.8	0.157	93.4
-1.016	87.4	-6.28	588	-42	0.153	90.1
-0.97536	84.6	-5.71	579	-38.9	0.15	86.9
-0.93472	81.8	-5.07	569	-35	0.148	84.1
-0.89408	79	-4.5	567	-32	0.147	83.1
-0.85344	77.2	-4.08	558	-29.3	0.143	80
-0.8128	75.7	-3.77	549	-27.1	0.14	77
-0.76962	74.1	-3.42	546	-25.1	0.138	75.5
-0.72898	71.7	-2.95	534	-21.9	0.138	73.6
-0.68834	70	-2.55	518	-18.8	0.136	70.6
-0.6477	68.2	-2.22	504	-16.3	0.137	69.2
-0.60452	66.8	-1.9	491	-13.9	0.138	67.8
-0.56388	64.8	-1.39	485	-10.3	0.137	66.4
-0.52324	63.4	-1.04	467	-7.59	0.138	64.3
-0.4826	61.6	-0.45	456	-3.33	0.138	63

UW Component Separated Turbulence Data
Hot Injection Case

Figure ycm)	(rho)rms	Urms	Wrms	(5.12b) rhopup	(5.18b) rhopwp	(5.17b) UpWp
-2.15138	0.0258	0.0223	0.0293	0.000249	2.75E-05	9.74E-05
-2.12344	0.0258	0.0185	0.0296	0.000229	5.86E-05	1.52E-05
-2.08788	0.026	0.0201	0.0299	0.000239	7.57E-05	-5.8E-05
-2.05232	0.0263	0.0217	0.0296	0.00025	4.45E-05	1.75E-05
-2.01168	0.0264	0.0226	0.0298	0.000238	5.03E-05	2.73E-05
-1.97358	0.0265	0.0251	0.0297	0.000274	3.99E-05	4.09E-05
-1.93294	0.0265	0.0247	0.0297	0.000278	0.000053	2.26E-05
-1.8923	0.0263	0.0242	0.0294	0.000268	9.51E-06	7.08E-05
-1.85166	0.0261	0.0218	0.0296	0.000276	-4.2E-06	0.000028
-1.80848	0.0253	0.0248	0.0298	0.000268	1.17E-05	-2.7E-05
-1.76784	0.0249	0.0278	0.0307	0.000229	8.07E-05	-0.00025
-1.7272	0.0242	0.0319	0.0315	0.000214	0.000132	-0.00041
-1.68402	0.0245	0.0247	0.0316	0.000134	0.000145	-0.00037
-1.64338	0.0259	0.0175	0.0318	4.58E-05	0.000127	-0.00026
-1.5621	0.0328	0.0261	0.0333	-5.1E-05	0.00024	-0.00036
-1.4986	0.0384	0.0331	0.0355	-8.6E-05	0.000384	-0.0007
-1.44526	0.0454	0.0337	0.04	-0.00035	0.000507	-0.00114
-1.397	0.0524	0.0344	0.041	-0.00025	0.000369	-0.00102
-1.35382	0.0582	0.0421	0.0434	-3.9E-05	0.000189	-0.00103
-1.31064	0.0662	0.0508	0.0481	0.000553	-0.00025	-0.00144
-1.26746	0.073	0.0479	0.0502	0.000664	-0.00077	-0.00093
-1.22428	0.0797	0.0493	0.0538	0.00112	-0.0016	-0.00075
-1.18364	0.0853	0.0557	0.0589	0.00178	-0.00228	-0.00117
-1.143	0.0874	0.0583	0.0626	0.00205	-0.00274	-0.00144
-1.09982	0.0889	0.0652	0.0681	0.00276	-0.00308	-0.00246
-1.05918	0.0881	0.0768	0.0727	0.00354	-0.00311	-0.00361
-1.016	0.0869	0.0752	0.0738	0.00334	-0.00306	-0.00359
-0.97536	0.0849	0.0786	0.0759	0.00325	-0.0027	-0.00432
-0.93472	0.0829	0.0837	0.077	0.00328	-0.00273	-0.00431
-0.89408	0.0829	0.0795	0.0781	0.00306	-0.00272	-0.00409
-0.85344	0.0803	0.0914	0.0799	0.0034	-0.00234	-0.00497
-0.8128	0.0779	0.0924	0.0807	0.00321	-0.00222	-0.00488
-0.76962	0.076	0.0884	0.082	0.00287	-0.00212	-0.00479
-0.72898	0.0744	0.0898	0.0832	0.00245	-0.00189	-0.00463
-0.68834	0.0719	0.0906	0.0841	0.00242	-0.00192	-0.00428
-0.6477	0.0692	0.0946	0.0853	0.00212	-0.00167	-0.00438
-0.60452	0.0653	0.0981	0.087	0.00177	-0.00108	-0.00509
-0.56388	0.0636	0.101	0.0873	0.0015	-0.00125	-0.00403
-0.52324	0.0601	0.103	0.0895	0.00143	-0.00064	-0.00507
-0.4826	0.0595	0.105	0.0909	0.000744	-9.6E-05	-0.00538

Table F.10: Hot Data.

UW Component Reynolds Separated Shear Data
Hot Injection Case

Figures	(5.21a)	(5.21a)	(5.21a)	(5.21a)
y(cm)	RHO _b (UbV _b)	Ub(RHO _p V _p)	V _b (RHO _p U _p)	ReyShear
-2.15138	-0.0000974	-0.0000275	6.21E-06	-0.00012
-2.12344	-0.0000152	-0.0000586	6.04E-06	-6.8E-05
-2.08788	0.0000577	-0.0000757	6.98E-06	-1.1E-05
-2.05232	-0.0000175	-0.0000445	7.87E-06	-5.4E-05
-2.01168	-0.0000273	-0.0000503	7.63E-06	-7E-05
-1.97358	-0.0000409	-0.0000399	9.62E-06	-7.1E-05
-1.93294	-0.0000226	-0.000053	0.0000106	-6.5E-05
-1.8923	-0.0000708	-9.51E-06	0.0000109	-6.9E-05
-1.85166	-0.000028	0.0000042	0.0000122	-1.2E-05
-1.80848	0.0000274	-0.0000117	0.0000124	2.81E-05
-1.76784	0.000249	-0.0000807	0.0000108	0.00018
-1.72772	0.000412	-0.000132	0.0000101	0.000289
-1.68402	0.000373	-0.000145	6.27E-06	0.000234
-1.64338	0.000259	-0.000127	2.09E-06	0.000133
-1.5621	0.000364	-0.00024	-2.43E-06	0.000121
-1.4986	0.000699	-0.000384	-4.28E-06	0.000311
-1.44526	0.00114	-0.000507	-0.0000186	0.000611
-1.397	0.00102	-0.000369	-0.0000146	0.000632
-1.35382	0.00103	-0.000189	-2.39E-06	0.000843
-1.31064	0.00144	0.000247	0.000036	0.00172
-1.26746	0.000933	0.000767	0.0000462	0.00175
-1.22428	0.00075	0.0016	0.0000836	0.00243
-1.18364	0.00117	0.00228	0.000138	0.00358
-1.143	0.00144	0.00274	0.000161	0.00434
-1.09982	0.00246	0.00308	0.000213	0.00576
-1.05918	0.00361	0.00311	0.000266	0.00698
-1.016	0.00359	0.00306	0.000239	0.00689
-0.97536	0.00432	0.0027	0.000218	0.00723
-0.93472	0.00431	0.00273	0.000202	0.00724
-0.89408	0.00409	0.00272	0.000173	0.00698
-0.85344	0.00497	0.00234	0.000179	0.00748
-0.8128	0.00488	0.00222	0.000159	0.00726
-0.76962	0.00479	0.00212	0.000132	0.00704
-0.72898	0.00463	0.00189	0.0001	0.00662
-0.68834	0.00428	0.00192	0.0000876	0.0063
-0.6477	0.00438	0.00167	0.0000686	0.00612
-0.60452	0.00509	0.00108	0.00005	0.00622
-0.56388	0.00403	0.00125	0.0000319	0.00531
-0.52324	0.00507	0.000635	0.0000233	0.00573
-0.4826	0.00538	0.0000957	5.43E-06	0.00548

Table F.11: Hot Data.

UW Component Compressible Shear Data
Hot Injection Case

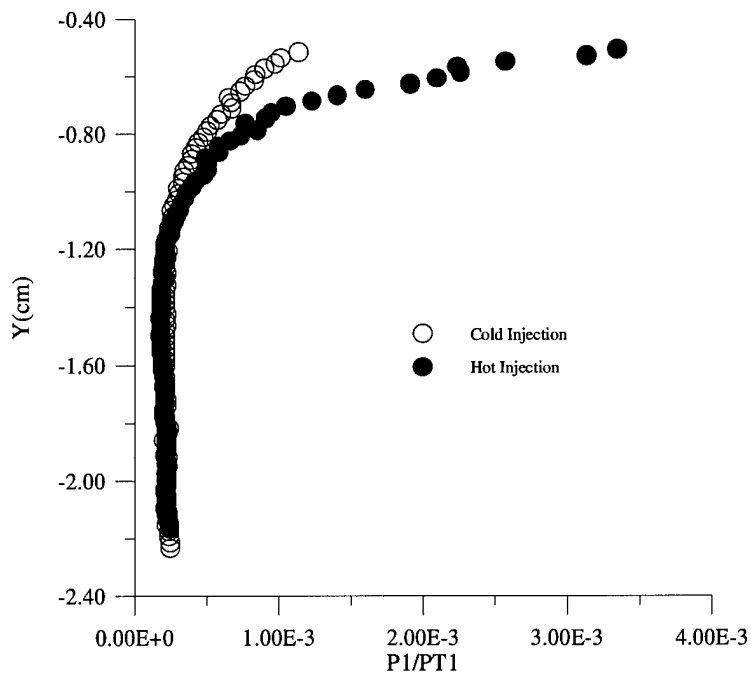
Figure	(5.14a)	(5.14a)	(5.14a)
y(cm)	term1	term2	shear
-2.15138	-9E-05	-1.8E-05	-0.00011
-2.12344	-4.6E-05	-1.9E-05	-6.6E-05
-2.08788	1.67E-05	-2.2E-05	-5.01E-06
-2.05232	-2E-05	-2.4E-05	-4.3E-05
-2.01168	-3.2E-05	-2.4E-05	-5.6E-05
-1.97358	-2E-05	-2.7E-05	-4.7E-05
-1.93294	-1.2E-05	-2.9E-05	-4.1E-05
-1.8923	-1.4E-05	-3.2E-05	-4.6E-05
-1.85166	3.66E-05	-3.4E-05	2.81E-06
-1.80848	9.33E-05	-3.3E-05	0.00006
-1.76784	0.000264	-3.4E-05	0.000231
-1.7272	0.0004	-3.2E-05	0.000368
-1.68402	0.000302	-3.3E-05	0.000269
-1.64338	0.000171	-3.6E-05	0.000135
-1.5621	0.000208	-6E-05	0.000148
-1.4986	0.000455	-8.4E-05	0.000371
-1.44526	0.000784	-0.00012	0.00066
-1.397	0.000829	-0.00018	0.000653
-1.35382	0.00114	-0.00023	0.000913
-1.31064	0.00215	-0.00031	0.00184
-1.26746	0.00217	-0.0004	0.00177
-1.22428	0.00291	-0.00051	0.0024
-1.18364	0.00419	-0.00062	0.00357
-1.143	0.005	-0.00065	0.00435
-1.09982	0.00652	-0.00067	0.00585
-1.05918	0.00795	-0.00063	0.00732
-1.016	0.00777	-0.00057	0.0072
-0.97536	0.00812	-0.00051	0.00761
-0.93472	0.00814	-0.00045	0.00769
-0.89408	0.00773	-0.00043	0.0073
-0.85344	0.00837	-0.00036	0.00801
-0.8128	0.00809	-0.00031	0.00778
-0.76962	0.00775	-0.00028	0.00747
-0.72898	0.00727	-0.00024	0.00703
-0.68834	0.00686	-0.00019	0.00667
-0.6477	0.00666	-0.00016	0.0065
-0.60452	0.00671	-0.00012	0.00659
-0.56388	0.0057	-9E-05	0.00561
-0.52324	0.00603	-6.1E-05	0.00597
-0.4826	0.00562	-2.7E-05	0.00559

UW Component Favre Data
Hot Injection Case

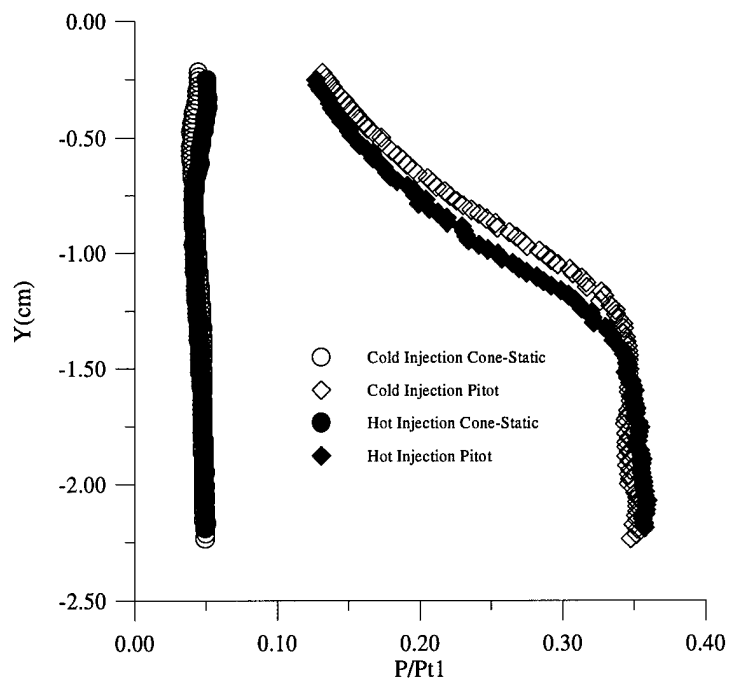
Figure	(5.22b)	(5.22b)	(5.21b)
y(cm)	ubar	wbar	FavShear
-2.15138	-0.00025	-2.8E-05	-9.7E-05
-2.12344	-0.00023	-5.9E-05	-1.5E-05
-2.08788	-0.00024	-7.6E-05	5.77E-05
-2.05232	-0.00025	-4.5E-05	-1.8E-05
-2.01168	-0.00024	-5E-05	-2.7E-05
-1.97358	-0.00027	-4E-05	-4.1E-05
-1.93294	-0.00028	-5.3E-05	-2.3E-05
-1.8923	-0.00027	-9.51E-06	-7.1E-05
-1.85166	-0.00028	4.2E-06	-2.8E-05
-1.80848	-0.00027	-1.2E-05	2.74E-05
-1.76784	-0.00023	-8.1E-05	0.000249
-1.7272	-0.00021	-0.00013	0.000412
-1.68402	-0.00013	-0.00015	0.000373
-1.64338	-4.6E-05	-0.00013	0.000259
-1.5621	5.09E-05	-0.00024	0.000364
-1.4986	8.56E-05	-0.00038	0.000699
-1.44526	0.000347	-0.00051	0.00114
-1.397	0.000254	-0.00037	0.00102
-1.35382	3.88E-05	-0.00019	0.00103
-1.31064	-0.00055	0.000247	0.00144
-1.26746	-0.00066	0.000767	0.000933
-1.22428	-0.00112	0.0016	0.00075
-1.18364	-0.00178	0.00228	0.00117
-1.143	-0.00205	0.00274	0.00144
-1.09982	-0.00276	0.00308	0.00246
-1.05918	-0.00354	0.00311	0.00361
-1.016	-0.00334	0.00306	0.00359
-0.97536	-0.00325	0.0027	0.00432
-0.93472	-0.00328	0.00273	0.00431
-0.89408	-0.00306	0.00272	0.00409
-0.85344	-0.0034	0.00234	0.00497
-0.8128	-0.00321	0.00222	0.00488
-0.76962	-0.00287	0.00212	0.00479
-0.72898	-0.00245	0.00189	0.00463
-0.68834	-0.00242	0.00192	0.00428
-0.6477	-0.00212	0.00167	0.00438
-0.60452	-0.00177	0.00108	0.00509
-0.56388	-0.0015	0.00125	0.00403
-0.52324	-0.00143	0.000635	0.00507
-0.4826	-0.00074	9.57E-05	0.00538

Appendix G

Pitot and Cone-Static Data



(a) Pressure distribution within the flowfield



(b) Pitot and cone-static measured pressure

Figure G.1: Pitot and Cone-Static Data.

Tabulated Pitot and Cone-Static Data

Cold Injection			Hot Injection		
Y(cm)	Pitot Ratio	Cone-Static Ratio	Y(cm)	Pitot Ratio	Cone-Static Ratio
-2.23551	0.3478263	4.98E-02	-2.18993	0.357425	4.96E-02
-2.21633	0.3516642	0.0500844	-2.17018	0.356963	5.05E-02
-2.19568	0.3520321	4.98E-02	-2.15018	0.3559806	5.02E-02
-2.17634	0.3495611	4.96E-02	-2.13051	0.3577821	5.01E-02
-2.15724	0.352042	4.90E-02	-2.11182	0.358539	5.03E-02
-2.13749	0.3511918	4.93E-02	-2.09109	0.3585073	4.96E-02
-2.11765	0.3519499	4.90E-02	-2.07158	0.3591069	4.97E-02
-2.09774	0.352008	4.85E-02	-2.05183	0.3575317	0.0496728
-2.07848	0.352026	0.049099	-2.03249	0.3577063	4.92E-02
-2.05848	0.352328	4.89E-02	-2.01201	0.3566374	4.97E-02
-2.0393	0.3510042	4.87E-02	-1.99258	0.3564275	0.0493919
-2.01939	0.3493195	4.90E-02	-1.97332	0.3555905	4.95E-02
-1.99939	0.3463465	0.0484647	-1.95259	0.3553488	4.97E-02
-1.97964	0.3471932	4.85E-02	-1.93365	0.3548493	4.94E-02
-1.96021	0.3465945	4.86E-02	-1.91406	0.3554575	4.90E-02
-1.94038	0.3474798	4.84E-02	-1.89447	0.3558004	4.95E-02
-1.92031	0.3450581	4.86E-02	-1.87432	0.3546633	4.94E-02
-1.9008	0.3469857	0.0484203	-1.85505	0.3537763	4.92E-02
-1.88105	0.3448408	4.85E-02	-1.83514	0.3517442	4.94E-02
-1.86162	0.3462211	4.75E-02	-1.81506	0.352686	4.92E-02
-1.8413	0.3447314	4.80E-02	-1.79564	0.3531366	4.87E-02
-1.82171	0.3444602	4.91E-02	-1.77572	0.3536621	4.82E-02
-1.80188	0.3464295	4.83E-02	-1.75614	0.3542758	4.85E-02
-1.78229	0.3447194	4.79E-02	-1.7363	0.3529591	4.86E-02
-1.7627	0.346655	4.78E-02	-1.71737	0.3502391	4.83E-02
-1.74295	0.3438883	4.82E-02	-1.69696	0.3511074	4.83E-02
-1.72288	0.3441811	4.83E-02	-1.67729	0.3516459	4.82E-02
-1.70313	0.3458062	4.80E-02	-1.65779	0.3503342	4.82E-02
-1.6837	0.3458406	4.79E-02	-1.63755	0.3499325	4.78E-02
-1.6633	0.3482007	0.0482728	-1.61812	0.349222	4.76E-02
-1.64404	0.3479317	4.83E-02	-1.59837	0.350251	4.77E-02
-1.62437	0.3477184	4.78E-02	-1.57911	0.3491977	4.73E-02
-1.6047	0.3463547	4.80E-02	-1.55822	0.3479581	4.67E-02
-1.58462	0.3463174	4.79E-02	-1.53961	0.3459763	4.67E-02
-1.56503	0.3473381	0.0481116	-1.51977	0.3441626	4.63E-02
-1.54512	0.345954	4.83E-02	-1.49986	0.3458447	4.61E-02
-1.52529	0.3463279	4.80E-02	-1.47987	0.3450986	4.64E-02
-1.5057	0.3468777	4.83E-02	-1.46101	0.3449344	4.63E-02
-1.48586	0.3458059	0.0478623	-1.44085	0.3426057	4.59E-02
-1.46571	0.3465538	4.84E-02	-1.42069	0.3413131	4.63E-02
-1.44596	0.3465686	4.82E-02	-1.40159	0.3393089	4.59E-02
-1.42661	0.3460034	4.86E-02	-1.38144	0.3357554	4.56E-02
-1.40621	0.3453035	4.80E-02	-1.36128	0.3354461	4.54E-02
-1.38695	0.3448515	4.81E-02	-1.3421	0.3323271	4.51E-02
-1.36687	0.3439976	0.047895	-1.32243	0.3299949	4.52E-02
-1.34728	0.3420115	4.75E-02	-1.30251	0.3220475	4.53E-02
-1.32745	0.3426073	4.79E-02	-1.28244	0.3210061	4.43E-02

Table G.1: Pitot and Cone Static Data.

Pitot and Cone-Static Data

Cold Injection			Hot Injection		
Y(cm)	Pitot Ratio	Cone-Static Ratio	Y(cm)	Pitot Ratio	Cone-Static Ratio
-1.30754	0.342431	4.75E-02	-1.26334	0.319679	4.46E-02
-1.28795	0.339499	4.78E-02	-1.24293	0.31355	4.41E-02
-1.26755	0.337611	0.047099	-1.22326	0.311172	0.044071
-1.24828	0.336989	4.72E-02	-1.204	0.308547	4.39E-02
-1.22878	0.333402	4.71E-02	-1.18417	0.304137	4.35E-02
-1.20886	0.326566	0.046532	-1.1636	0.298971	4.33E-02
-1.18871	0.32901	4.64E-02	-1.14434	0.292263	0.043175
-1.1692	0.327325	4.63E-02	-1.12451	0.286909	4.30E-02
-1.14904	0.31687	4.62E-02	-1.10427	0.281958	4.31E-02
-1.12945	0.316684	4.60E-02	-1.08533	0.275019	4.29E-02
-1.10962	0.313276	4.60E-02	-1.0655	0.2697	4.28E-02
-1.08987	0.307272	4.58E-02	-1.0451	0.265042	4.26E-02
-1.07012	0.305102	4.52E-02	-1.02551	0.257422	4.23E-02
-1.04996	0.296661	4.50E-02	-1.00608	0.254822	4.24E-02
-1.0307	0.292291	4.49E-02	-0.98633	0.247881	4.23E-02
-1.01046	0.288097	4.48E-02	-0.96609	0.241293	4.20E-02
-0.99079	0.283579	4.43E-02	-0.94699	0.234294	4.21E-02
-0.97128	0.275447	4.42E-02	-0.92684	0.232715	4.25E-02
-0.95137	0.272144	4.38E-02	-0.90652	0.230975	4.22E-02
-0.93113	0.267649	4.35E-02	-0.88701	0.229515	4.17E-02
-0.91113	0.262965	4.36E-02	-0.86799	0.219155	4.18E-02
-0.89203	0.254442	4.31E-02	-0.84743	0.219045	4.18E-02
-0.87163	0.25313	4.29E-02	-0.82735	0.212636	0.042053
-0.85237	0.24676	4.27E-02	-0.80857	0.207057	4.22E-02
-0.83213	0.241674	4.24E-02	-0.78801	0.199466	4.23E-02
-0.8136	0.236287	4.24E-02	-0.76777	0.203946	4.21E-02
-0.79303	0.23025	4.20E-02	-0.74834	0.19681	4.25E-02
-0.77401	0.226009	4.18E-02	-0.72892	0.195559	4.27E-02
-0.75386	0.221638	4.20E-02	-0.70779	0.191354	4.29E-02
-0.7337	0.217639	4.19E-02	-0.68917	0.183958	4.31E-02
-0.71452	0.211829	4.21E-02	-0.66967	0.179619	4.36E-02
-0.69452	0.208948	4.16E-02	-0.64918	0.177056	4.44E-02
-0.67558	0.205477	4.08E-02	-0.62984	0.174645	4.58E-02
-0.65543	0.198432	4.07E-02	-0.60984	0.171726	4.61E-02
-0.636	0.195299	4.07E-02	-0.59001	0.167195	4.59E-02
-0.61601	0.190828	4.07E-02	-0.56953	0.166666	4.57E-02
-0.5965	0.188126	4.03E-02	-0.55067	0.162757	4.63E-02
-0.57691	0.184507	4.03E-02	-0.5306	0.157907	4.74E-02
-0.55748	0.17998	4.03E-02	-0.51028	0.155091	4.75E-02
-0.53725	0.176977	4.01E-02	-0.49085	0.152198	0.047548
-0.51749	0.173624	4.05E-02	-0.47126	0.150256	4.89E-02
-0.49848	0.173039	4.06E-02	-0.4511	0.14822	4.96E-02
-0.47791	0.167128	4.03E-02	-0.43095	0.144791	4.99E-02
-0.45881	0.163324	4.09E-02	-0.41201	0.1433	4.98E-02
-0.43898	0.161643	0.041177	-0.39136	0.140604	5.11E-02
-0.41939	0.156943	4.16E-02	-0.37177	0.138419	5.14E-02
-0.39939	0.15579	4.20E-02	-0.35227	0.136887	5.11E-02

Pitot and Cone-Static Data

Cold Injection			Hot Injection		
Y(cm)	Pitot Ratio	Cone-Static Ratio	Y(cm)	Pitot Ratio	Cone-Static Ratio
-0.38021	0.152187	4.27E-02	-0.33244	0.135613	5.17E-02
-0.36046	0.149751	0.043279	-0.31195	0.13297	5.11E-02
-0.34039	0.147287	4.40E-02	-0.29228	0.130423	5.14E-02
-0.32137	0.144211	4.43E-02	-0.27351	0.128142	5.11E-02
-0.30088	0.140864	4.46E-02	-0.25278	0.127147	5.06E-02
-0.28195	0.138991	4.51E-02			
-0.26138	0.136639	4.49E-02			
-0.24293	0.134364	4.56E-02			
-0.22164	0.131845	4.50E-02			

Bibliography

1. Fuller, E., Mays, R., Thomas, R., and Schetz, J., "Mixing Studies of Helium in Air at High Supersonic Speeds," *AIAA Journal*, Vol. 30, No. 9, 1992, pp. 2234-2243.
2. Mays, R., Thomas, R., and Schetz, J., "Low Angle Injection into a Supersonic Flow," AIAA-89-2461, AIAA, Washington D.C., 1989.
3. Heiser, William H., Pratt, David T., *Hypersonic Airbreathing Propulsion*, AIAA Washington, DC 1994.
4. Rizzetta, Donald P. "Numerical Simulation of Slot Injection into a Turbulent Supersonic Stream", *AIAA Journal*, Vol. 30, No. 10, 1992, pp. 2434-2439.
5. Speziale, C.G. (1985) "Modeling the Pressure-Gradient-Velocity Correlation of Turbulence," *Physics of Fluids*, Vol. 28,pp. 69-71.
6. Wilcox, David C., *Turbulence Modeling for CFD*, DCW Industries, Inc., La Canada, California 1993
7. Cebeci, T., and Smith, A.M.O., *Analysis of Turbulent Boundary Layers*, Academic Press, 1974.
8. Gilreath, H.E. and Schetz, J.A., "Transition and Mixing in the Shear Layer Produced by Tangential Injection in Supersonic flow," *Journal of Basic Engineering*, December 1971, pp. 610-618.
9. Bowersox, R.D.W., "Compressible Turbulence in a High-Speed High-Reynolds Number Mixing Layer," Ph.D. Dissertation, Virginia Polytechnic Institute and State University, VA, Department of Aerospace Engineering, September 1992.
10. Schetz, J.A., *Foundations of Boundary Layer Theory for Momentum, Heat Transfer, and Mass Transfer*, Englewood Cliffs, NJ 1984.
11. Marks, L.S. and Baumeister, T. *Standard Handbook for Mechanical Engineers, 7th Edition*, McGraw-Hill Book Company, New York, NY
12. Incropera, F.P. and DeWitt, D.P. *Introduction to Heat Transfer, 2nd Edition*, John Wiley & Sons, New York, NY 1990
13. Nicolet, *Nicolet Systems Operation*, Madison, WI, 1991

14. Volluz, R., *Handbook of Supersonic Aerodynamics*, Section 20, Wind Tunnel Instrumentation and Operation, NAVORD Report 1488, Vol. 6. Ordnance Aerophysics Laboratory, Daingerfield, TX, 1961.
15. TSI Incorporated , *Hot-Wire / Hot-Film Anemometry*, St. Paul, MN 1988
16. Bowersox, R., "Thermal Anemometry," *Handbook of Fluid Mechanics and Fluid Machinery*, John Wiley and Sons, Sect. 15.4.2, Dec. 1995, pp. 15.29 - 15.40.
17. Huffman, Richard E. "Investigation into the Flow Structure in the Vicinity of a Wrap-Around Fin," Masters Thesis, December 1995, Air Force Institute of Technology, Wright-Patterson AFB, OH.
18. Bowersox, R., and Hokenson, A., "Refractive Optical Flow Visualization Techniques," *Handbook of Fluid Mechanics and Fluid Machinery*, John Wiley and Sons, Sect. 15.6.2, Dec. 1995, pp. 15.40 - 15.69.
19. Bowersox, R.D.W., "MSHeAR User's Manual," Department of Aeronautics, Air Force Institute of Technology, Wright-Patterson AFB, Ohio, 1994.
20. Holman, J.P. *Heat Transfer*, 6th Ed., McGraw-Hill Book Co., 1986
21. Berkey, Dennis D., *Calculus*, 2nd Ed., Saunders College Publishing, New York, NY 1988.
22. Burden, R.L., and Faires, D.J. *Numerical Analysis*, 5th ed., PWS Publishing Company, Boston, MA 1993
23. Powrie, H., Ball, G., and East, R. "Comparison of the Interactions of Two and Three Dimensional Traverse Jets with a Hypersonic Free Stream", AGARD-CP-534, NATO, April 1993
24. Settles, G. and Dodson, L. "Supersonic and Hypersonic Shock / Boundary - Layer Interaction Database." *AIAA Journal*, Vol 32, No. 7, July 1994.
25. Miller, R. "Compressible Turbulence measurements in a Supersonic Boundary Layer Including Favorable Pressure Gradient Effects." Master's Thesis, December 1994, Air Force Institute of Technology, Wright-Patterson AFB, OH.
26. Dotter, J. "Compressible Turbulence Measurements in a Supersonic Flow with Adverse Pressure Gradient." Master's Thesis, December 1994, Air Force Institute of Technology, Wright-Patterson AFB, OH.

27. McCann, G.J. and Bowersox, R.D.W. "Experimental Investigation of Supersonic Gaseous injection into a Supersonic Free Stream" AIAA 96-0197, 1996 Also accepted AIAA Journal.
28. Gnielinski, V. *Int. Chem. Eng.* **16**, 359, 1976.
29. Petukhov, P.S. in T.F. Irvine and J.P. Hartnett, Ed., *Advances in Heat Transfer*, Volume 6, Academic Press, New York, 1970.

Vita

Kelly Colin Tucker was born on January 29, 1971, in Tuscaloosa, Alabama. He graduated Valedictorian from Porters Chapel Academy in 1989, and accepted a scholarship to attend Mississippi State University. After graduating in 1994, he was commissioned a Second Lieutenant in the United States Air Force, and became the fourth generation of military officers in his family. He married the former Ms. Allison Wallace of Tupelo, MS, and reported to his first assignment to complete the Masters program at the Air Force Institute of Technology. After graduation in December of 1995, his next assignment is with the Aeronautical Systems Center at Wright-Patterson AFB, Ohio.